



UNIVERSIDADE FEDERAL DE SANTA CATARINA  
CAMPUS JOINVILLE  
PROGRAMA DE PÓS-GRADUAÇÃO EM ENGENHARIA E CIÊNCIAS  
MECÂNICAS

BRUNA LARISSA TASCHECK

**NUMERICAL ANALYSIS OF HYDRODYNAMIC CHARACTERISTICS  
OF A PLATE AND SHELL HEAT EXCHANGER (PSHE)**

JOINVILLE

2019

Bruna Larissa Tascheck

**NUMERICAL ANALYSIS OF HYDRODYNAMIC CHARACTERISTICS  
OF A PLATE AND SHELL HEAT EXCHANGER (PSHE)**

Dissertação submetida ao Programa de Pós  
Graduação em Engenharia e Ciências Mecânicas  
da Universidade Federal de Santa Catarina para a  
obtenção do título de Mestre em  
Engenharia e Ciências Mecânicas.

Orientador: Prof. Dr<sup>a</sup>. Talita Sauter Possamai

Coorientador: Prof. Dr. Jorge Goes Oliveira

Joinville

2019

Ficha de identificação da obra elaborada pelo autor,  
através do Programa de Geração Automática da Biblioteca Universitária da UFSC.

Tascheck, Bruna Larissa

Numerical analysis of hydrodynamic characteristics of a  
plate and shell heat exchanger (PSHE) / Bruna Larissa  
Tascheck ; orientador, Talita Sauter Possamai,  
coorientador, Jorge Goes Oliveira, 2019.  
102 p.

Dissertação (mestrado) - Universidade Federal de Santa  
Catarina, Campus Joinville, Programa de Pós-Graduação em  
Engenharia e Ciências Mecânicas, Joinville, 2019.

Inclui referências.

1. Engenharia e Ciências Mecânicas. 2. Permutador de  
calor. 3. PSHE. 4. CFD. I. Sauter Possamai, Talita . II.  
Goes Oliveira, Jorge . III. Universidade Federal de Santa  
Catarina. Programa de Pós-Graduação em Engenharia e Ciências  
Mecânicas. IV. Título.

Bruna Larissa Tascheck

**Numerical Analysis of Hydrodynamic Characteristics of a Plate and Shell Heat Exchanger (PSHE)**

O presente trabalho em nível de mestrado foi avaliado e aprovado por banca examinadora composta pelos seguintes membros:

Prof. Fabiano Gilberto Wolf, Dr.  
Universidade Federal de Santa Catarina

Prof. Kleber Vieira de Paiva, Dr.  
Universidade Federal de Santa Catarina

Prof. Roberto Wolf Francisco Junior, Dr.  
Universidade do Estado de Santa Catarina

Certificamos que esta é a **versão original e final** do trabalho de conclusão que foi julgado adequado para obtenção do título de mestre em Engenharia e Ciências Mecânicas.

---

Prof. Dr. Régis Kovacs Scalice  
Coordenador do Programa

---

Prof. Dr<sup>a</sup>. Talita Sauter Possamai  
Orientadora

Joinville, 27 de setembro de 2019.



## **AGRADECIMENTOS**

Agradeço a minha família pelo apoio e incentivo.

Agradeço a minha professora orientadora Dr<sup>a</sup>. Talita Sauter Possamai e ao meu professor coorientador Dr. Jorge Goes Oliveira, pelo conhecimento transmitido e pela confiança depositada. A Renato Oba pelas contribuições ao desenvolvimento desse trabalho.

Agradeço à FEESC, à PETROBRAS e à ANP pelos recursos oferecidos durante o período do presente trabalho.

Agradeço em especial aos meus amigos de laboratório pelos momentos de amizade e contribuição de trabalho: Damylle Cristina Xavier Donati e Rodrigo Santiago.



## RESUMO

O permutador de calor de placas soldadas (PSHE) é um trocador de calor que apresenta um formato compacto e robusto, sendo uma variação do trocador de calor de placas (PHE). O presente trabalho apresenta uma análise de um par de placas de um PSHE empregando dinâmica computacional dos fluidos (CFD) para determinar as suas características hidrodinâmicas para três configurações de ângulo de Chevron,  $15^\circ \times 15^\circ$ ,  $45^\circ \times 45^\circ$  e  $15^\circ \times 45^\circ$ . Para tanto o programa comercial ANSYS CFX é empregado. Dois modelos de turbulência, Standard  $k - \epsilon$  e SST (Shear-Stress-Transport), foram empregados na análise e seus resultados analisados para comparação. Dados experimentais de perda de carga e linhas de corrente do escoamento foram empregados na validação dos modelos numéricos e na análise das simplificações nos modelos geométricos. Resultados de perda de carga no par de placas obtidos pelo modelo numérico apontam um desvio com relação aos dados experimentais máximo de 11,40% para a configuração  $45^\circ \times 45^\circ$  ( $1993 < Re < 7529$ ), 13,20% para a configuração de  $45^\circ \times 15^\circ$  ( $1305 < Re < 6153$ ) e acima de 60% para a configuração de  $15^\circ \times 15^\circ$  ( $1332 < Re < 4034$ ). Apesar do elevado erro na configuração  $15^\circ \times 15^\circ$  para perda de carga, o formato das linhas de corrente encontradas no modelo numérico concordam com o encontrado experimentalmente e também descrito na literatura para baixos ângulos de Chevron, em zig-zag. Para a configuração  $45^\circ \times 45^\circ$  o formato com reflexão do escoamento pelas bordas da placa, também descrito na literatura, foi visualizado, enquanto que para a configuração  $45^\circ \times 15^\circ$  uma mistura do comportamento dos dois ângulos foi encontrado. A comparação com as correlações experimentais empregadas para os PHEs indicou que as correlações de Kumar (1984) para  $\beta \leq 65^\circ$  e  $\beta = 45^\circ$  apresentam valores de perda de carga equivalentes aos encontrados pelo modelo numérico, apesar de não haver concordância com a definição do ângulo de Chevron indicado nas correlações, o que sugere que possivelmente os resultados de Nu e força de atrito, derivados destas correções, também possam ser aplicados as placas do PSHE em conjunto com os dados obtidos por meio do modelo numérico proposto.

**Palavras-chave:** Permutador de calor. PSHE. CFD.

## RESUMO EXPANDIDO

### Introdução

O permutador de calor de placas soldadas (PSHE) é um trocador de calor que apresenta uma ampla faixa de aplicação devido a sua robustez e formato compacto. O PSHE é composto por placas corrugadas circulares, sendo uma variação dos trocadores de calor de placas (PHEs), formados por placas retangulares e conectados através de gaxetas ao invés de solda.

A geometria dos canais formados por placas corrugadas é provavelmente a mais complexa de todos os dutos de fluxo. O ângulo de Chevron, a amplitude e o comprimento da onda, a forma da ondulação, espessura da chapa, etc., são parâmetros de projetos que definem o desempenho do permutador de calor. Como na literatura é escasso o número de trabalhos focados em PSHEs, o presente trabalho estuda os canais do PSHE empregando a dinâmica computacional dos fluidos (CFD) para determinar as características hidrodinâmicas das placas deste tipo de permutador de calor.

### Objetivos

O objetivo principal deste estudo é analisar o comportamento hidrodinâmico do fluxo em canais com diferentes configurações de um PSHE, utilizando um modelo numérico turbulento tridimensional. Os objetivos específicos são os seguintes: apresentar uma revisão do estado da arte atual de trocadores de calor PHE e PSHE com relação a informações do comportamento do escoamento e modelagem numérica; simular o escoamento frio de água no canal interno de um par de placas de um PSHE com ângulo de Chevron de  $15^\circ \times 15^\circ$ ,  $45^\circ \times 45^\circ$  e  $15^\circ \times 45^\circ$  para os números de Reynolds  $1332 \leq Re \leq 10819$ ,  $1993 \leq Re \leq 7529$  e  $1305 \leq Re \leq 6153$ , respectivamente; validar o modelo numérico do escoamento interno para a queda de pressão total, identificando qual modelagem da turbulência e simplificação de geometria é a mais indicada, através de dados experimentais; analisar o perfil de velocidade média para o escoamento entre um par de placas com ângulo de Chevron de  $15^\circ \times 15^\circ$ ,  $45^\circ \times 45^\circ$  e  $15^\circ \times 45^\circ$  para três faixas de números de Reynolds (baixa, média e alta); identificar a limitação dos modelos; identificar as correlações para queda de pressão desenvolvidas para os PHEs que melhor descrevem o comportamento do escoamento interno de um par de placas de um PSHE.

### Metodologia

Quatro domínios computacionais foram analisados: Caso 1: consiste em duas placas corrugadas que formam um canal com  $\beta = 15^\circ$  e com tubos de 0,168 m de comprimento conectados às portas de entrada e saída da placa. Os tubos tornam a geometria similar a utilizada na bancada experimental, onde a pressão é aferida na posição de 0,168 m.; Caso 2: o domínio computacional apresentado no Caso 1 foi segmentado ao longo do eixo vertical e os tubos foram excluídos, dando origem a placa corrugada simétrica, onde a condição de simetria foi adotada na interface seccionada. Representando a metade da placa corrugada, a placa simétrica possui a metade da área da seção das portas de admissão e descarga; Caso 3: consiste em duas placas corrugadas segmentadas ao longo do eixo vertical formando um canal simétrico com  $\beta = 45^\circ$ . A condição de simetria aplicada e a área da seção das portas de entrada e saída são equivalentes às do Caso 2; Caso 4: consiste em duas placas corrugadas segmentadas ao longo do eixo vertical formando um canal simétrico com  $\beta = 45^\circ \times 15^\circ$ . A condição de simetria aplicada e a área da seção das portas de entrada e saída são equivalentes às do Caso 2.

A faixa de número de Reynolds avaliada é  $1332 \leq Re \leq 4034$  para os Casos 1 e 2;  $1993 \leq Re \leq 7529$  para o Caso 3 e  $1305 \leq Re \leq 6153$  para o Caso 4.

As condições de contorno aplicadas para os quatro casos estudados foram as mesmas. Para a entrada foi especificada a vazão mássica na seção da porta de entrada do canal, a direção da vazão mássica foi considerada normal à superfície de entrada, assumindo que o fluxo é uniformemente distribuído na região de admissão. A intensidade percentual da turbulência admitida foi de 5%. Na saída, a pressão manométrica foi descrita como um valor constante igual a zero para 0,05 como mistura de perfil de pressão. As paredes da placa foram consideradas fixas e com rugosidade igual a zero. O critério de convergência adotado é de  $1 \times 10^{-5}$  (RMS). Água foi utilizada como fluido de trabalho com temperatura constante igual a 25°C com densidade de  $997 \text{ kg/m}^3$  e viscosidade dinâmica de  $8,9 \times 10^{-4} \text{ Pa.s}$ .

O programa utilizado para realizar as simulações foi o ANSYS CFX. Devido à complexidade da geometria dos canais estudados as malhas foram concebidas com morfologia tetraédrica. Uma malha constituída de aproximadamente 22 milhões de volumes (M22) e 60 milhões (M60) foi gerada para o Caso 1. Para os Casos simétricos 2, 3 e 4, malhas constituídas de 4 (M4), 11 (M11) 21 (M21) e 52 (M52) milhões de volumes foi aplicada, com o objetivo de estudar a influência da densidade da malha juntamente com os modelos de turbulência. Os modelos de turbulência SST e Standard  $k - \epsilon$  com tratamento de parede Scalable foram aplicados para cada caso estudado para a obtenção dos resultados numéricos. A validação dos dados foi realizada comparando os resultados numéricos com os obtidos experimentalmente através de uma bancada apresentada por Beckdorff et al., 2019.

## Resultados e Discussão

A análise numérica da queda de pressão apresentou resultados satisfatórios para os Casos 3 ( $45^\circ \times 45^\circ$ ) e 4 ( $45^\circ \times 15^\circ$ ), concordando com os resultados experimentais, indicando desvios menores que 13,20% para toda a faixa de Re analisada. Desvios abaixo de 5% foram obtidos para Re abaixo de 4644 para o Caso 3 enquanto um desvio de 10% foi encontrado para Re abaixo de 4005 para o Caso 4. O modelo de turbulência SST obteve maior desempenho quando aplicado com malhas mais densas (21 to 52 million volumes), enquanto que o modelo  $k - \epsilon$  tem melhor desempenho com as malhas mais grossas (4 to 11 million volumes). Isso era esperado, já que para densidades de malha mais baixas, a distância da parede adimensional,  $y^+$ , para ambos os modelos é prevista com valores superiores a 1, o valor recomendado para o modelo SST para estimar corretamente a camada limite. Entretanto, desvios acima de 80% e 60% foram observados para os Casos 1 e 2 ( $15^\circ \times 15^\circ$ ), nesta ordem. A presença dos tubos justifica a menor concentração de malha no Caso 1, fator que contribui para erro.

De modelo geral, os campos de pressão mostram a perda gradual da pressão ao longo do canal. A queda de pressão ocorre devido à redução abrupta da seção transversal do canal, e a interação do fluxo com os pontos de contato que acabam reduzindo a velocidade do escoamento.

Com relação aos campos de velocidade, os vetores indicam que o fluxo segue predominantemente na direção vertical, com velocidades expressivas no centro do canal, fluindo da porta de entrada para a porta de saída do canal. O comportamento do campo de velocidade é uniforme na porta de entrada (Caso 1), a baixa pressão local e a aceleração do escoamento facilitam a admissão do fluido, comportamento contrário do observado na porta de saída, onde ocorre a formação de vórtices.

Os padrões de fluxo foram identificados para os canais, com formato zig-zag para o canal  $15^\circ \times 15^\circ$ , com caminho preferencial entre os sulcos para a configuração  $45^\circ \times 45^\circ$ , e uma combinação dos padrões é exibida para o arranjo  $15^\circ \times 45^\circ$ .

Os perfis de velocidade média obtidos na seção transversal dos canais 2, 3 e 4, foram estudados. Apresentando perfis com pequenas variações ao longo da seção, os Casos 2 e 4 são semelhantes, enquanto que o Caso 3 apresenta perfis parabólicos com picos de velocidade no

centro do canal. Este comportamento aponta para uma grande diferença entre as áreas efetivas de transferência de calor, onde os Casos 2 e 4 contemplam uma área maior.

Os resultados da queda de pressão obtidos por meio das correlações desenvolvidas para os PHEs, foram comparados com os dados numéricos para os canais do PSHE. Desta comparação foi possível concluir que a correlação de Kumar para  $\beta \leq 65^\circ$  é a mais adequada para representar os Casos 2 e 4, enquanto que a correlação de Kumar para  $\beta = 45^\circ$  descreve com maior precisão o Caso 3. A conformidade dos resultados apresentados na seção 4.2.3 é associada ao conjunto das características geométricas dos canais e não exclusivamente ao ângulo de Chevron.

O número de Reynolds,  $Re(x,y)$ , fator de atrito,  $f(x,y)$ , e Nusselt,  $Nu(x,y)$ , foram calculados localmente para os Casos 2, 3 e 4. Os resultados concordam qualitativamente, valores elevados de  $Re(x,y)$  e  $Nu(x,y)$  concentram-se no centro dos canais, inversamente proporcional, o fator de atrito local é menor na mesma região. Quantitativamente os resultados para os Casos 2 e 4 são similares, visto que foram obtidos para as mesmas correlações de Kumar para  $\beta \leq 65^\circ$ , diferente do Caso 3 que utiliza as correlações de Kumar para  $\beta = 45^\circ$ . Derivado das correlações o número de Nusselt local pode ser impreciso, uma vez que o estudo das correlações levou em consideração apenas o fator de atrito. Isto posto, consideramos a média local de  $Re(x,y)$  para identificar o canal com maior eficiência térmica. A configuração  $15^\circ \times 15^\circ$  foi então apontada como a configuração geométrica mais eficaz. Ainda, um baixo desvio foi verificado para as médias locais de  $Re(x,y)$ ,  $f(x,y)$  e  $Nu(x,y)$ , com relação as médias obtidas no plano médio dos canais, indicando que os valores médios locais são representativos do canal do PSHE.

Com relação às forças de cisalhamento, as componentes horizontais são expressivas nas áreas adjacentes as portas de entrada e saída, enquanto que as componentes verticais são significantes no centro dos canais. A região de saída do canal concentra as maiores forças, devido a recirculação do fluxo, tornando a área susceptível a fadiga. A integral da força de cisalhamento resulta em um valor próximo de zero para as componentes horizontais, para a componente vertical -1.49 N, -1.55 N e -1.60 N para os Casos 2, 3 e 4, respectivamente. Este resultado propõe que a configuração  $45^\circ \times 15^\circ$  (Caso 4) possui maiores gradientes de velocidade.

## Conclusões

A modelagem numérica dos canais de um PSHE, apresentada neste estudo, revela o comportamento hidrodinâmico de quatro domínios computacionais distintos, analisando três diferentes ângulos de Chevron ( $\beta = 15^\circ \times 15^\circ$ ,  $45^\circ \times 45^\circ$  e  $15^\circ \times 45^\circ$ ). A verificação dos modelos numéricos foi realizada comparando os resultados com os dados experimentais para perda de carga total em um par de placas para três configurações de ângulo de Chevron e formato das linhas de corrente para uma configuração. As maiores contribuições do trabalho estão listadas na sequência:

- a) Os resultados para a queda de pressão revelaram que o modelo SST apresenta erro máximo menor de 15% para as configurações de  $45^\circ \times 45^\circ$  e  $45^\circ \times 15^\circ$  para toda a faixa de  $Re$  analisada e que o modelo para a configuração de  $15^\circ \times 15^\circ$  apresenta erro elevado e deve ser melhor analisado;
- b) A identificação do padrão de escoamento da configuração  $45^\circ \times 15^\circ$ , não identificada na literatura, onde o comportamento ocorre de forma misturada entre o comportamento esperado para a configuração  $15^\circ \times 15^\circ$  e  $45^\circ \times 15^\circ$ . O padrão de escoamento aqui foi apresentado apenas para um número de  $Re$  e a influência deste último no padrão não foi analisada, sendo este um ponto interessante a ser abordado em um estudo mais avançado;

A comparação de correlações experimentais já existentes para PHEs para uso em PSHEs se mostrou possível com relação à perda de carga total no par de placas e à força de cisalhamento exercida nas placas. Apesar da aplicação neste trabalho das correlações também para o cálculo de  $Nu$ , o mesmo não foi comparado com valores próprios do modelo numérico, como no caso da perda de carga total nas placas e da força de cisalhamento. Para isso, um estudo incluindo a troca de calor nas placas é necessário, sugerido aqui como um trabalho futuro.

**Palavras-chave:** Permutador de calor. PSHE. CFD.

## ABSTRACT

The Plate-Shell Heat Exchanger (PSHE) is a heat exchanger that has a compact and robust shape, which is a variation of the plate heat exchanger (PHE). This paper presents a plate pair analysis of a PSHE employing the computational fluid dynamics (CFD) to determine the hydrodynamic characteristics for three Chevron angle configurations,  $15^\circ \times 15^\circ$ ,  $45^\circ \times 45^\circ$  and  $45^\circ \times 15^\circ$ . Therefore, the ANSYS CFX trading program is employed. Two turbulence models, Standard k- $\epsilon$  and SST (Shear-Stress-Transport), were employed in the analysis and their results analyzed for comparison. Experimental pressure drop data and flow current lines were used to validate numerical models and to analyze simplifications in geometric models. Plate pair pressure drop results obtained by the numerical model indicate a deviation from the maximum experimental data of 11.40% for the  $45^\circ \times 45^\circ$  configuration ( $1993 \leq Re \leq 7529$ ), 13.20% for the  $45^\circ \times 15^\circ$  configuration ( $1305 \leq Re \leq 6153$ ) and above 60% for the  $15^\circ \times 15^\circ$  configuration ( $1332 \leq Re \leq 4034$ ). Despite the high error in the  $15^\circ \times 15^\circ$  configuration for pressure drop, the shape of the current lines found in the numerical model agree with that found experimentally and also described in the low angle Chevron zig-zag literature. The  $45^\circ \times 45^\circ$  configuration the shape with reflection of the plate edge flow, also described in the literature, was visualized, while for the  $45^\circ \times 15^\circ$  configuration a mixture of the behavior of the two angles was found. Comparison with the experimental correlations employed for the PHEs indicated that the correlations of Kumar (1984) for  $\beta \leq 65^\circ$  and  $\beta = 45^\circ$  present pressure drop values equivalent to those found by the numerical model, although there is no agreement with the definition of the Chevron angle indicated in this correlations, which suggests that possibly the results of Nu and frictional strength derived from these corrections may also be applied to the PSHE plates together with the data obtained through the proposed numerical model.

**Keywords:** Heat exchanger. PSHE. CFD.

## LIST OF FIGURES

Figure 1.1 – Types of heat exchangers: (a) direct transfer; (b) spiral plate; (c) shell-and-tube; (d) plate and shell; (e) gasketed plate; (f) brazed plate. ....	15
Figure 2.1 – Gasket plate heat exchanger.....	20
Figure 2.2 – Brazed Plate Heat Exchangers. ....	21
Figure 2.3 – Schematic of a PSHE. ....	22
Figure 2.4 – Plate geometry: Plate design of PSHE (a); Characteristics of the plate wave (b).....	23
Figure 2.5 – Influence of the Chevron angle on the flow pattern for a GPHE.....	33
Figure 2.6 – Flow patterns in a single corrugated channel as a function of Reynolds ( $\beta = 90^\circ$ ). ....	34
Figure 2.7 – Cross corrugated channel formed by two plates with opposite directions for a GPHE with $\beta = 65^\circ$ . ....	35
Figure 2.8 – Plates of a GPHE: a) Full geometric domain (2 channels); b) Coordinate systems and fluid inlet and outlet positions.....	36
Figure 2.9 – Geometric domain and its limits. ....	36
Figure 2.10 – Computational domain composed of four corrugated plates. ....	37
Figure 2.11 – Flow patterns for simulated plate sections ( $Re = 2000$ ): a) $\beta = 32^\circ$ and b) $\beta=67^\circ$ .....	38
Figure 2.12 – Geometry of the channels composed of two corrugated plates constituting the 16 cells units of a PHE. ....	38
Figure 2.13 – Single cell extracted from corrugated plate of a GPHE.....	39
Figure 2.14 – Shell inlet geometry model for a PSHE.....	40
Figure 2.15 – Computational domain: (a) block-type; (b) PSHE-type plate-side; (c) PSHE-type shell-side.....	40
Figure 3.1 – Multiphase flow experimental setup: (a) schematics and (b) photograph. Only the water circuit (colorful graphic in “a”) was applied for experiments. ....	45
Figure 3.2 – PSHE channel flow geometry: (a) frontal view main dimensions for one disk, (b) cross section characteristics. ....	47
Figure 3.3 – Computational domain: Case 1: corrugated plate with tubes coupled to the inlet and outlet ports for $\beta = 15^\circ \times 15^\circ$ ; Case 2: one half of the corrugated plate for $\beta = 15^\circ \times 15^\circ$ ; Case 3: one half of the corrugated plate for $\beta = 45^\circ \times 45^\circ$ ; Case 4: one half of the corrugated plate for $\beta = 45^\circ \times 15^\circ$ .....	48

Figure 3.4 – Flow inlet and outlet sections for the evaluated cases. Inlet: upper ports. Outlet: lower ports.....	49
Figure 3.5 – Hierarchy of current models of turbulence. Abbreviations: DNS = Direct Numerical Simulation; LES = Large Eddy Simulation; RANS = Reynolds-Averaged Navier Stokes; 1st order = closure of first order turbulence; 2st order = closure of second order turbulence; RST = Reynolds-Stress Tensor transport models; ARS = Algebraic Models of Reynolds-Stress; 0-, 1-, 2-Eq = Zero, one and two equation models. ....	52
Figure 3.6 – Subdivisions of the region near the wall.....	56
Figure 4.1 – Comparison between experimental and numerical data obtained for Case 1 ( $15^\circ \times 15^\circ - 1970 \leq Re \leq 4034$ ), Case 2 ( $15^\circ \times 15^\circ - 1332 \leq Re \leq 4034$ ), Case 3 ( $45^\circ \times 45^\circ - 1993 \leq Re \leq 7529$ ) and Case 4 ( $45^\circ \times 15^\circ - 1305 \leq Re \leq 6153$ ): Left: pressure loss on a pair of plates; Right: Deviation (%) between experimental and numerical data. ....	59
Figure 4.2 – Velocity field plotted on a plane situated between the plates: Case 1 (M22, SST - $Re = 4451$ ), Case 2 (M4, SST - $Re = 4451$ ), Case 3 (M21, SST - $Re = 4643$ ) and Case 4 (M21, SST - $Re = 4005$ ). Inlet port is located on the upper side of the plate. ....	62
Figure 4.3 – Velocity field distribution near the inlet (a) and outlet (b) for Chevron angle configuration of $15^\circ \times 15^\circ$ ( $Re = 3400$ ): Results predicted with numerical model – Case 1 – left side; Experimental result – right side (BECKEDORFF et al., 2019).63	63
Figure 4.4 – Flow pattern between a pair of PSHE plates for Chevron angle $15^\circ \times 15^\circ$ . Left: numerical results for Case 1 (M22, SST and $Re = 3400$ ); Right: experimental data (BECKEDORFF et al., 2019) ( $Re = 3400$ ). ....	64
Figure 4.5 – Flow pattern between a pair of PSHE plates for configurations of Chevron angle of $15^\circ \times 15^\circ$ (Case 2 (M21, SST - $Re = 4034$ )), $45^\circ \times 45^\circ$ (Case 3 - M21, SST - $Re = 4643$ ) and $45^\circ \times 15^\circ$ (Case 4 - M21, SST - $Re = 4005$ ). ....	65
Figure 4.6 – Static pressure profile on the surface of the plates for configurations of Chevron angle of $15^\circ \times 15^\circ$ (Case 1 (M22, SST - $Re = 4643$ ) and Case 2 (M4, SST - $Re = 4034$ )), $45^\circ \times 45^\circ$ (Case 3 - M21, SST – $Re = 4644$ ) and $45^\circ \times 15^\circ$ (Case 4 - M21, SST - $Re = 4005$ ).....	66
Figure 4.7 – Pressure profile for PSHE (Left: Case 1 ( $15^\circ \times 15^\circ$ ) for $Re = 4643$ ) and PHE (Right: Adapted from Han et al., 2010). ....	67

Figure 4.8 – Volumetric meshes applied for the volumetric average methodology for post-processing the results for velocity vectors: a) mesh sections indicating the reference axis y and x; b) The complete volumetric mesh. A) Refined volume mesh. B) Thickest volume mesh.....	68
Figure 4.9 – Average velocity for a plane situated between PSHE plates: a) Case 1 (M22, SST – Re = 3400), b) Case 3 (M21, SST – Re = 4643), c) Case 4 (M21, SST – Re = 4005). Left: vertical velocity. Right: horizontal velocity. ....	70
Figure 4.10 – Averaged vertical velocity profile at y = 0 m for low, medium and high Re number: Case 2 (15°x15°, SST and M11), Case 3 (45°x45°, SST and M52) and Case 4 (45°x15°, SST and M55). ....	71
Figure 4.11 – Vertical velocity profiles in the center of the channel (y = 0 [m]) for the different ranges of Re. ....	72
Figure 4.12 – Comparison between the results obtained by the numerical approach and the correlations for Cases 2, 3 and 4. Left: pressure drop as a function of Reynolds number. Right: deviation (%) from numerical data for pressure loss. ....	73
Figure 4.13 – Local: Reynolds number (a), friction factor (b) and Nusselt number (c). A) Case 2 (15°x15°). B) Case 3 (45°x45°). C) Case 4 (45°x15°). ....	76
Figure 4.14 – Local: vertical shear stress (a), vertical shear force [N] (b), horizontal shear stress [N] (c), vertical shear force [N] (d). A) Case 2 (15°x15°). B) Case 3 (45°x45°). C) Case 4 (45°x15°). ....	78

## LIST OF TABLES

Table 2.1 – Correlations for the Fanning friction factor developed for PHEs. ....	26
Table 2.2 – Correlations to the Nusselt Number developed for PHEs.....	29
Table 2.3 – Main results observed in the literature review. ....	42
Table 3.1 – Fluid properties and boundary conditions.....	50
Table A.1 – Comparison between experimental and numerical results obtained with the SST and $k - \epsilon$ models for pressure drop for the Cases 1 and 2 ( $15^\circ \times 15^\circ$ ) ( $1970 \leq Re \leq 10819$ ). ....	90
Table A.2 – Comparison between experimental and numerical results obtained with the SST and $k - \epsilon$ models for pressure drop for the Case 3 ( $45^\circ \times 45^\circ$ ) ( $1993 \leq Re \leq 7529$ ). ....	90
Table A.3 – Comparison between experimental and numerical results obtained with the SST and $k - \epsilon$ models for pressure drop for Case 4 ( $45^\circ \times 15^\circ$ ) ( $1305 \leq Re \leq 6153$ ). ....	91
Table A.4 – Comparison between experimental and numerical results obtained with the SST and $k - \epsilon$ model for pressure drop for the Cases 1 and 2 ( $15^\circ \times 15^\circ$ ) ( $1332 \leq Re \leq 4034$ ). ....	91

## **LIST OF ABBREVIATIONS**

ARS Algebraic of Reynolds-Stress  
BPHE Brazed Plate Heat Exchanger  
CFD Computational Fluid Dynamics  
CFX commercial software  
DNS Direct Numerical Simulation  
FLUENT commercial software  
GPHE Gasketed Plate Heat Exchanger  
LES Large Eddy Simulation  
PHE Plate Heat Exchanger  
PSHE Plate end Shell Heat Exchanger  
PTV Particle Tracking Velocimetry  
RANS Reynolds-Averaged Navier Stokes  
RST Reynolds-Stress Tensor  
SST Shear Stress Transport

## LIST OF SYMBOLS

$A_1$	effective area [m <sup>2</sup> ]
$a_1$	constants in SST model [-]
$A_p$	projected plate area [m <sup>2</sup> ]
$b$	corrugation depth [m]
$B$	body force [Nm <sup>-3</sup> ]
$c$	clearance between plates [mm]
$C$	constant [-]
$c_p$	specific heat at constant pressure [kJkg <sup>-1</sup> s <sup>-1</sup> ]
$C_{\varepsilon 1}, C_{\varepsilon 2}, C_{\mu}$	constants in k – $\varepsilon$ model [-]
$D$	circular duct diameter [m]
$D_e$	equivalent diameter [m]
$D_h$	hydraulic diameter [m]
$D_p$	port diameter [m]
$f$	Fanning friction factor [-]
$F_1, F_2$	blending function in SST model [-]
$f_{\mu}$	damping function [-]
$G$	mass flux [kgm <sup>-2</sup> s <sup>-1</sup> ]
$g_c$	Newton constant [-]
$G_p$	port mass flux [kgm <sup>-2</sup> s <sup>-1</sup> ]
$K$	thermal conductivity [Wm <sup>-1</sup> K <sup>-1</sup> ]
$k$	turbulence energy [m <sup>2</sup> s <sup>-2</sup> ]
$ka$	Von Karmann constant [-]
$h$	heat transfer coefficient [Wm <sup>-2</sup> K <sup>-1</sup> ]
$L$	length of channel [m]
$L_p$	vertical distance between the two ports [m]
$L_w$	plate diameter [m]
$\dot{m}$	mass flow rate [kgs <sup>-1</sup> ]
$N_{cp}$	number of channels per pass [-]
$N_p$	number of flow passages [-]
$N_t$	total number of plates [-]
$Nu$	Nusselt number [-]

$\bar{p}$	average pressure [Pa]
Pc	corrugation pitch [m]
$P_k$	turbulent energy production rate [ $\text{kgm}^{-1}\text{s}^{-3}$ ]
Pr	Número de Prandtl [-]
Q	volumetric flow rate [ $\text{kgm}^{-3}$ ]
R	duct radius [m]
Re	Reynolds number [-]
$Re_{cr}$	critical Reynolds number [-]
$R_p$	port radius [m]
$R_w$	plate radius [m]
T	temperature [K]
t	time [s]
$S_1$	modulus of the average shear rate [-]
$\bar{S}_{ji}$	average strain-rate tensor [-]
$\bar{u}$	average velocity [ $\text{ms}^{-1}$ ]
u	velocity [ $\text{ms}^{-1}$ ]
U	centerline velocity [ $\text{ms}^{-1}$ ]
$u^+$	Non-dimensional velocity [-]
$u^*$	friction velocity [ $\text{ms}^{-1}$ ]
y	wall distance [m]
$y^+$	Non dimensional wall distance [-]

#### Subscripts

m, avg	average
i, j, w	refers to an axis [x, y, z]
in, o	inlet, outlet

#### Greek letters

$\beta$	Chevron angle [ $^\circ$ ]
$\mu$	fluid dynamic viscosity [ $\text{Nsm}^{-2}$ ]
$\mu_t$	turbulent viscosity [ $\text{Nsm}^{-2}$ ]
$\Delta p$	pressure drop [Pa]
$\varepsilon$	turbulence energy dissipation rate [ $\text{m}^2\text{s}^{-3}$ ]

$\omega$	turbulence frequency [xx]
$\rho$	density [kgm <sup>-3</sup> ]
$k - \varepsilon$	$\varepsilon$ based turbulence model [-]
$\phi$	any property [-]
$\emptyset_1, \emptyset_2$	constants in SST model [-]
$\varphi$	area enlargement factor [-]
$\tau_w$	wall shear stress [Nm <sup>2</sup> ]
$\overline{\tau_{ij}}$	average Reynolds stress tensor [-]
$\delta$	plate thickness [mm]
$\sigma_k, \sigma_\varepsilon$	constants in $k - \varepsilon$ model [-]

## CONTENTS

<b>1</b>	<b>INTRODUCTION.....</b>	<b>15</b>
1.1	OVERVIEW.....	15
1.2	OBJETIVES .....	16
<b>1.2.1</b>	<b>Main Objective .....</b>	<b>16</b>
<b>1.2.2</b>	<b>Specific Objectives.....</b>	<b>16</b>
1.3	JUSTIFICATION AND CONTRIBUTIONS .....	17
1.4	STRUCTURE OF THE PAPER .....	17
<b>2</b>	<b>LITERATURE REVIEW.....</b>	<b>18</b>
2.1	TYPES OF PLATE HEAT EXCHANGERS - PHE.....	18
2.2	PLATE GEOMETRICAL CHARACTERISTICS .....	21
<b>2.2.1</b>	<b>Chevron Corrugation and Enlargement Factor.....</b>	<b>21</b>
2.3	PLATE GEOMETRICAL CHARACTERISTICS .....	22
<b>2.3.1</b>	<b>Reynolds Number .....</b>	<b>22</b>
<b>2.3.2</b>	<b>Friction Factor .....</b>	<b>24</b>
<b>2.3.3</b>	<b>Nusselt Number .....</b>	<b>27</b>
<b>2.3.4</b>	<b>Pressure Drop .....</b>	<b>29</b>
2.4	EXPERIMENTAL AND NUMERICAL RESULTS – LITERATURE.....	30
<b>3</b>	<b>METHODOLOGY.....</b>	<b>42</b>
3.1	PLATE VALIDATION.....	42
<b>3.1.1</b>	<b>PSHE Corrugated Plate.....</b>	<b>42</b>
3.1.1.1	Experimental setup.....	42
3.1.1.1.1	<i>Test rig.....</i>	<i>42</i>
3.1.1.1.2	<i>Test section.....</i>	<i>44</i>
3.1.1.2	Numerical setup.....	45
3.1.1.2.1	<i>Boundary conditions and models .....</i>	<i>47</i>
3.2	NUMERICAL MODELS.....	48

3.2.1	<b>Governing Equations .....</b>	<b>48</b>
3.2.2	<b>The Standard <math>k - \epsilon</math> Model .....</b>	<b>50</b>
3.2.3	<b>The SST Model (Shear – Stress – Transport).....</b>	<b>51</b>
3.2.4	<b>Wall Treatment.....</b>	<b>52</b>
4	<b>RESULTS AND DISCUSSION.....</b>	<b>56</b>
4.1	<b>PART I – EXPERIMENTAL VALIDATION AND DISCUSSION.....</b>	<b>56</b>
4.1.1	<b>Total Pressure Loss for a Pair of PSHE Plates with Chevron Angle of <math>15 \times 15^\circ</math>, <math>45 \times 45^\circ</math> and <math>45 \times 15^\circ</math> .....</b>	<b>56</b>
4.1.2	<b>Velocity Field .....</b>	<b>59</b>
4.2	<b>PART II – NUMERICAL RESULTS .....</b>	<b>62</b>
4.2.1	<b>Static Pressure Profile on the Surface Across Plates .....</b>	<b>62</b>
4.2.2	<b>Velocity, Re Number, Nu Number and Friction Factor .....</b>	<b>64</b>
4.2.2.1	Volumetric meshes .....	64
4.2.2.2	Velocity profile.....	65
4.2.3	<b>Correlations .....</b>	<b>69</b>
4.2.4	<b>Reynolds, Friction Factor and Nusselt Numbers .....</b>	<b>71</b>
4.2.5	<b>Shear Forces.....</b>	<b>74</b>
5	<b>CONCLUSIONS.....</b>	<b>78</b>
5.1	<b>MAIN CONCLUSIONS .....</b>	<b>78</b>
5.2	<b>SUGGESTIONS FOR FUTURE WORK.....</b>	<b>79</b>
	<b>BIBLIOGRAPHY .....</b>	<b>81</b>
	<b>APPENDIX A – Numerical results .....</b>	<b>87</b>

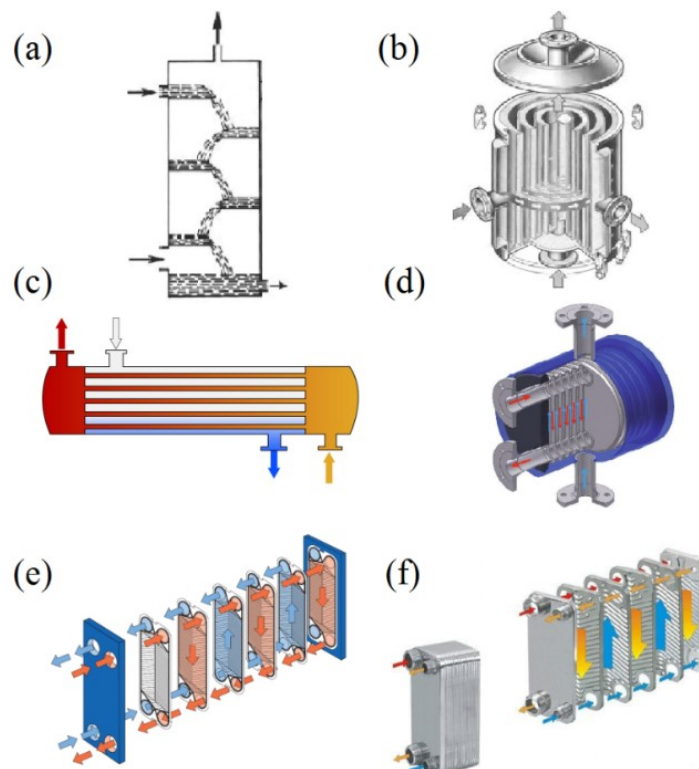


## 1 INTRODUCTION

### 1.1 OVERVIEW

A heat exchanger is a heat transfer device which provides the exchange of thermal energy between two or more fluids present in a process. The applicability of heat exchangers is generalized, justifying the various configurations available. The range of existing models can be classified according to some basic criteria such as the process of heat transfer (direct transfer and indirect transfer); recuperators or regenerators; construction geometry (tubes, plates and extended surfaces); mechanisms of heat transfer; flow patterns (flow patterns, flow contours and cross flows) (SHAH; SEKULIC, 2003). Some of these heat exchangers are exemplified in Figure 1.1.

Figure 1.1 – Types of heat exchangers: (a) direct transfer; (b) spiral plate; (c) shell-and-tube; (d) plate and shell; (e) gasketed plate; (f) brazed plate.



Source: Adapted from Kakaç, Liu and Pramuanjaroenkij (2012); GESMEX (2007); Alfa Laval (2008).

Plate type heat exchangers are examples of compact heat exchangers (see Figure 1.1 c to f). A specific type of plate exchanger is called Plate-Shell Heat Exchanger (PSHE) and it is the focus of this study. Further details on this equipment are presented later on section 2.2.

## 1.2 OBJETIVES

### 1.2.1 Main Objective

The main objective of this study is to analyze the hydrodynamic behavior of the flow between plates of a PSHE for different configurations of Chevron angle with a tridimensional turbulent numerical model. Specific objectives are as follows.

### 1.2.2 Specific Objectives

- Present a review of the current state of the art of PHE and PSHE heat exchangers with respect to flow behavior information and numerical modeling;
- Simulate cold water flow in the inner channel of a pair of PSHE plates with a Chevron angle of  $15^\circ \times 15^\circ$ ,  $45^\circ \times 45^\circ$  and  $15^\circ \times 45^\circ$  for  $1331 \leq Re \leq 4034$ ,  $1993 \leq Re \leq 7529$  and  $1305 \leq Re \leq 6153$ , respectively;
- Validate the numerical model of internal flow for total pressure drop, identifying which model of turbulence and simplification of geometry is the most indicated, through experimental data;
- Analyze the average velocity profile for the flow between a pair of plates with a Chevron angle of  $15^\circ \times 15^\circ$ ,  $45^\circ \times 45^\circ$  and  $15^\circ \times 45^\circ$  for Re numbers  $2000 < Re$ ,  $Re \approx 4000$  e  $Re > 6000$ ;
- Identify the limitations in the models;
- Identify the pressure drop correlations developed for the PHEs that best describe the internal flow behavior for a pair of PSHE plates based on the numerical results obtained.

### 1.3 JUSTIFICATION AND CONTRIBUTIONS

Up to the date the number of papers focused on PSHE heat exchangers in the literature is scarce, as will be shown in the next section. Very few data presenting velocity profiles and flow behavior between plates is available for PSHE and yet for limited configuration of Chevron angle and Re number. However there are a good number of studies applied to PHEs, with experimental analyzes more predominant in the literature. Nevertheless, numerical approaches for PHEs show a lack of data for complete internal flow between plates due to the computational cost required for these arrangements, usually presenting a methodology focused on small elements that compose the device such as elementary cells formed by a piece of plates. For that reason an approach based on experimental correlations is more commonly applied to predict Nu number, friction factor and pressure drop on PHE.

A more detailed assessment of fluid dynamics behavior in a PSHE by using the numerical approach is the most significant contribution provided by this study. As PSHEs have circular plates some correlations usually adopted in the PHE analyzes, which have rectangular plates, may not be directly applied but may be used with corrections. Determining these characteristics gives a better understanding of the operation of this type of heat exchanger, providing a database for further investigations.

### 1.4 STRUCTURE OF THE PAPER

This following text is divided into more 4 chapters. Chapter 2 describes the PSHE and presents a review containing the main experimental and numerical results found in the literature concerning PSHEs and PHEs. Chapter 3 presents the mathematical models, numerical techniques, and methodology applied for this study. The results and following discussions are presented in Chapter 4. Finally, Chapter 5 compiles the study and presents the conclusions obtained.



## 2 LITERATURE REVIEW

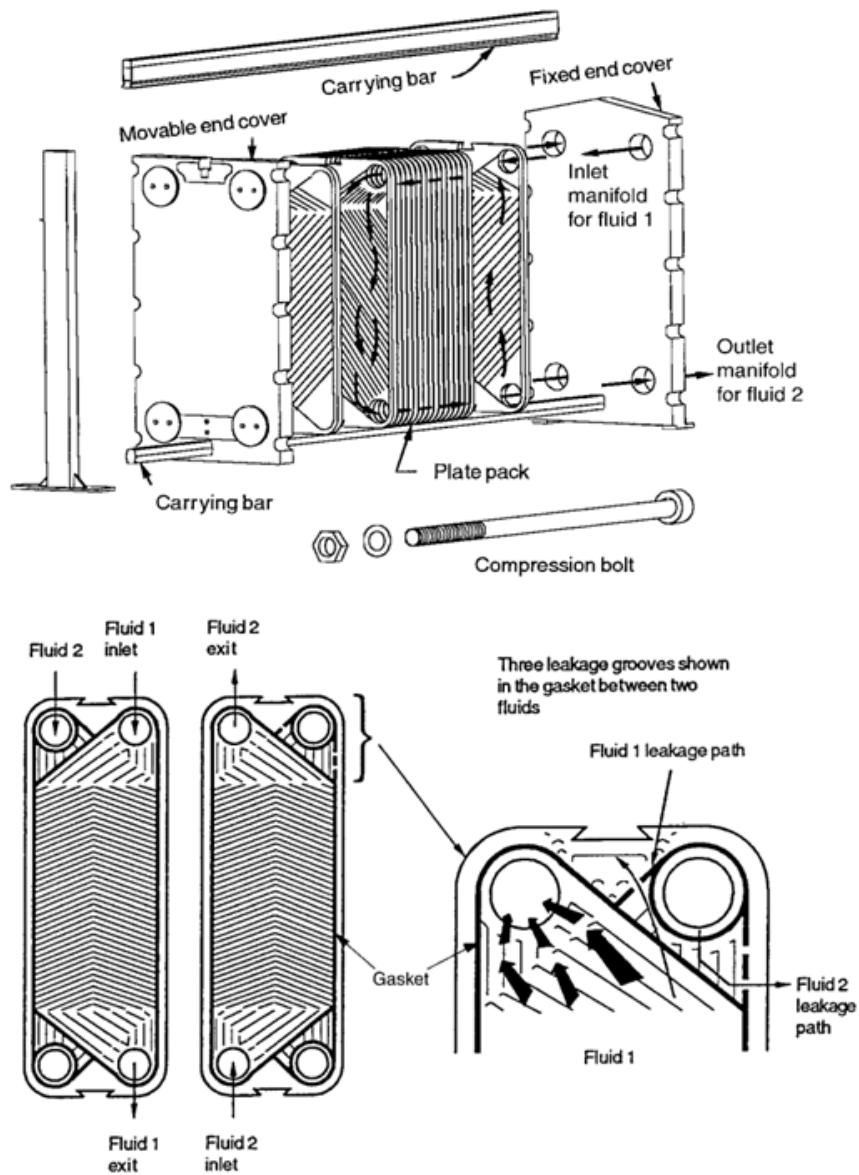
In this chapter a brief description of the plate heat exchanger type (PHE) is presented, as well as the characteristics and parameters that define a plate heat exchanger. Its subdivisions are presented and the PSHE is discussed. A review of the existing literature focused on PHEs and PSHEs is presented at the end of this chapter.

### 2.1 TYPES OF PLATE HEAT EXCHANGERS (PHE)

The PHEs have their main heat exchange surface made by thin plates, formed by a wave pattern with the object to promote turbulent flow and consequently increase the heat transfer efficiency. These heat exchangers do not regularly operate with elevated pressures and temperatures or high pressure temperatures differences between working fluids. However, they have great versatility in easily changing their thermal capacity by adding or removing plates from the assembly when the heat load required by the process changes. In addition, the ability to disassemble and reassemble the plate pack facilitates maintenance and cleaning. This class is subdivided according to the way in which the plates are sealed, which depends on the necessary stiffness (THULUKKANAM, 2013). One interesting advantage is PHEs have less weight and volume (30% and 20% respectively) for the same performance with the same effective area of heat transfer than a classic shell-tube heat exchanger (MCGERORGE, 1991).

A Gasketed Plate Heat Exchanger (GPHE) has gaskets that separate the working fluids. The gaskets prevent leaks and allows to seal the channels between the plates, directing the fluids to alternate channels and ensuring that the two media do not mix. The plate assemblies are joined by means of compression bolts, connecting the end plates as shown in Figure 2.1 (SHAH; SUBBARAO; MASHELKAR, 1988).

Figure 2.1 – Gasket plate heat exchanger.



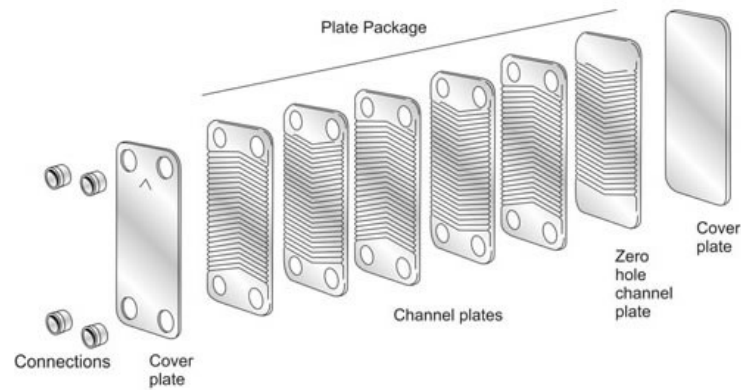
Source: Adapted from Shah (2003).

The operating range of these heat exchangers is restricted to temperatures between 40 and 180 ° C and pressure limits varying from 25 to 30 bar. These restrictions are imposed by the gasket material, which cannot withstand harsher conditions of temperature and pressure or corrosive fluids (THUKUKANAM, 2013).

The gasket is replaced by a joint produced by the brazing method on the Brazed Plate Heat Exchangers (BPHE) (Figure 2.2). Completely fixed plates eliminate end plates, gaskets and compression bolts, which makes the heat exchanger lighter and more compact. The

stronger joint also allows a greater range of operation, with temperatures and pressures above 400°C and 30 bar respectively (WANG et al., 2007).

Figure 2.2 – Brazed Plate Heat Exchangers.



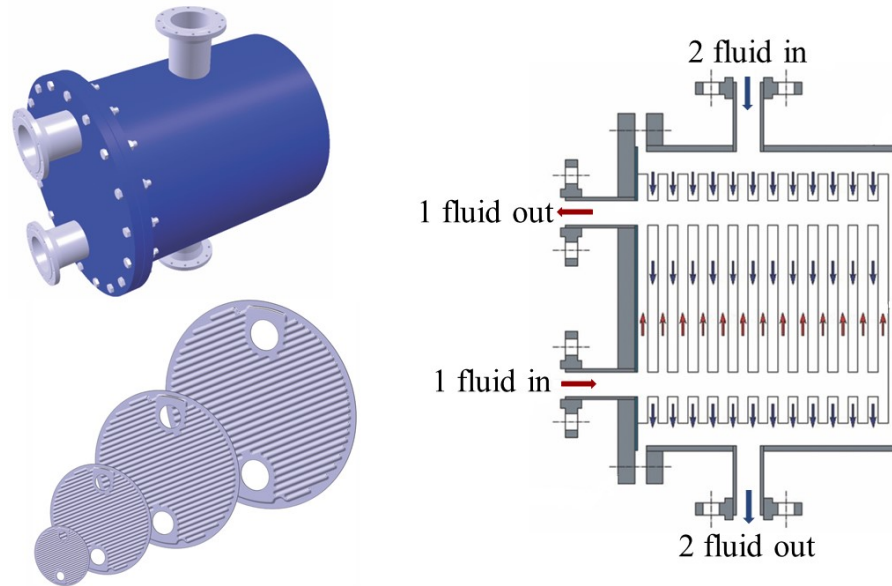
Source: Gullapalli (2013).

One of the biggest disadvantages of the BPHE is in the cleaning of the plates that can only be carried out by chemical agents, since the plates cannot be separated. Another disadvantage is its size; usually these heat exchangers have a length of less than 1 m due to the limited sizes of the brazing furnaces (WANG et al., 2007).

Welded heat exchangers can be subdivided into another two classes, either semi-welded or fully welded. The semi-welded are composed of pairs of welded plates, a process usually performed by laser, where gaskets are used to assemble the plate assemblies. When fully welded, the plate assembly consists of plates welded one by one, alternating the grooves. The plate pack is then mounted between the end plates and compressed by screws. Due to the fact that they do not use gaskets, fully welded models allow higher pressure and temperature ranges (SHAH; SEKULIC, 2003).

Within the fully welded heat exchanger class is the Plate and Shell Heat Exchanger (PSHE). This heat exchanger is composed of a packet of welded plates and a conventional shell. The plate packet itself is composed of several corrugated plates welded in its perimeter by a laser welding process. The schematic drawing of heat exchanger is presented in Figure 2.3.

Figure 2.3 – Schematic of a PSHE.



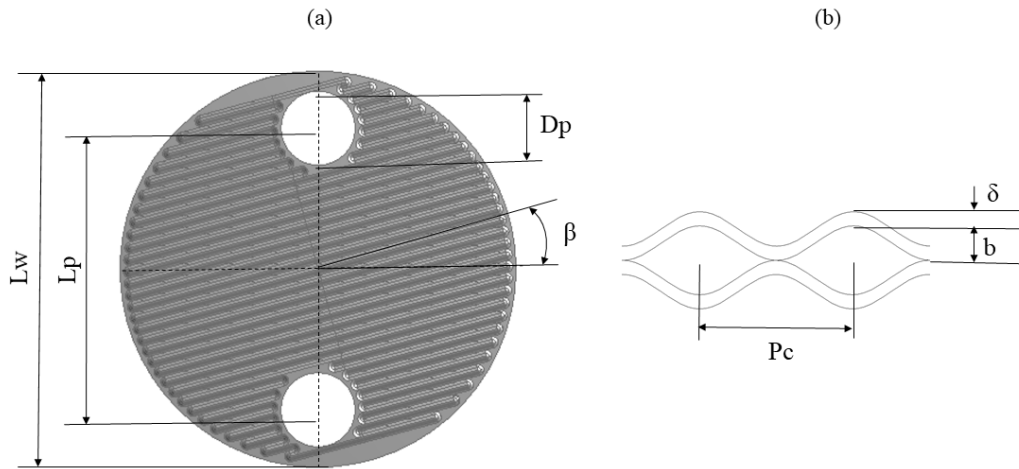
Source: Adapted from Euro Heat LTD (2019).

Due to the characteristic of a cylindrical casing, the design pressures are higher with respect to the other models of plate heat exchangers. The units sold by Alfa Laval, named AlfaDisc, are designed to operate at pressures up to 170 bar, operating within a temperature range from  $-60\text{ }^{\circ}\text{C}$  to temperatures above  $890\text{ }^{\circ}\text{C}$  (ALFA LAVAL, 2008) (VAHTERUS OY, 2017).

## 2.2 PLATE GEOMETRICAL CHARACTERISTICS

The circular configuration and the absence of the gasket are the characteristics that differ the plates of a PSHE from the plates of the PHEs, since the other geometric parameters are considered corresponding between the plates of PHEs and PSHEs. Figure 2.4 shows the front view design of a PSHE plate indicating the port diameter ( $D_p$ ), the distance between the centers of the fluid inlet and outlet ports ( $L_p$ ), the plate diameter ( $L_w$ ), and other characteristics of the corrugated plate as Chevron angle ( $\beta$ ), corrugation pitch ( $P_c$ ), corrugation depth ( $b$ ) and plate thickness ( $\delta$ ).

Figure 2.4 – Plate geometry: Plate design of PSHE (a); Characteristics of the plate wave (b).



Source: Author (2019).

Corrugation of the plate may occur in a number of ways. However, over the years, the Chevron wave pattern has proven to be a more efficient and popular arrangement, and is offered in quite similar ways by suppliers (MARTIN, 1996).

### 2.2.1 Chevron Corrugation and Enlargement Factor

The corrugated pattern has a  $\beta$  angle (Chevron angle) (figure 2.4), evaluated as the angle between the corrugated line and the horizontal direction. The Chevron pattern has four main effects (KAKAÇ; LIU; PRAMUANJAROENKIJ, 2012) (LIU; TSAI, 2010): it increases the level of flow turbulence; increases the effective area of heat transfer; increases the rigidity of the plate pack; and induces a turbulent flow with high shear forces in the wall which reduces fouling.

The efficiency of the heat transfer is strongly related to the  $\beta$  angle. On the other hand, the performance of a plate will also depend on the area enlargement factor ( $\varphi$ ), which is defined as the ratio of the actual effective area as specified by manufacturer,  $A_1$ , to the projected plate area  $A_p$  (KAKAÇ; LIU; PRAMUANJAROENKIJ, 2012):

$$\varphi = \frac{A_1}{A_p}. \quad (2.1)$$

For a circular plate  $A_p$  can be approximated as:

$$A_p = \pi R W^2 - 2\pi R p^2, \quad (2.2)$$

where  $R W$  is the plate radius and  $R p$  is the port radius.

## 2.3 PLATE GEOMETRICAL CHARACTERISTICS

### 2.3.1 Reynolds Number

In fluid mechanics, the Reynolds number characterizes the flow regime. The flow in a duct can be laminar or turbulent, depending on the flow conditions. The transition from laminar to turbulent flow does not occur suddenly, the transition regime is identified for certain velocity ranges. For circular tubes the transition flow exists for  $2300 \leq Re \leq 10000$ . The transition depends on the input configuration, flow path geometry, surface roughness, natural convection effects, flow pulsation, even the change of viscosity when there are great heating rates. In addition, noise and vibration outside the duct wall can influence  $Re_{cr}$ , defined as the Reynolds number of transition between the laminar and turbulent regimes. For a PHE, the transition flow starts between  $10 \leq Re \leq 200$ , depending on the geometry and operating conditions (SHAH; SEKULIC, 2003).

For flow in a circular tube, the Reynolds number is defined as:

$$Re = \frac{\rho u_m D}{\mu}, \quad (2.3)$$

where  $\rho$  is the fluid density,  $u_m$  is the average velocity,  $D$  is the tube diameter and  $\mu$  is the dynamic viscosity of the fluid. For non-circular pipe flow, the Reynolds number as well as the other correlations are based on the hydraulic diameter  $D_h$  defined as (KAKAÇ; LIU; PRAMUANJAROENKIJ, 2012):

$$D_h = \frac{4 \times \text{channel flow area}}{\text{wetted perimeter}} = \frac{4b(Lw)}{2(b+Lw\varphi)} \approx \frac{2b}{\varphi}. \quad (2.4)$$

Considering the flow through a channel formed by the undulations between two plates of a PSHE, with the approximation  $b \ll Lw$ :

$$D_e = 2b, \quad (2.5)$$

were  $D_e$  is the equivalent diameter.

When the definition of the equivalent diameter is adopted, the projected area of the plate must be used in the heat transfer calculations, since its formulation does not take into account the plate area magnification factor (as in the definition of  $D_h$ ).

Then for a PHE the Reynolds number is given by:

$$Re = \frac{\rho u_m D_h}{\mu} = \frac{G D_h}{\mu}, \quad (2.6)$$

where the mass flow in the channel can be defined as:

$$G = \frac{\dot{m}}{N_{cp} b L_w}, \quad (2.7)$$

where  $\dot{m}$  is the mass flow rate and  $N_{cp}$  is the number of channels per pass (one channel is the space between two plates,  $N_{cp}$  is the number of channels contained in a group of channels in which flow is in the same direction):

$$N_{cp} = \frac{N_t - 1}{2N_p}, \quad (2.8)$$

where  $N_t$  is the total number of plates and  $N_p$  is the number of flow passages.

### 2.3.2 Friction Factor

The ratio between the shear stress at the wall and the kinetic energy of the flow per unit volume is defined as the Fanning friction factor (Equation 2.9), given by

$$f = \frac{2\tau_w}{\rho u_m^2}, \quad (2.9)$$

where  $\tau_w$  is the wall shear stress:

$$\tau_w = \mu \left( \frac{\partial u}{\partial y} \right)_{y=0}, \quad (2.10)$$

where  $\left( \frac{\partial u}{\partial y} \right)_{y=0}$  is the velocity gradient on the y direction at the surface ( $y = 0$ ).

In the core of a heat exchanger, depending on the geometry surface, there may be drag and internal expansion / contraction, such as in a tube bank or a perforated plate core, included in the experimental value of the friction factor (SHAH; SEKULIC, 2003). Thus, many correlations were developed for different GPHEs in order to better define this characteristic. Table 2.1 presents correlations for the Fanning friction factor for PHE available in the literature.

Table 2.1 – Correlations for the Fanning friction factor developed for PHEs.

Authors	Correlations	Conditions	Equation	
Savostin and Tikhonov (1970)	$f = 6.25(1 + 0.95\Psi^{1.72})\Phi^{1.84}Re^{-0.84}$ $f = 0.925[0.62 + 0.38 \cos(2.6\Psi)]\Phi^{1+a2}Re^{-a2}$ $a2 = 0.53[0.58 + 0.42\cos(1.87\Psi)]$	$200 \leq Re/\Phi \leq 600$ $600 \leq Re/\Phi \leq 4000$	Air flows $57^\circ < \beta < 90^\circ$ $200 < Re < 4000$ $\Psi = p-2\beta$ ; $\beta$ in radian	(2.11)
Cooper (1974)	$f = \frac{\Delta_P \rho g D_h D_h}{2G^2 L}$	-	-	(2.12)
Price and Fattah (1978)	$f = \frac{\Delta_P D_h}{2\rho v^2 L}$	$300 < Re < 3000$	-	(2.13)

Authors	Correlations	Conditions	Equation																																																							
Tovazhnyanski, Kapustenko and Tsubulnik (1980)	$f = 0.085 \exp[1.52 \tan \Psi] Re^{-(0.25 - 0.06 \tan \beta)}$	$\beta = 30^\circ; 45^\circ; 60^\circ$ $2000 < Re < 25000$ $\Psi = p - 2\beta; \beta$ in radian	(2.14)																																																							
Kumar (1984)	$f = C1/(Re)^p$	<table border="1"> <thead> <tr> <th><math>\beta</math></th> <th>Re</th> <th>C1</th> <th>p</th> </tr> </thead> <tbody> <tr> <td rowspan="3"><math>\leq 30^\circ</math></td> <td><math>\leq 10</math></td> <td>50.0</td> <td>1.0</td> </tr> <tr> <td><math>&gt;10</math></td> <td>19.40</td> <td>0.589</td> </tr> <tr> <td><math>&gt;100</math></td> <td>2.990</td> <td>0.183</td> </tr> <tr> <td rowspan="3"><math>45^\circ</math></td> <td><math>&lt;15</math></td> <td>47.0</td> <td>1.0</td> </tr> <tr> <td>15-300</td> <td>18.29</td> <td>0.652</td> </tr> <tr> <td><math>&gt;300</math></td> <td>1.441</td> <td>0.206</td> </tr> <tr> <td rowspan="3"><math>50^\circ</math></td> <td><math>&lt;20</math></td> <td>34.0</td> <td>1.0</td> </tr> <tr> <td>20-300</td> <td>11.25</td> <td>0.631</td> </tr> <tr> <td><math>&gt;300</math></td> <td>0.772</td> <td>0.161</td> </tr> <tr> <td rowspan="3"><math>60^\circ</math></td> <td><math>&lt;40</math></td> <td>24.0</td> <td>1.0</td> </tr> <tr> <td>40-400</td> <td>3.24</td> <td>0.457</td> </tr> <tr> <td><math>&gt;400</math></td> <td>0.760</td> <td>0.215</td> </tr> <tr> <td rowspan="3"><math>\leq 65^\circ</math></td> <td><math>&lt;50</math></td> <td>24.0</td> <td>1.0</td> </tr> <tr> <td>50-500</td> <td>2.80</td> <td>0.451</td> </tr> <tr> <td><math>&gt;500</math></td> <td>0.639</td> <td>0.213</td> </tr> </tbody> </table>	$\beta$	Re	C1	p	$\leq 30^\circ$	$\leq 10$	50.0	1.0	$>10$	19.40	0.589	$>100$	2.990	0.183	$45^\circ$	$<15$	47.0	1.0	15-300	18.29	0.652	$>300$	1.441	0.206	$50^\circ$	$<20$	34.0	1.0	20-300	11.25	0.631	$>300$	0.772	0.161	$60^\circ$	$<40$	24.0	1.0	40-400	3.24	0.457	$>400$	0.760	0.215	$\leq 65^\circ$	$<50$	24.0	1.0	50-500	2.80	0.451	$>500$	0.639	0.213	single phase water, $\Phi = 1.17$	(2.15)
$\beta$	Re	C1	p																																																							
$\leq 30^\circ$	$\leq 10$	50.0	1.0																																																							
	$>10$	19.40	0.589																																																							
	$>100$	2.990	0.183																																																							
$45^\circ$	$<15$	47.0	1.0																																																							
	15-300	18.29	0.652																																																							
	$>300$	1.441	0.206																																																							
$50^\circ$	$<20$	34.0	1.0																																																							
	20-300	11.25	0.631																																																							
	$>300$	0.772	0.161																																																							
$60^\circ$	$<40$	24.0	1.0																																																							
	40-400	3.24	0.457																																																							
	$>400$	0.760	0.215																																																							
$\leq 65^\circ$	$<50$	24.0	1.0																																																							
	50-500	2.80	0.451																																																							
	$>500$	0.639	0.213																																																							
Focke, Zachariades and Olivier (1985)	$f = \begin{cases} 114.4/Re & \text{Laminar(theory)} \rightarrow \beta = 0^\circ \\ 0.552Re^{-0.263} & 8000 < Re < 56000 \rightarrow \beta = 0^\circ \\ 0.37 + 230/Re & 260 < Re < 3000 \rightarrow \beta = 30^\circ \\ 3.59Re^{-0.263} & 3000 < Re < 50000 \rightarrow \beta = 30^\circ \\ 1.21 + 367/Re & 150 < Re < 1800 \rightarrow \beta = 45^\circ \\ 5.84Re^{-0.177} & 1800 < Re < 30000 \rightarrow \beta = 45^\circ \\ 5.03 + 755/Re & 90 < Re < 400 \rightarrow \beta = 60^\circ \\ 26.8Re^{-0.209} & 400 < Re < 16000 \rightarrow \beta = 60^\circ \\ 19.0 + 764/Re & 110 < Re < 500 \rightarrow \beta = 72^\circ \\ 132Re^{-0.296} & 500 < Re < 12000 \rightarrow \beta = 72^\circ \\ 140Re^{-0.28} & 130 < Re < 3700 \rightarrow \beta = 80^\circ \\ 5.63 + 1280/Re & 200 < Re < 3000 \rightarrow \beta = 90^\circ \\ 63.8Re^{-0.289} & 3000 < Re < 16000 \rightarrow \beta = 90^\circ \end{cases}$	$\beta = 30^\circ; 45^\circ; 60^\circ;$ $72^\circ; 80^\circ; 90^\circ$ $90 < Re < 56000$	(2.16)																																																							
Chisholm and Wanniarachchi (1992)	$f = 0.8Re^{-0.25} \Phi^{1.15} ((90 - \beta)/30)^{3.6}$	$30^\circ \leq \beta \leq 80^\circ$ $100 < Re < 4000$	(2.17)																																																							
Heavner, Kumar and Wanniarachchi (1993)	$f = \begin{cases} 1.458\Phi^{1.0838} Re^{-0.0838} & \beta = 45^\circ/0^\circ \\ 1.441\Phi^{1.1353} Re^{-0.1353} & \beta = 67^\circ/0^\circ \\ 0.687\Phi^{1.1405} Re^{-0.1405} & \beta = 45^\circ/45^\circ \\ 0.545\Phi^{1.1555} Re^{-0.1555} & \beta = 67^\circ/45^\circ \\ 0.490\Phi^{1.1814} Re^{-0.1814} & \beta = 67^\circ/67^\circ \end{cases}$	$400 < Re < 10000$ $3.3 < Pe < 5.9$	(2.18)																																																							
Talik and Swanson (1995)	$f = \begin{cases} 12.065Re^{-0.74} & 10 < Re < 80; \text{water/glicol} \\ 0.3323Re^{-0.042} & 1450 < Re < 11460; \text{water} \end{cases}$	$\Phi = 1.22$ $Dh = 4.65$ mm $Lw = 0.346$ m $t = 0.61$ mm $\beta = 30^\circ$ $10 < Re < 11460$	(2.19)																																																							
Wanniarachchi et al. (1995)	$f = \frac{\Delta p \rho g_c D_h}{2G^2 L} (\mu/\mu_w)^{0.17}$	$\Theta = 90^\circ - \beta$ gc = Newton constant = 1 (SI)	(2.20)																																																							
Muley and Manglik (1995)	$f = \begin{cases} 51.5/Re & Re < 16 \\ 17.0Re^{-0.6} & 16 \leq Re \leq 100 \\ 2.48Re^{-0.2} & Re \geq 800 \end{cases}$	$\beta = 30^\circ$	(2.21)																																																							

Authors	Correlations	Conditions	Equation
Martin (1996)	$Re_h = \Phi Re$ $\frac{1}{\sqrt{f}} = \frac{\cos\left(\frac{\pi}{2} - \beta\right)}{\left(0.18 \tan\left(\frac{\pi}{2} - \beta\right) + 0.36 \sin\left(\frac{\pi}{2} - \beta\right) + f_0 / \cos\left(\frac{\pi}{2} - \beta\right)\right)^{1/2} + \frac{1 - \cos\left(\frac{\pi}{2} - \beta\right)}{\sqrt{3.8f_1}}$ $Re_h < 2000 = \begin{cases} f_0 = 64/Re_h \\ f_1 = 597/Re_h + 3.85 \end{cases}$ $Re_h \geq 2000 = \begin{cases} f_0 = (1.8 \log_{10} Re_h - 1.5)^{-2} \\ f_1 = 39/Re_h^{0.289} \end{cases}$	$\beta$ in radian	(2.22)
Muley and Manglik (1997)	$f = \begin{cases} [(40.32/Re)^5 + (8.12Re^{-0.5})^5]^{0.2} & 2 \leq Re \leq 200 \\ 1.274Re^{-0.15} & Re \geq 1000 \end{cases}$	$\beta = 30^\circ$ and $60^\circ$ ( $\beta_{avg} = 45^\circ$ )	(2.23)
Greth (1999)	$f = \frac{\Delta_p D_e}{2\rho v^2 L}$	$40 < Re < 20000$ Function of $\beta$ ; $\lambda/b$	(2.24)
Muley and Manglik (1999)	$f = \frac{\Delta_p D_e}{2(\dot{m}/NA_c)^2 L_p}$	Function of $\beta$ and $\Phi$ $Re > 1000$ $30^\circ < \beta < 60^\circ$ $1 < \Phi < 1.5$	(2.25)
Wang and Sundén (2003)	$\frac{1}{\sqrt{f}} = \frac{\cos(90 - \beta)}{(0.045 \tan(90 - \beta) + 0.09 \sin(90 - \beta) + f_0 / \cos(90 - \beta))} + \frac{1 - \cos(90 - \beta)}{\sqrt{3.8f_1}}$ $Re_h < 2000 = \begin{cases} f_0 = 16/Re \\ f_1 = 149/Re + 0.9625 \end{cases}$ $Re_h \geq 2000 = \begin{cases} f_0 = (1.8 \ln(Re) - 3.0)^{-2} \\ f_1 = 9.75/Re^{0.289} \end{cases}$	$10^\circ \leq \beta \leq 80^\circ$	(2.26)
Rao, Sunden and Das (2005)	$f = 21.41 Re^{-0.301}$	$\beta = 30^\circ$ $1000 < Re < 7000$	(2.27)
Kanaris, Mouza and Paras (2005)	$f = 0.27 Re^{-0.14}$	$\beta = 45^\circ$ $900 < Re < 1400$	(2.28)
Kanaris et al. (2006)	$f = \frac{\Delta_p D_h}{2\rho v^2 L}$	$\beta = 60^\circ$ $700 < Re < 1700$	(2.29)
Abu-Khader (2007)	$f = \frac{2\Delta_p D_h}{\rho v^2 L_p}$	Modified by Martin	(2.30)
Dovic' et al. (2009)	$f = \frac{C}{Re_{sine}} + B$	Modified by Martin	(2.31)
Gherasim et al. (2011a)	$f = \frac{2\Delta_p D_e}{\rho v^2 L_c}$	$\beta = 60^\circ$	(2.32)
Akturk et al. (2015)	$f = 60550 Re^{-1.72} + 0.4299$	$\beta = 30^\circ$ $450 < Re < 5250$	(2.33)
Turk, Aradag and Kakac (2016)	$f = 386500 Re^{-2.112} + 0.7299$	$\beta = 27.5^\circ$ and $62.5^\circ$ ( $\beta_{avg} = 45^\circ$ ) $Re < 4500$	(2.34)
Jin and Hrnjak (2016)	$f = \frac{\rho D_e \Delta P_{core}}{2L_p [\dot{m}/A_{cs}]^2}$	-	(2.35)
Elmaaty, Kabeel and Mahgoub (2017)	$f = \frac{\rho \Delta_p D_e}{2L_p G^2}$	-	(2.36)
Kumar and Singh (2017)	$f = 2.573 Re^{-0.1513}$	$\beta = 60^\circ$ $800 < Re < 4300$	(2.37)

Source: Author (2019).

### 2.3.3 Nusselt Number

The Nusselt number (Nu) is a dimensionless number that applied to quantified the heat transfer through convection. It is defined for an internal flow as the ratio between the convection heat transfer coefficient (h) and the pure molecular thermal conductivity (K / D) (SHAH; SEKULIC, 2003):

$$Nu = \frac{hD}{K}. \quad (2.38)$$

It represents a way to measure the efficiency of heat transfer, the larger the number of Nu, the more effective the convective heat transfer will be. Like the friction factor, the Nusselt number is strongly dependent on the thermal boundary conditions and the flow path geometry. Table 2.2 presents correlations for the Nusselt Number for PHE available in the literature.

Table 2.2 – Correlations to the Nusselt Number developed for PHEs.

Authors	Correlations	Conditions	Equation					
Savostin and Tikhonov (1970)	$Nu = 1.26[(0.62 + 0.38\cos(2.3\Psi)]\Phi^{1-a_1}Pr^{1/3}Re^{a_1}$ $a_1 = 0.22[1 + 1.1\Psi^{1.5}]$ $Nu = 0.072e^{0.5\Psi + 0.17\Psi^2}\Phi^{0.33}Pr^{1/3}Re^{0.67}$	$200 \leq Re/\Phi \leq 600$ $600 \leq Re/\Phi \leq 4000$	Air flows $57^\circ < \beta < 90^\circ$ $200 < Re < 4000$ $\Psi = p - 2\beta$ ; $\beta$ in radian	(2.39)				
Okada et al. (1972)	$Nu = 0.1528Re^{0.66}Pr^{0.4}$	$400 \leq Re \leq 15000$		(2.40)				
Tovazhnyanski, Kapustenko and Tsibulnik (1980)	$Nu = 0.051e^{[0.64\tan\Psi]}Re^{0.73}Pr^{0.43}(Pr/Pr_w)^{0.25}$	$\beta = 30^\circ; 45^\circ; 60^\circ$ $2000 < Re < 25000$ $\Psi = p - 2\beta$ ; $\beta$ in radian		(2.41)				
Kumar (1984)	$Nu = C1Re^mPr^{0.33}\left(\frac{\mu}{\mu_w}\right)^p$	$\beta \leq 30^\circ$ $\beta = 45^\circ$ $\beta = 50^\circ$ $\beta = 60^\circ$ $\beta \leq 65^\circ$	$Re \leq 10$ $Re > 10$ $Re < 10$ $10-100$ $Re > 100$ $20-300$ $Re > 300$ $20-400$ $Re > 400$ $20-500$ $Re > 500$	$C1$ $0.718$ $0.348$ $0.718$ $0.400$ $0.300$ $0.630$ $0.291$ $0.130$ $0.562$ $0.306$ $0.457$ $0.215$ $0.562$ $0.331$ $0.451$ $0.087$	$p$ $1.0$ $1.0$ $0.652$ $0.206$ $1.0$ $0.631$ $0.161$ $1.0$ $0.457$ $1.0$ $0.326$ $0.451$ $0.503$ $0.213$	$m$ $0.349$ $0.663$ $0.349$ $0.598$ $0.663$ $0.333$ $0.591$ $0.732$ $0.529$ $0.703$ $0.326$ $0.503$ $0.718$	single phase water, $\Phi = 1.17$	(2.42)

Authors		Correlations				Conditions	Equation
		$\beta$	Re	C1	C2		
Focke, Zachariades and Olivier (1985)	$Nu = C1Re^{C2}Pr^{0.5}$	0°	8000-56000	0.021	0.868	$\beta = 0^\circ; 30^\circ; 45^\circ;$ $60^\circ; 72^\circ; 80^\circ; 90^\circ$ $27 < Re < 56000$	(2.43)
		30°	120-1000	0.77	0.54		
		45°	1000-42000	0.44	0.64		
			45-300	1.67	0.44		
		60°	300-2000	0.405	0.7		
			2000-20000	0.84	0.6		
		72°	20-150	1.89	0.46		
			150-600	0.57	0.7		
		80°	600-16000	1.112	0.6		
		90°	200-4000	1.45	0.58		
27-500	1.05	0.64					
500-2800	1.98	0.54					
300-14000	0.98	0.63					
Chisholm and Wanniarachchi (1992)	$Nu = 0.72Re^{0.59}Pr^{0.4}\Phi^{0.41}((90 - \beta)/30)^{0.66}$					$30^\circ \leq \beta \leq 80^\circ$ $100 < Re < 4000$	(2.44)
Heavner, Kumar and Wanniarachchi (1993)	$\frac{Nu}{Pr^{1/2}} \left(\frac{\mu}{\mu_w}\right)^{-0.17} =$	$\begin{cases} 0.278\Phi^{0.317}Re^{0.683} & \beta = 45^\circ/0^\circ \\ 0.308\Phi^{0.333}Re^{0.667} & \beta = 67^\circ/0^\circ \\ 0.195\Phi^{0.308}Re^{0.692} & \beta = 45^\circ/45^\circ \\ 0.118\Phi^{0.280}Re^{0.720} & \beta = 67^\circ/45^\circ \\ 0.089\Phi^{0.282}Re^{0.718} & \beta = 67^\circ/67^\circ \end{cases}$				$400 < Re < 10000$ $3.3 < Pe < 5.9$	(2.45)
Talik and Swanson (1995)	$Nu = \begin{cases} 0.2Re^{0.75}Pr^{0.4} & 10 < Re < 720; 70 < Pr < 450; \text{água/glicol} \\ 0.248Re^{0.75}Pr^{0.4} & 1450 < Re < 11460; 2.5 < Pr < 5.0; \text{água} \end{cases}$					$\Phi = 1.22$ $Dh = 4.65 \text{ mm}$ $Lw = 0.346 \text{ m}$ $t = 0.61 \text{ mm}$ $\beta = 30^\circ$ $10 < Re < 11460$	(2.46)
Muley and Manglik (1995)	$Nu = \begin{cases} 0.57Re^{0.5}Pr^{1/3}(\mu/\mu_w)^{0.14} & 20 \leq Re \leq 210 \\ 0.1096Re^{0.78}Pr^{1/3}(\mu/\mu_w)^{0.14} & Re \geq 800 \end{cases}$					$\beta = 30^\circ$	(2.47)
Martin (1996)	$Nu_h = \Phi Nu$ $Nu_h = 0.122Pr^{1/3} \left(\frac{\eta_m}{\eta_w}\right)^{1/6} \left(fRe^2 \sin 2\left(\frac{\pi}{2} - \beta\right)\right)^{0.374}$					$\beta$ in radian	(2.48)
Muley and Manglik (1997)	$Nu = \begin{cases} 0.471Re^{0.5}Pr^{1/3}(\mu/\mu_w)^{0.14} & 20 \leq Re \leq 200 \\ 0.10Re^{0.76}Pr^{1/3}(\mu/\mu_w)^{0.14} & Re \geq 1000 \end{cases}$					$\beta = 30^\circ \text{ e } 60^\circ$ $(\beta_{avg} = 45^\circ)$ $2.4 < Pr < 4.5$	(2.49)
Muley, Manglik and Metwally (1999)	$Nu = 1.6774(De/L)^{1/3}(\beta/30)^{0.38}Re^{0.5}Pr^{0.333} \left(\frac{\mu}{\mu_w}\right)^{0.14}$					$30 < Re < 400$ $130 < Pr < 290$	(2.50)
Muley and Manglik (1999)	$Nu = (0.2668 - 6.967 \cdot 10^{-3}\beta + 7.244 \cdot 10^{-5}\beta^2)Re^{[0.728+0.0543\sin(\frac{\pi\beta}{45}+3.7)]}Pr^{0.333} \left(\frac{\mu}{\mu_w}\right)^{0.14}$					$1000 \leq Re$ $2 \leq Pr \leq 6$	(2.51)
Han, Lee and Kim (2003)	$Nu = 0.295(\beta)^{0.09}Re^{0.64}Pr^{0.32}$					$2000 \leq Re$ $2 \leq Pr \leq 6$	(2.52)
Wang and Sunden (2003)	$Nu = 0.205Pr^{1/3} \left(\frac{\mu}{\mu_w}\right)^{1/6} (fRe^2 \sin(180 - 2\beta))^{0.374}$					$10^\circ \leq \beta \leq 80^\circ$	(2.53)
Rao, Sunden and Das (2005)	$Nu = 0.218Re^{0.65}Pr^{1/3} \quad 500 < Re$					$\beta = 30^\circ$ $1000 < Re < 7000$	(2.54)
Hayes, Jokar and Ayab (2009)	$Nu = C1Re^{C2}Pr^{0.333} \left(\frac{\mu}{\mu_w}\right)^{0.14}$	$\beta$	Re	C1	C2	$400 \leq Re \leq 1000$ $15 \leq Pr \leq 50$	(2.55)
Hayes, Jokar and Ayab (2009)	$Nu = C1Re^{C2}Pr^{0.333} \left(\frac{\mu}{\mu_w}\right)^{0.14}$	30°	$400 \leq Re \leq 1000$	0.177	0.744		(2.56)
		46.5°	$400 \leq Re \leq 700$	0.278	0.745		
		63°	$400 \leq Re \leq 700$	0.561	0.726		
Hayes, Jokar and Ayab (2009)	$Nu = C1Re^{C2}Pr^{0.333} \left(\frac{\mu}{\mu_w}\right)^{0.14}$	30°	$2000 \leq Re \leq 8000$	0.134	0.712	$2000 \leq Re \leq 8000$ $2 \leq Pr \leq 6$	(2.56)
		46.5°	$2000 \leq Re \leq 7000$	0.214	0.698		
		63°	$2000 \leq Re \leq 4500$	0.240	0.724		

Authors	Correlations	Conditions	Equation
Khan et al. (2014)	$Nu = \left(0.0161 \frac{\beta}{\beta_{max}} + 0.1298\right) Re^{\left(0.198 \frac{\beta}{\beta_{max}} + 0.6398\right)} Pr^{0.35} \left(\frac{\mu}{\mu_w}\right)^{0.14}$	$500 \leq Re \leq 2500$ $3.5 \leq Pr \leq 6.5$	(2.57)
Akturk et al. (2015)	$Nu = 0.32673 Re^{0.6125} Pr^{1/3} \left(\frac{\mu_b}{\mu_w}\right)^{0.14}$	$\beta = 30^\circ$ $450 \leq Re \leq 5250$	(2.58)
Ikegami, Mutair and Kawabata (2015)	$Nu = 0.37 Re^{0.64} Pr^{1/3}$	$\beta = 65^\circ$ $Re \geq 800$	(2.59)

Source: Author (2019).

As can be seen in Tables 2.1 and 2.2, these equations have different limitations for different values of Chevron angle ( $\beta$ ) and do not take into account all the effects of the different geometric parameters of the corrugation. However, since the geometry of PSHEs and PHEs channels are similar, some correlations presented may provide a prediction with acceptable deviation for some parameters. This topic will be addressed latter on this study, in the results section.

### 2.3.4 Pressure Drop

In practice, pressure loss for all types of fully developed internal flow (laminar or turbulent flow, circular or non-circular pipe, smooth or rough surfaces, horizontal or inclined pipes) can be expressed as (ÇENGEL, 2007):

$$\Delta p = f \frac{L}{D} \frac{\rho u_m^2}{2}, \quad (2.60)$$

where L is the length of the duct. The pressure drop in the heat exchanger plate consists of three contributions: (1) pressure drop associated with the inlet and outlet manifolds and ports, (2) pressure drop within the core (plate channels), and (3) pressure drop due to elevation change for a vertical flow exchanger. In addition to all contributions, the pressure drop on one fluid side in a plate heat exchanger is given by (SHAH; SEKULIC, 2003):

$$\Delta p = \frac{1.5 G_p^2 N_p}{2 g_c \rho_{in}} + \frac{4 f L G^2}{2 g_c D_e} \left(\frac{1}{\rho}\right)_m + \left(\frac{1}{\rho_o} - \frac{1}{\rho_{in}}\right) \frac{G^2}{g_c} \mp \frac{\rho_m g L}{g_c}, \quad (2.62)$$

where  $g_c$  is the proportionality constant in Newton's second law of motion,  $g_c = 1$  and dimensionless in SI units,  $\rho_o$  and  $\rho_{in}$  are fluid mass densities evaluated at the local bulk

temperatures and the mean pressures at the outlet and inlet, respectively, and  $G_p$  is the fluid mass flux in the port (SHAH; SEKULIC, 2003) given by:

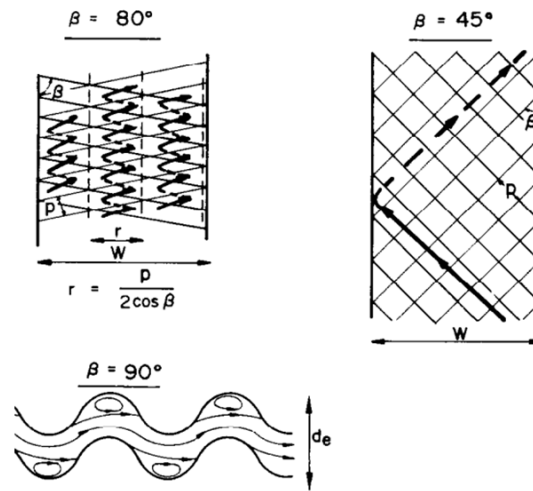
$$G_p = \frac{\dot{m}}{(\pi/4)D_p^2}. \quad (2.63)$$

## 2.4 EXPERIMENTAL AND NUMERICAL RESULTS – LITERATURE

Very few studies related to PSHEs can be found in the current literature. However, a great number of work has been done studying the flow behavior in GPHEs and BPHEs. Experimental investigations are predominant in the literature, nevertheless, analytical and numerical modeling were also performed. Important results from these works are compiled in sequence.

Focke, Zachariades and Olivier (1985) subjected the segment of a GPHE plate to experimentation with the aim of evaluating the influence of the  $\beta$  angle ( $0^\circ$ ,  $30^\circ$ ,  $45^\circ$ ,  $60^\circ$ ,  $72^\circ$ ,  $80^\circ$  and  $90^\circ$  - measured with respect to the vertical axis as shown in Figure 2.5 on the thermo-hydraulic performance of the heat exchanger. A summary of the main results is shown in Figure 2.5. When  $\beta = 45^\circ$  the fluid flows predominantly in the grooves and, upon reaching the edge of the plate, is "reflected" and returns to the opposite side of the plate along the grooves. This pattern renders the heat transfer rate approximately uniform throughout the width of the plate. For  $\beta = 80^\circ$  the fluid still flows mainly along the grooves, but the "reflection" occurs between the contact points of the plate, forming a zig-zag pattern in the flow. In the this latter case, the transition to a turbulent flow occurs sooner, in relation to the other  $\beta$  angles analyzed, thus, the highest rate of heat transfer is observed. However, there are increases in pressure drop in the order of magnitude of more than 2.5 while the heat transfer increases only 4 to 10 times.

Figure 2.5 – Influence of the Chevron angle on the flow pattern for a GPHE.

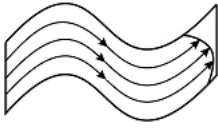
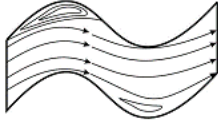
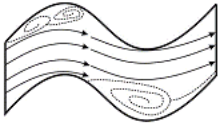
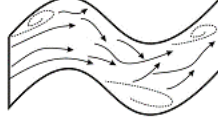


Source: Adapted from Focke, Zachariades and Olivier (1985).

With  $\beta = 90^\circ$  the two overlapping plates create a corrugated channel, where the distinction between grooves and contact points is no longer applicable, as there is no more cross flow, we can observe the separation of the flow. The separation zones cause the heat transfer, pressure drop and the friction factor to decrease considerably closer to the values found for  $\beta = 60^\circ$  (FOCKE; ZACHARIADES; OLIVIER, 1985).

Corrugated channels ( $\beta = 90^\circ$ ) are investigated by Greth (1999) in order to provide a better understanding of the local behavior of waves and their contribution to heat transfer and pressure drop. The variation of  $Re$  promotes the modification of the flow pattern within the channels as shown in Figure 2.6.

Figure 2.6 – Flow patterns in a single corrugated channel as a function of Reynolds ( $\beta = 90^\circ$ ).

Re	Flow visual description	Flow characteristics
<100		- Uniform laminar flow. No recirculation zone detected.
100 - 200		Flow divided in 2 zones: - Principal laminar flow in the stream center; - Stable recirculation zones in the bends with separation and reattachment points.
200 - 350		Flow divided in 2 zones: - Principal laminar flow in the stream center; - Unstable secondary motions in the bends: separation and Von Karman vortices are detected.
200 - 2000		Unstable turbulent flow: great vortices disrupt principal flow in some zones of the fluid stream, but they are neutralized by still flow in other zones of the fluid stream.
>2000		Turbulent flow divided in 2 zones (with unstable interface between): - Principal turbulent flow in the stream centre; - Zones with low relative velocity and potentially recirculation.

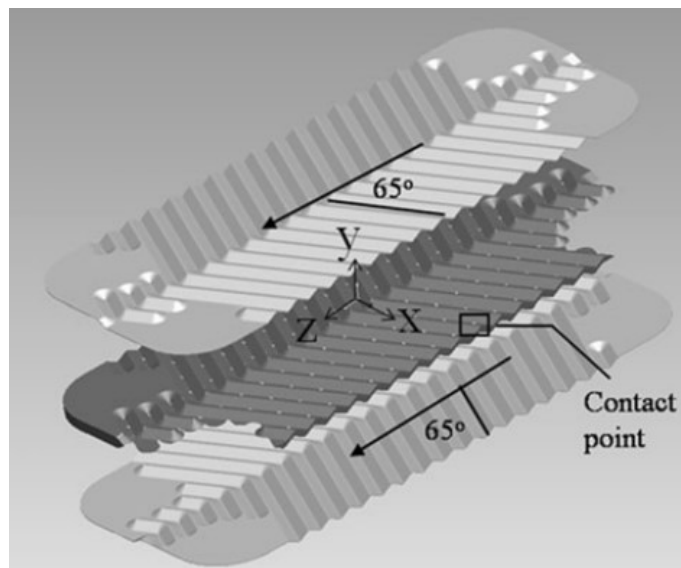
Source: Adapted from Greth (1999) apud Vitillo (2014, p.45).

For a very low Re (200) it is already possible to observe characteristics of a turbulent flow with the development of stable recirculation zones. The greatest heat transfer region is located opposite to the recirculation zones, where the flow acceleration is higher, i.e., recirculation is desired to achieve higher performance (METWALLY and MEANGLI, 2004 apud VITILLO, 2014, p 50). However, it is important to emphasize that the corrugated channels for  $\beta = 90^\circ$  are two-dimensional and the plates of the heat exchangers for others values of  $\beta$  have a third dimension that will contribute to the separation and fixation of the boundary layer, a process that will increase the local and global heat transfer of the equipment (VITILLO, 2014).

For the corrugated plate of a PHE, the increase of the Chevron angle maintaining Re constant, favors the formation of the turbulent flow. The turbulent flow raises the coefficient of friction and consequently increases the pressure drop in the channels. In other words, there are counterpoints for the increase of the heat transfer rate when the  $\beta$  value is added (MARTIN, 1996), (SHIOMI; NAKANISHI; UEHARA, 2004) and (HUANG, 2010).

Liu and Tsai (2010) also encountered the zig-zag flow pattern when investigating the behavior of a single flow path, consisting of two plates ( $\beta = 65^\circ$ ) including the fluid inlet and outlet ports of a GPHE (Figure 2.7). The experimental data were corroborated with those obtained by 3D-CFD simulations performed in the commercial software ANSYS FLUENT. The authors observed that the transition from laminar to turbulent flow occurred at a Re equal to 300, where the turbulent flow was modeled with the Realizable  $k - \varepsilon$  model with Non-equilibrium wall functions. For the Re range from 660 to 2000 a deviation of 7% for the friction factor was observed when compared to experimental data.

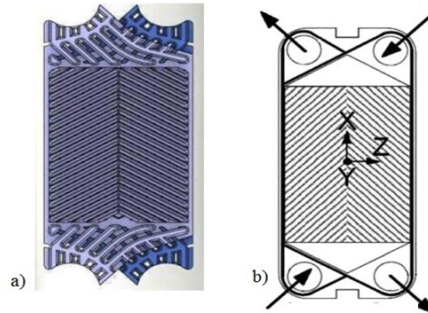
Figure 2.7 – Cross corrugated channel formed by two plates with opposite directions for a GPHE with  $\beta = 65^\circ$ .



Source: Liu and Tsai (2010).

Gherasim, Galanis and Nguyen (2011) investigate the behavior of thermal and hydrodynamic fields between two confined fluid passages between a set of three plates ( $\beta = 30^\circ$ ) of a GPHE (Figure 2.8). The validation of the 3D-CFD analyzes, generated for laminar and turbulent flows using the ANSYS FLUENT software was performed with experimental data obtained by Gherasim et al. (2011). The laminar model was satisfactory for Reynolds numbers inferior to 400. For the turbulent regime, five combinations of turbulent models of two equations and wall treatments were compared, and the Realizable  $k - \varepsilon$  model with Non-equilibrium wall functions showed better results.

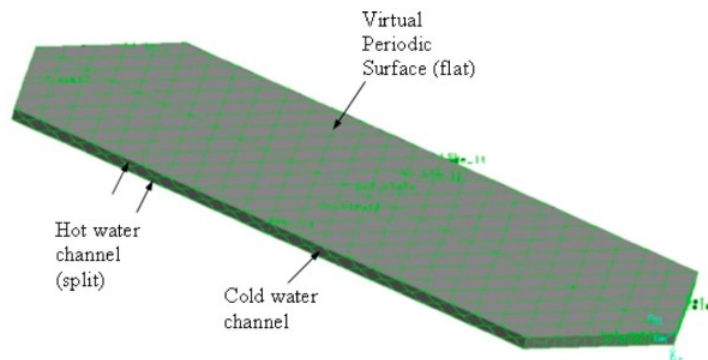
Figure 2.8 – Plates of a GPHE: a) Full geometric domain (2 channels); b) Coordinate systems and fluid inlet and outlet positions.



Source: Adapted from Gherasim, Galanis and Nguyen (2011).

Jain, Joshi and Bansal (2007) carried out a study on a computational domain consisting of a cold channel and two hot channels delimited by a plate on both sides of the cold channel, representing the section of a plate of a small PHE with  $\beta$  equal at  $60^\circ$  (Figure 2.9). The approach adopted for the treatment of wall and turbulence model was the same one used by Liu and Tsai (2010). It was found that the numerical friction factor had a deviation below 2.5% to 14.5% in relation to the Kumar (1984) correlation (shown in Table 2.1), whereas the values of the experimental friction factor showed deviations greater than 8% to 33% with respect to the correlation. The exclusion of the distribution areas from the entrance and exit ports of the plates was the reason given for the imprecision of the results.

Figure 2.9 – Geometric domain and its limits.

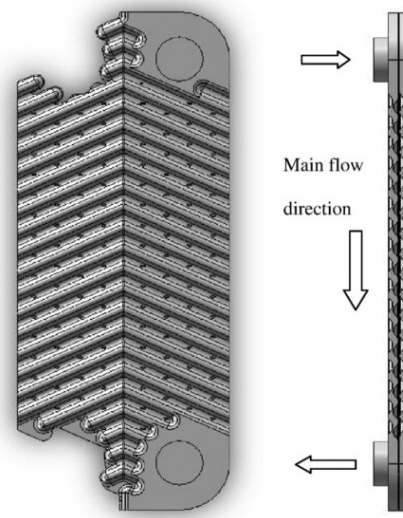


Source: Adapted from Jain, Joshi and Bansal (2007).

Tsai, Liu and Shen (2009) conducted experimental and numerical investigations in four plates of a BPHE ( $\beta = 65^\circ$ ) (Figure 2.10). The software and the turbulent model for the study of the Re range from 600 to 1700 were the same as those applied by the authors cited

above. The experimental results were 20% higher for the pressure drop compared to the ones predicted by the numerical model. The authors suspected that this deviation was caused by the small computational domain chosen when compared to the experimental setup, since the experimental results were documented for 400 plates and the numerical model was comprised of only two passages between four plates.

Figure 2.10 – Computational domain composed of four corrugated plates.

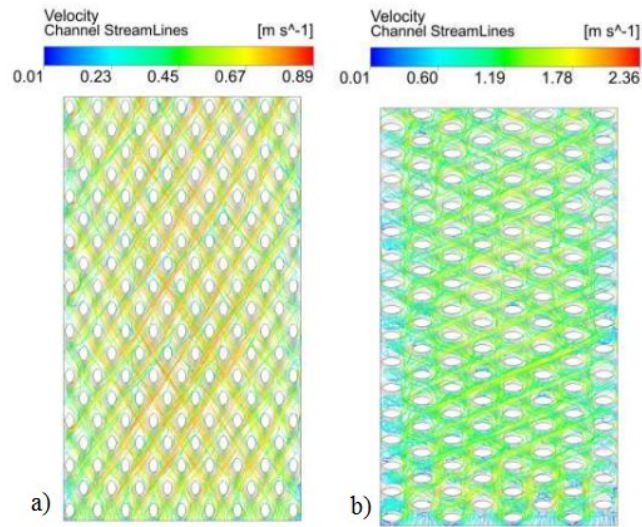


Source: Adapted from Tsai, Liu and Shen (2009).

We find in the literature some authors who defend and emphasize the importance of the analysis of small sections of the flow. As a main argument, they emphasize that a small segment of the plate of a heat exchanger offers information about the local flow patterns and the interference of the geometric parameters of each model.

Gullapalli (2013) investigates methods to estimate the performance of BPHEs operating in several applications. In addition to conducting experiments the study presents numerical simulations in sections of the plate for different  $\beta$  ( $32^\circ$ ,  $66.5^\circ$  and  $67^\circ$ ) (Figure 2.11), and in the complete plate ( $\beta = 65^\circ$ ) with the aid of the ANSYS CFX software. For both cases, the Shear Stress Transport (SST) method was applied to model the turbulent flow. The study also analyzed three wall contour conditions for the heat transfer: constant wall temperature; conjugated heat transfer; and constant heat flow. It was shown that the predictions of all these methods underestimated the thermal performance of the heat exchanger.

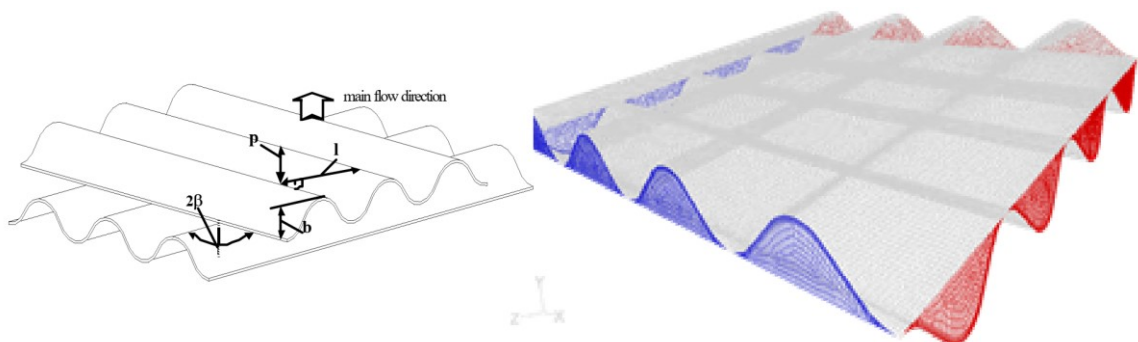
Figure 2.11 – Flow patterns for simulated plate sections ( $Re = 2000$ ): a)  $\beta = 32^\circ$  and b)  $\beta=67^\circ$ .



Source: Gullapalli (2013).

Dovic and Svaic (2004) performed numerical simulations on 16 channel units from a plate of a PHE (Figure 2.12). The authors observed zig-zag flow patterns by analyzing the flow path in the channels for  $\beta = 28^\circ$  and  $65^\circ$ . The comparison with experimental results for thermal and hydraulic tests indicated that the pressure drop and the heat transfer calculations provided reliable results only for the transient and fully turbulent flows ( $Re > 700$ ), in which the RES model proved to be more accurate than the  $k - \epsilon$  model.

Figure 2.12 – Geometry of the channels composed of two corrugated plates constituting the 16 cells units of a PHE.

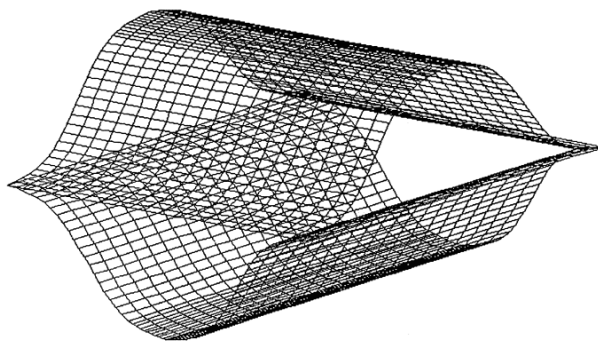


Source: Adapted from Dovic and Svaic (2004).

Mehrabian and Poulter (1998) modeled with the software ANSYS CFX a single plate cell of a GPHE (Figure 2.13). A periodicity condition was applied to reduce the complexity of the geometry of the modeled channel, allowing analysis of the flow in the smallest segment of the channel. For the  $\beta$  angles of  $35^\circ$ ,  $45^\circ$  and  $55^\circ$ , the authors studied the distribution of the

flow, pressure and temperature in the channel segment. Some results of the numerical analysis were compared with those obtained by empirical formulations for the heat exchanger plates. In conclusion, it was observed that  $\beta$  and the general direction of the flow are parameters that influence the thermal-hydraulic performance of the plate heat exchangers. The change in  $\beta$  affects the basic structure of the flow, which in turn, is the factor that acts directly on the pressure and heat transfer rate.

Figure 2.13 – Single cell extracted from corrugated plate of a GPHE.

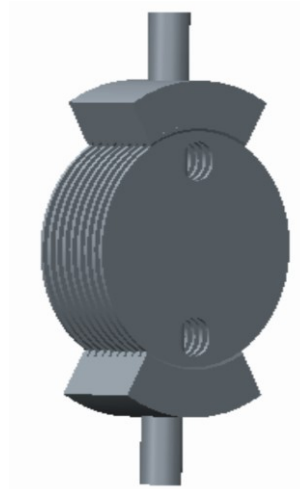


Source: Mehrabian and Poulter (1998).

As the literature shows, the geometry of corrugated plates of GPHE and BPHE are widely studied. However, studies and data related to the circular geometry of the corrugated plates of PSHEs are scarce and recent.

Liu et al. (2015) presented a numerical study to analyze the shell inlet port of a PSHE to analyze the fluid flow distribution inside the heat exchanger. The analyzed geometry consists of six plates with 257 mm of diameter, 11 channels and a semi-circular head mounted at the inlet of the flow (Figure 2.14). The RNG  $k - \epsilon$  was used as the turbulence model to analyze the Re range from 715 to 4092. They concluded that the semi-circular head was effective in improving the performance of the heat exchanger, increasing the uniformity of the fluid flow distribution on the shell side of the PSHE, decreasing the total pressure drop on that side of the heat exchanger.

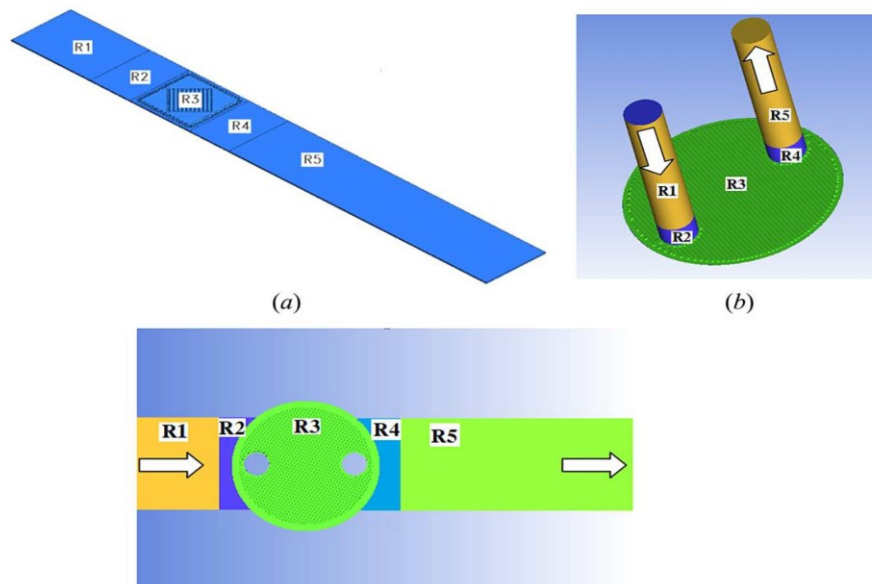
Figure 2.14 – Shell inlet geometry model for a PSHE.



Source: Liu et al. (2015).

More recently Luan et al. (2017) performed a numerical and experimental study on two types of heat exchangers. The computational domain consists of a unitary cell of a PHE (block-type) with  $\beta = 45^\circ$  and a corrugated channel of a PSHE with  $\beta = 75^\circ$  with a diameter of 440 mm (Figure 2.15).

Figure 2.15 – Computational domain: (a) block-type; (b) PSHE-type plate-side; (c) PSHE-type shell-side.



Source: Luan et al. (2017).

The PSHE corrugated channel was evaluated both on the plate-side and on the shell side. The software ANSYS FLUENT with the Realizable  $k - \epsilon$  model was adopted and the

near-wall treatment with the Enhanced wall function was applied to the turbulence modeling. Re numbers from 300 to 10000 were analyzed. A clearance (space between plates in the numerical model) of 0.2 mm was proposed to improve mesh quality around the points of contact. For the simulations of plate-side of the PSHE, the deviation between CFD and experimental correlations for the Colburn heat transfer factor was within  $\pm 15\%$  in the Re range from 300 to 7000.

In summary the table below compiles the main results obtained by the authors mentioned in the review.

Table 2.3 – Main results observed in the literature review.

Authors	Heat Exchanger	Analysis	Re	$\beta$	Main Results
Focke et al. (1985)	GPHE	Experimental	$20 < Re < 5.6 \times 10^4$	$0^\circ, 30^\circ, 45^\circ, 60^\circ, 72^\circ, 80^\circ$ e $90^\circ$	Zigzag flow patterns ( $\beta = 80^\circ$ ); Lower heat transfer and pressure drop ( $\beta = 90^\circ$ e $60^\circ$ ).
Greth (1999)	-	Experimental	Re < 100 Re > 20000	$90^\circ$	Turbulent flow for Re < 200; Greater heat transfer in the recirculation zones.
Liu et al. (2010)	GPHE	Experimental Numerical	$660 < Re < 2000$	$65^\circ$	Zigzag flow patterns ( $\beta = 80^\circ$ ); Turbulent flow for Re = 300.
Gherasim et al. (2011b)	GPHE	Numerical	$120 < Re < 2800$	$30^\circ$	Laminar flow for Re < 400.
Jain et al. (2007)	PHE	Numerical	$400 < Re < 1300$	$60^\circ$	Frictional factor presents smaller deviation in relation to the correlation of Kumar; Computational domain may generate inaccuracies in results.
Tsai et al. (2009)	BPHE	Numerical	$400 < Re < 1300$	$65^\circ$	The numerical error is 20% bigger than the experimental one. Unimpressive computational domain.
Gullapalli (2013)	BPHE	Numerical	$300 < Re < 3000$	$32^\circ, 65^\circ, 66,5^\circ$ e $67^\circ$	Numerical error ranging from 2 to 20% using constant heat flow in relation to the experimental results.
Dovic et al. (2004)	PHE	Numerical	$10 < Re < 1 \times 10^4$	$28^\circ$ e $65^\circ$	Zigzag flow patterns ( $\beta = 28^\circ$ e $65^\circ$ ); Turbulent flow for Re > 700.
Mehrabian et al. (1998)	GPHE	Experimental Numerical	-	$35^\circ, 45^\circ$ e $55^\circ$	The change of $\beta$ affects the basic structure of the flow; $\beta$ directly influences the pressure and heat transfer rate.
Liu et al. (2015)	PSHE	Numerical	$715 < Re < 4092$	-	A change in the design of the shell-side of plate inlet of the PSHE improves the uniformity of flow distribution and decreases the pressure drop.
Luan et al. (2017)	PHE/PSHE	Experimental Numerical	$300 < Re < 10000$	$45^\circ/75^\circ$	An adequate clearance (c) between the corrugated plates improves the mesh around the contact points, contributing to the numerical analysis (c/Dh = 0.02).

Source: Author (2019).

Even more, as can be seen by tables 2.1 and 2.2 presented earlier on the text, it is evident that many experimental studies proposing correlations for Nusselt and friction factor for PHEs were published, addressing a large range of Reynolds number and Chevron angles for this type of exchanger. However due to the change in the geometry of the plates, from rectangular to circular, a change in the behavior of some properties of the flow for the PSHE

is expected as a variation of the friction factor along the plate (due to change of flow section). These details are still poorly explored for PSHEs.

Another point that has been not been given much attention until now are the influences of the geometric simplifications in the numerical models in order to reduce the computational demand for the resolution of the fluid flow hydrodynamics between plates of a PSHE. In the same sense, the analysis of flows with higher Re was also little explored. In Table 2.3 only 3 studies with  $Re > 5000$  are identified, and only one of the numerical studies is classified in this Re range (notice also that in table 2.1, most of the correlations presented for Fanning factor in PHEs are for  $Re < 5000$ ).

This work is inserted in this context and brings contributions in these three main areas.

### 3 METHODOLOGY

This chapter presents the details of the numerical modeling based on the finite volumes methodology applied with the commercial software ANSYS CFX. The evaluated computational domains and their applied models defined in the following sections. The validation of the described models was performed with experimental data obtained in an experimental rig design for measurement of total pressure loss for a pair of PSHE plates. The experimental setup is also described in this section.

#### 3.1 PLATE VALIDATION

##### 3.1.1 PSHE Corrugated Plate

The validation of the hydrodynamic model was performed based on the total pressure loss for a pair of PSHE plates for a Reynolds number range in an experimental bench. Configurations of Chevron angle of  $15^\circ \times 15^\circ$ ,  $45^\circ \times 45^\circ$  and  $45^\circ \times 15^\circ$  were tested. Also, the same test rig was applied by Beckedorff et al. (2019) to study the flow pattern between two PSHE plates with Chevron angle of  $15^\circ \times 15^\circ$  for a Re number of 3450. This flow pattern is later also compared to the numerical results in Chapter 4 to verify the hydrodynamics of the flow.

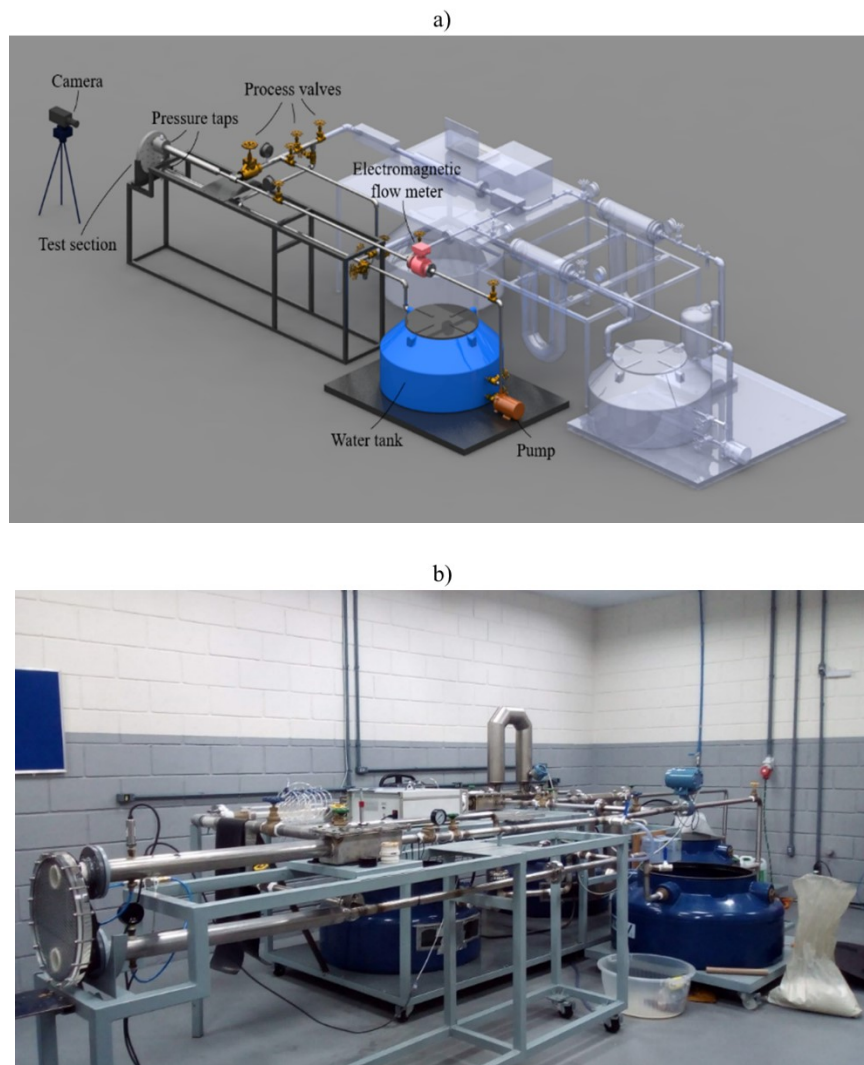
##### 3.1.1.1 Experimental setup

###### 3.1.1.1.1 Test rig

PSHE channel flows have been created in a water loop driven by a centrifugal pump. The in-line 2 kW pump, type BC-91 S/T from Schneider Motobombas, allows for a maximum mass flow rate of 2.5 kg/s. A frequency controller and process valves permit fine-tuning of the Reynolds number by adjusting the mass flow rate of the vertical flow in the measurement section. Water flows through the test section after 40 pipe diameters and after passing, subsequently, a mesh flow conditioner. The mass flow rate is measured by means of a Rosemount 8700 M magnetic flowmeter, whose inaccuracy is less than 0.5% of the registered

flow rate. A water reservoir contains about 0.35 m<sup>3</sup> of water. This value facilitates water temperature stabilization and hence Reynolds number control. Thermocouples monitor water temperature in the flow loop (BECKEDORFF et al., 2019). Figure 3.1 presents details of the setup.

Figure 3.1 – Multiphase flow experimental setup: (a) schematics and (b) photograph. Only the water circuit (colorful graphic in “a”) was applied for experiments.



Source: Adapted from Beckedorff et al. (2019).

The measurement section consists of two narrow acrylic plates. They were machined to match the PSHE channel geometry when they are pressed against each other. Water leaves or enters the section through pipes with 56 mm inner diameter. Pressure taps were installed

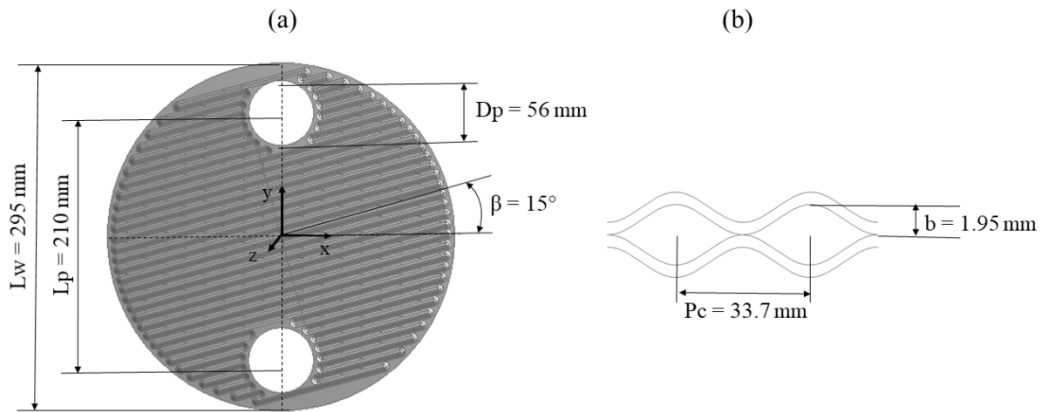
just upstream and downstream of the test section. An Omega differential pressure transducer, type PX409 Series Differential Pressure, monitors the pressure drop over the test section. The transducer uncertainty is 0.5% of the registered pressure drop. Pressure drop measurements also occurred in a smooth titanium PSHE channel to assure that the flow field measured in the acrylic cross section was representative. The commercial PTV (Particle Tracking Velocimetry) imaging code from La Vision GmbH, named Davis, has been used to obtain tracer trajectories. The PTV measurements have provided inner flow features within PSHE (BECKEDORFF et al. 2019). The PVT measurements have been performed only for the inlet mass flow of 0.49 kg/s and Chevron angle of  $15^\circ \times 15^\circ$ . No PVT measurements were performed for Chevron angle of  $45^\circ \times 45^\circ$  and  $45^\circ \times 15^\circ$ .

#### *3.1.1.1.2 Test section*

Two circular acrylic disks with a thickness of 1.5 cm were machined to make up a typical PSHE channel when pressed together. A metal apparatus was used to prevent the distancing of the plates for high Re. Figure 3.2 (a) presents the main dimensions of the channel frontal view of one plate. The port diameter,  $D_p$ , is 56 mm, the external diameter,  $L_w$ , is 295 mm, whereas the length between the inlet and outlet centers,  $L_p$ , is 210 mm. A Cartesian coordinate system with its origin in the frontal view center is taken with the y-axis joining the centers and with gravity antiparallel to the y-axis. The Chevron angle,  $\beta$ , denotes the angle between the flow channel main direction and the x-axis;  $\beta$  is chosen as  $15^\circ$ , which is typical of high pressure drop channels. Figure 3.2 (b) provides details of the cross-section, where  $P_c$  is the corrugation pitch and  $b$  the corrugation amplitude. Here,  $P_c$  is 33.7 mm and  $b$  is 1.95 mm (BECKEDORFF et al., 2019).

For more information and details about the experimental study developed for the PSHE channel see Beckedorff et al. (2019).

Figure 3.2 – PSHE channel flow geometry: (a) frontal view main dimensions for one disk, (b) cross section characteristics.



Source: Author (2019).

### 3.1.1.2 Numerical setup

The three-dimensional computational domain constructed to model the PSHE cross corrugated channel consists of the fluid domain delimited by two corrugated plates, this later shown in Figure 3.2. Four models were used for the numerical hydrodynamic analysis of the PSHE corrugated channel: two considering  $\beta = 15^\circ \times 15^\circ$ ; one for  $45^\circ \times 45^\circ$  and one more for  $15^\circ \times 45^\circ$ , (see Figure 3.3). Each configuration is here denominated of “Case”.

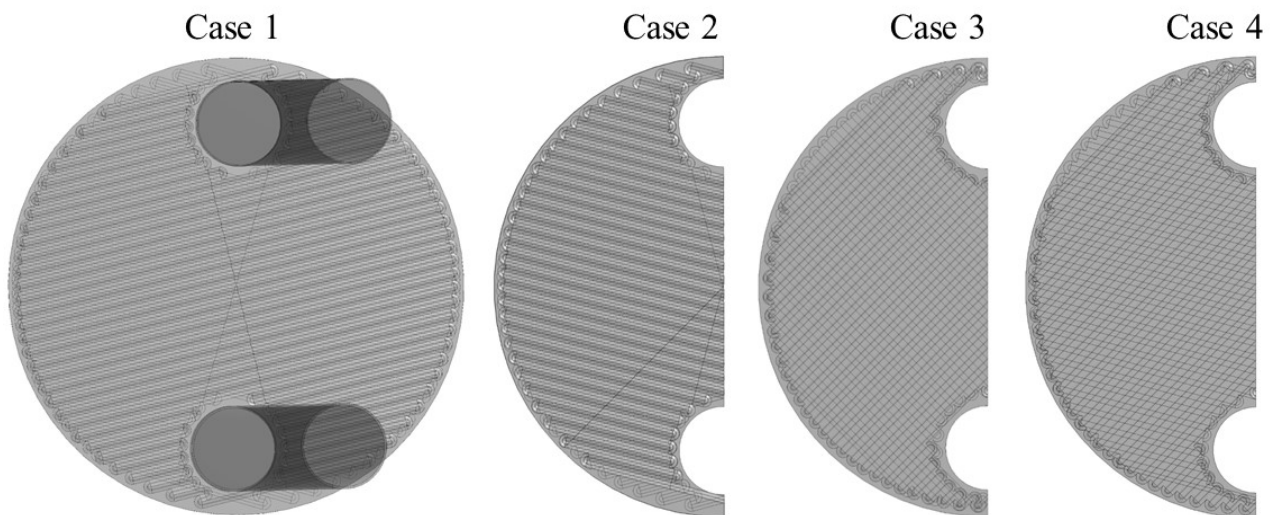
**Case 1:** fluid domain formed by the space between two corrugated plates forming a channel with  $\beta = 15^\circ$  and with 0.168 m long tubes connected to the inlet and outlet ports. The tubes were coupled to the plates to better agree with the experimental bench that measures the pressure for the experimental test at the tube surface at a position located at 0.168 m from the inlet and outlet port.

**Case 2:** The computational domain presented in Case 1 was segmented along the vertical axis and the tubes were excluded. A symmetry condition was adopted at the sectioned interface. Representing one half of the corrugated plate, the symmetrical plate has half the section area of the intake and discharge ports.

**Case 3:** fluid domain formed by the space between two corrugated plates segmented along the vertical axis forming a symmetrical channel with  $\beta = 45^\circ$ . The applied symmetry condition and section area of the inlet and outlet ports are equivalent to those in Case 2.

**Case 4:** fluid domain formed by the space between two corrugated plates segmented along the vertical axis forming a symmetrical channel with  $\beta = 45^\circ \times 15^\circ$ . The applied symmetry condition and section area of the inlet and outlet ports are equivalent to those in Case 2.

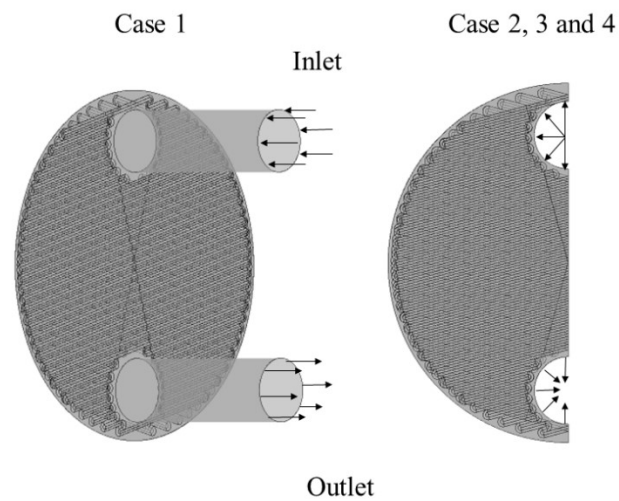
Figure 3.3 – Computational domain: Case 1: corrugated plate with tubes coupled to the inlet and outlet ports for  $\beta = 15^\circ \times 15^\circ$ ; Case 2: one half of the corrugated plate for  $\beta = 15^\circ \times 15^\circ$ ; Case 3: one half of the corrugated plate for  $\beta = 45^\circ \times 45^\circ$ ; Case 4: one half of the corrugated plate for  $\beta = 45^\circ \times 15^\circ$ .



Source: Author (2019).

Figure 3.4 shows the location of the flow inlet and outlet sections employed for the evaluated cases.

Figure 3.4 – Flow inlet and outlet sections for the evaluated cases. Inlet: upper ports. Outlet: lower ports.



Source: Author (2019).

The Reynolds number range evaluated is  $1332 \leq Re \leq 4034$  for Cases 1 and 2,  $1993 \leq Re \leq 7529$  for Case 3 and  $1305 \leq Re \leq 6153$  for Case 4.

#### 3.1.1.2.1 Boundary conditions and models

For all evaluated four cases, the inlet condition at the inlet port was specified as the mass flow rate in the inlet port section of the plate, the mass flow direction was considered normal to the inlet surface, assuming that the flow is evenly distributed in the inlet region. The percentage of turbulence intensity was prescribed as 5%, an intermediate value considered as an appropriate configuration for complex flows (JAIN; JOSHI; BANSAL, 2007). On the outlet port, the relative pressure condition was described as a constant value of zero (the reference pressure was set to 1 atm). All other variables at the outlet were set to zero gradient. The convergence criterion adopted was maximum error of  $1 \times 10^{-5}$  for all variables. The plate surfaces were considered with roughness equal to zero and with the no-slip condition. Water at 25°C was used as the working fluid. All fluid properties and boundary conditions employed for all analyzed cases are shown in Table 3.1. The Hybrid Scheme was adopted for the advection terms and all cases were solved through the commercial software ANSYS CFX. ANSYS CFX applies a coupled solver and a pseudo-transient scheme to solve

the discretized set of equations. Details of the mass flow values for each evaluated numerical test presented in the results section case can be found in Appendix A.

Two turbulence models were applied: the Shear Stress Transport Model – SST; and the Standard  $k - \epsilon$  model.

Table 3.1 – Fluid properties and boundary conditions.

Fluid Properties	
Fluid	Water
Fluid Temperature [°C]	25
Density [kg.m <sup>-3</sup> ]	997
Dynamic Viscosity [kg.m <sup>-1</sup> .s <sup>-1</sup> ]	8.90E-04
Inlet	
Mass and Momentum	Mass Flow Rate
Flow Direction	Normal to Boundary Condition
Turbulence	Medium Intensity (5%)
Outlet	
Mass and Momentum	Average Static Pressure
Relative Pressure [Pa]	0
Pressure Profile Blend	0.05
Pressure Averaging	Average Over Whole Outlet
Wall	
Mass and Momentum	No Slip Wall
Wall Roughness	Smooth Wall

Source: Author (2019).

## 3.2 NUMERICAL MODELS

### 3.2.1 Governing Equations

A statistical approximation to treat turbulence was proposed by Reynolds in 1895, where an instant property  $\phi$  is expressed by the sum of a mean part  $\bar{\phi}$  and its fluctuation  $\phi'$  (WILCOX, 1994):

$$\phi = \bar{\phi} + \phi'. \quad (3.1)$$

The set of Navier-Stokes and mass continuity governing equations with application of the Reynolds averaged method for a fluid considered as Newtonian, incompressible, and with constant viscosity are presented by

$$\frac{\partial}{\partial x_i} (\bar{u}_i) = 0, \quad (3.2)$$

$$\frac{\partial}{\partial t} (\rho \bar{u}_i) + \frac{\partial u_i}{\partial x_j} (\rho \bar{u}_i \bar{u}_j) = -\frac{\partial \bar{p}}{\partial x_i} + \frac{\partial}{\partial x_j} (2\mu \bar{S}_{ji} - \bar{\tau}_{ij}) + B_i, \quad (3.3)$$

where  $\bar{p}$  is the average static pressure, the averaged velocity component is given by  $\bar{u}$ ,  $B_i$  is the body force per unit volume acting on the fluid and  $t$  is the time. The term  $\bar{S}_{ji}$  is the mean strain-rate tensor and  $\bar{\tau}_{ij}$  is known as the Reynolds stress tensor, these last two defined as:

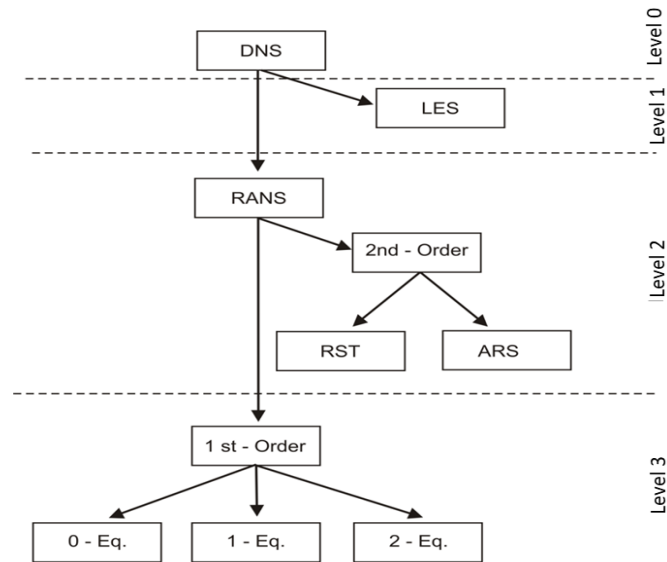
$$\bar{S}_{ji} = \frac{1}{2} \left( \frac{\partial \bar{u}_i}{\partial x_j} + \frac{\partial \bar{u}_j}{\partial x_i} \right), \quad (3.4)$$

$$\bar{\tau}_{ij} = -\rho \overline{u'_i v'_j}. \quad (3.5)$$

Equation (3.5) mathematically represents the effects of fluctuations on the mean fluid flow. Physically, these terms correspond to a rate of transfer of momentum arising from the fluctuation of the velocity of the fluid.

The turbulence is treated by means of approximations by different turbulence models. Currently, turbulence models are divided into four levels of resolution, as represented in Figure 3.5.

Figure 3.5 – Hierarchy of current models of turbulence. Abbreviations: DNS = Direct Numerical Simulation; LES = Large Eddy Simulation; RANS = Reynolds-Averaged Navier Stokes; 1st order = closure of first order turbulence; 2nd order = closure of second order turbulence; RST = Reynolds-Stress Tensor transport models; ARS = Algebraic Models of Reynolds-Stress; 0-, 1-, 2-Eq = Zero, one and two equation models.



Source: Adapted from Blazek (2001).

The level of precision in the resolution of the turbulence decreases as the level grows, i.e. the models indicated by level 3 are the most simplified and those indicated by level 0 are the most complete. At level 3 the first-order models, represented by the algebraic model (0 equations) and the model of one or two equations appear. The models classified at this level are based on the Boussinesq turbulent viscosity hypothesis. They are solved from the Reynolds averages concept, using the mean Reynolds equations applied to Navier-Stokes (RANS - Reynolds Averaged Navier Stokes). Two turbulence models were used in this study, both of them from first order and of two equations. They are described below.

### 3.2.2 The Standard $k - \varepsilon$ Model

The  $k - \varepsilon$  model is the most popular and extensively used method among the two equation turbulence models. Different versions of this model are found in the literature. This model is sometimes referred to as the Standard  $k - \varepsilon$  model, which is the classic model (WILCOX, 1994).

Originally the  $k - \varepsilon$  model was developed to improve the mixing length model and to avoid the algebraic prescription of the turbulent length scale in complex flows. The transport equations are solved by two scalar turbulence properties. The equation for  $k$  is a model of the transport equation for the turbulent kinetic energy, and the equation for  $\varepsilon$  is a model for the rate of turbulent kinetic energy dissipation (BARDINA; HUANG; COAKLEY, 1997).

For wall limited flows, the model shows good agreement with the experimental results for zero or small mean pressure gradients, but is less accurate for adverse pressure gradients. The model requires explicit functions of wall damping (BARDINA; HUANG; COAKLEY, 1997).

The Reynolds tensor are modeled in terms of the turbulence viscosity as follows:

$$\tau_{tij} = 2\mu_t(S_{ij} - S_{nn}\delta_{ij}/3) - 2\rho k\delta_{ij}/3, \quad (3.6)$$

where  $S_{ij}$  is the strain rate tensor of the mean velocity,  $k$  is the turbulent kinetic energy and  $\mu_t$  is the turbulent viscosity defined as:

$$\mu_t = C_\mu f_\mu \bar{\rho} k^2 / \varepsilon, \quad (3.7)$$

where  $\varepsilon$  is the turbulence dissipation rate,  $C_\mu$  is an empirical constant of the model, determined in the equilibrium analysis for high numbers of  $Re$ , and the damping function,  $f_\mu$ , is equal to 1 for the classical  $k - \varepsilon$  model.

The equations of transport for the turbulence and dissipation of the energy in the  $k - \varepsilon$  model are solved according to equations (3.9) and (3.10):

$$\frac{\partial(\bar{\rho}k)}{\partial t} + \frac{\partial(\bar{\rho}u_j k)}{\partial x_j} = \frac{\partial}{\partial x_j} \left[ \left( \mu + \frac{\mu_t}{\sigma_k} \right) \frac{\partial k}{\partial x_j} \right] + P_k - \bar{\rho}\varepsilon, \quad (3.8)$$

$$\frac{\partial(\bar{\rho}\varepsilon)}{\partial t} + \frac{\partial(\bar{\rho}u_j \varepsilon)}{\partial x_j} = \frac{\partial}{\partial x_j} \left[ \left( \mu + \frac{\mu_t}{\sigma_\varepsilon} \right) \frac{\partial \varepsilon}{\partial x_j} \right] + C_{\varepsilon 1} P_k \frac{\varepsilon}{k} - C_{\varepsilon 2} \bar{\rho} \frac{\varepsilon^2}{k}, \quad (3.9)$$

where four empirical constants are presented:  $\sigma_k$ ,  $\sigma_\varepsilon$ ,  $C_{\varepsilon 1}$  and  $C_{\varepsilon 2}$ . Their values corresponding to the  $k - \varepsilon$  model are found in (BARDINA; HUANG; COAKLEY, 1997). The rate of production of turbulent energy due to the viscous energy,  $P_k$ , is defined by:

$$P_k = \mu_t \left( \frac{\partial \bar{u}_m}{\partial x_j} + \frac{\partial \bar{u}_j}{\partial x_m} \right) \left( \frac{\partial \bar{u}_m}{\partial x_j} \right). \quad (3.10)$$

### 3.2.3 The SST Model (Shear – Stress – Transport)

The SST model is a combination of the  $k - \varepsilon$  and  $k - \omega$  models to obtain a formulation with adverse pressure gradient flow applications close to walls. For this, a mixing function ( $F_1$ ) is introduced and this function is then equal to 1 near the solid surface and equal to 0 for the flow domain away from the wall. Thus, the  $k - \omega$  model is applied for the region adjacent to the wall and the  $k - \varepsilon$  model is applied for the remainder of the flow. This approach makes it possible to use the attractive performance near the wall of the  $k - \omega$  model without the possible errors resulting from the free flow, common of this method. In addition, the SST model also presents a modification of the turbulent viscosity definition, which can be interpreted as  $C_\mu$ , where  $C_\mu$  in the  $k - \varepsilon$  model is a constant. This modification is necessary to accurately capture the onset of separation under pressure gradients. The equations modeled for the turbulent kinetic energy  $k$  and the turbulence frequency  $\omega$  are as follows (MENTER; ESCH; KONNO, 2003):

$$\frac{\partial \rho k}{\partial t} + \frac{\partial \rho U_j k}{\partial x_j} = \tilde{P}_k - \beta^* \rho \omega k + \frac{\partial}{\partial x_j} \left( \Gamma_k \frac{\partial k}{\partial x_j} \right), \quad (3.11)$$

$$\frac{\partial \rho \omega}{\partial t} + \frac{\partial \rho U_j \omega}{\partial x_j} = \frac{\alpha}{\nu_t} P_k - \beta \rho \omega^2 + \frac{\partial}{\partial x_j} \left( \Gamma_\omega \frac{\partial \omega}{\partial x_j} \right) + (1 - F_1) 2 \rho \sigma_{\omega 2} \frac{1}{\omega}. \quad (3.12)$$

where the blending function  $F_1$  is calculated as:

$$F_1 = \tanh(\arg_1^4), \quad (3.13)$$

$$\arg_1 = \min \left( \max \left( \frac{\sqrt{k}}{\beta^* \omega y}; \frac{500 \nu}{y^2 \omega} \right); \frac{4 \rho \sigma_{\omega 2} k}{CD_{k\omega} y^2} \right), \quad (3.14)$$

where  $y$  is the distance to the wall and  $CD_{k\omega}$  is the positive portion of the cross-diffusion term:

$$CD_{k\omega} = \max \left( 2 \rho \sigma_{\omega 2} \frac{1}{\omega} \frac{\partial k}{\partial x_j} \frac{\partial \omega}{\partial x_j}; 1.0 e^{-10} \right). \quad (3.15)$$

The turbulent viscosity is calculated by:

$$\mu_t = \min \left[ \frac{\rho k}{\omega}; \frac{a_1 \rho k}{S_1 F_1} \right], \quad (3.16)$$

where the constant  $a_1 = 0.31$  and  $S_1$  is the modulus of the average shear rate. The blending function  $F_2$  is defined as:

$$F_2 = \tanh(\arg_2^2), \quad (3.17)$$

$$\arg_2 = \max \left( 2 \frac{\sqrt{k}}{\beta^* \omega y}; \frac{500\nu}{y^2 \omega} \right). \quad (3.18)$$

The constants are calculated from the blending functions:

$$\emptyset = F_1 \emptyset_1 + (1 - F_1) \emptyset_2, \quad (3.19)$$

where  $\emptyset_1$  and  $\emptyset_2$  represent the coefficients of the models  $k - \omega$  and  $k - \varepsilon$  respectively. The constants corresponding to the model are found in (MENTER; ESCH; KONNO, 2003).

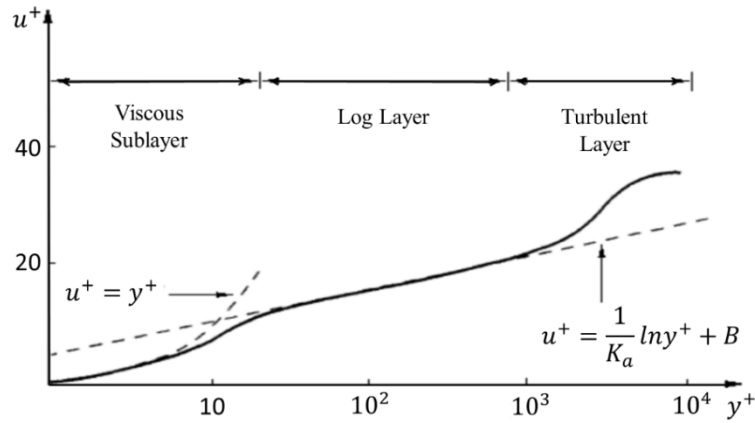
### 3.2.4 Wall Treatment

Turbulent flows are significantly affected by the presence of walls. The average velocity field is affected by the non-slip condition that needs to be satisfied on the wall. However, turbulence is also altered by the presence of the wall in different ways.

A number of experiments (KLINE et al., 1967), (MABEY; MEIER; SAWYER, 1976), (PURTELL; KLEBANOFF; BUCKLEY, 1981) and (HUTCHINS et al., 2009) show that the region near the wall, for a turbulent flow developed without adverse pressure gradient can be subdivided into three layers. In the innermost layer, called the "viscous sublayer", the flow is almost laminar, and the viscosity (molecular) plays a dominant role in the transport of momentum and the transfer of heat or mass. In the outer layer, called totally turbulent layer, the turbulence plays an important role, predominating the turbulent effects of the flow. Finally, there is an intermediate region between the viscous sublayer and the fully turbulent layer, where the effects of molecular viscosity and turbulence are equally important. The

figure below illustrates these subdivisions of the region near the wall, plotted in semi-logarithmic coordinates (WILCOX, 1994).

Figure 3.6 – Subdivisions of the region near the wall.



Source: Adapted from Wilcox (1994).

Semi-empirical formulas are used to model the area affected by the wall, connecting the regions influenced by the viscosity between the wall and the fully turbulent region. Thus, the non-dimensional velocity close to the wall is defined as:

$$u^+ = \frac{1}{K_a} \ln y^+ + C, \quad (3.20)$$

where  $K_a$  is the Kármán constant,  $C$  is a generic integration constant and  $y^+$  is the non-dimensional wall distance:

$$y^+ = \frac{u^* y}{\nu}, \quad (3.21)$$

where  $u^*$  is the friction velocity:

$$u^* = \sqrt{\frac{\tau_w}{\rho}}, \quad (3.22)$$

Depending on the turbulence model chosen some approaches are offered for wall functions. The value of the first point in the mesh varies for each approach. The  $k - \epsilon$  model has some options of wall functions: Standard ( $30 \leq y^+ \leq 300$ ), Scalable ( $y^+ > 11$ ), Enhanced ( $y^+ \approx 1$ ) and Non-Equilibrium ( $30 \leq y^+ \leq 300$ ). However, when applying the Standard and the Scalable wall function, the method assumes a full turbulent developed profile as the one

presented in Figure 3.6 for the first mesh layer while for the Enhanced and Non-Equilibrium not.

In more details, the Standard is an economical computational method, which avoids the need to solve the entire boundary layer profile, representing the properties of the turbulent boundary layer near the wall by means of the algebraic relations described above. However, it has limitations for complex flows with severe pressure gradients (where it is not applicable) or for complex geometries where  $y^+$  must be within the range of values  $30 \leq y^+ \leq 300$  (KUCUKGOKOGLAN et al., 2000). For the same range of  $y^+$  the Non-Equilibrium function, recommended for use in complex flows involving separation, reinsertion and collision where the mean flow and turbulence are subjected to severe pressure gradients and sudden changes (NAJLA et al., 2009) also has the imposition of a high value for  $y^+$  ( $30 > y^+$ ). This restriction, particularly for flows with lower Reynolds numbers, is a severe limitation, since the boundary layer can be fine, so that it can not be solved with a thick mesh near the wall (MENTER; ESCH, 2001).

By requiring a more refined mesh, the Enhanced function allows the representation of low Re and the inclusion of pressure gradients, in addition to accurately representing the velocity profiles when  $y^+ \approx 1$  since it assumes the profile for the viscous layer region of Figure 3.6. However, the restriction that the mesh close to the wall must be sufficiently refined on all surfaces imposes sometimes a large computational requirement (FIUZA; REZENDE, 2018).

The Scalable treatment, used in this work for the  $k - \epsilon$  model, has only a lower bound,  $y^+ > 11$ , a value that marks the intersection between the logarithmic and the linear profile. However, arbitrarily thin meshes can be used in the region near the wall, which allows their application when the geometry is complex, and the points of the mesh close to the wall can not be strictly controlled to guarantee the value of  $y^+$ . The physical interpretation for thin grids is that the wall is treated as if it were the edge of the viscous sublayer. The error introduced by this formulation stems from the effect of the displacement of the viscous sublayer that is not counted in the simulation. However, this is the case for all wall function formulations, since the sublayer is never solved accurately (MENTER; ESCH; KONNO, 2003).

The automatic wall treatment ( $1 \leq y^+$  - similar to the Enhanced function), combined with the SST model, explores the robust formulation for the viscous sublayer but requires a more refined mesh near the wall than the other wall functions (MENTER; ESCH; KONNO, 2003). This model can also be used to model flow near wall with adverse pressure gradient.

In conclusion, two turbulence models combined with wall function were applied in this work: the Standard  $k - \varepsilon$  model with Scalable wall function with the objective to reduce the computational cost and; the SST model with the automatic wall treatment with the objective to better model the adverse pressure gradient expected to appear in the flow between two plates of the modeled configurations of PSHE. Results from both models are compared in the next section.

## 4 RESULTS AND DISCUSSION

This chapter presents the results for this work and is divided into two parts. Part I is comprised by the comparison of numerical results and experimental data for total pressure loss and fluid flow behavior. Part II presents numerical results of mean velocity profiles, pressure fields, Nusselt number and others hydrodynamics characteristics. All results are based on the flow between a pair of PSHE plates with Chevron angle of  $15^\circ \times 15^\circ$ ,  $45^\circ \times 45^\circ$  and  $15^\circ \times 45^\circ$ .

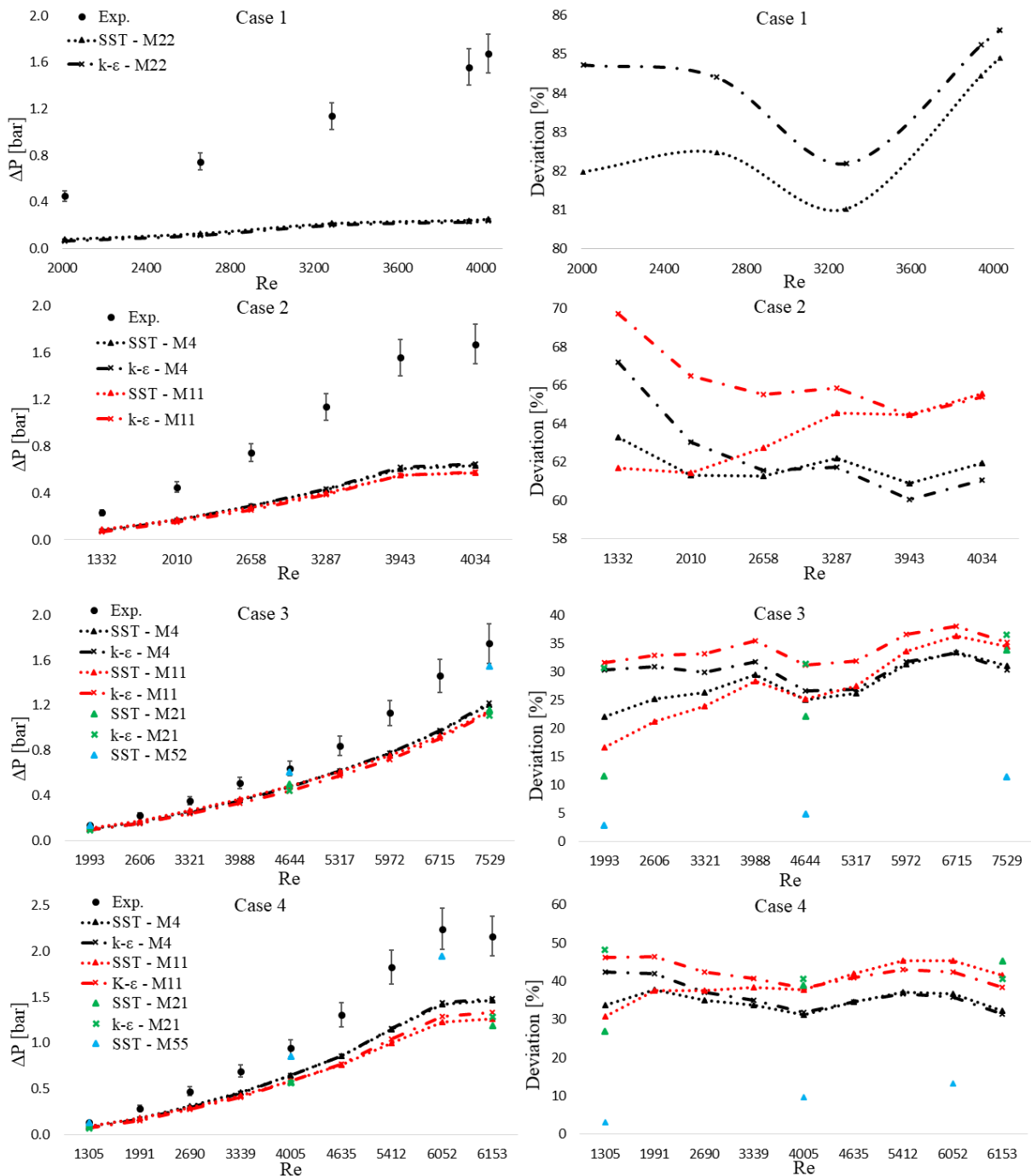
### 4.1 PART I – EXPERIMENTAL VALIDATION AND DISCUSSION

#### 4.1.1 Total Pressure Loss for a Pair of PSHE Plates with Chevron Angle of $15^\circ \times 15^\circ$ , $45^\circ \times 45^\circ$ and $15^\circ \times 45^\circ$

Numerical results from the model for total pressure loss over a pair of PSHE plates for Cases 1 to 4 (identified in section 3.1.1.2) were compared with experimental data for Reynolds number from 1305 to 7529 for Chevron angle of  $15^\circ \times 15^\circ$ ,  $45^\circ \times 45^\circ$  and  $15^\circ \times 45^\circ$  for two turbulence models ( $k - \epsilon$  and SST) and various mesh densities (see Figure 4.1). Results were obtained for isothermal condition ( $25^\circ\text{C}$ ) and with water as fluid. On the left side of Figure 4.1 the pressure loss for each Reynolds number is presented for each case (1 to 4), on the right side the deviation (%) between experimental data and numerical result is indicated. The mesh densities for each case is indicated in the legend of Figure 4.1, where the number next to the turbulence model stands for the approximate number of volumes in the mesh, in millions (For instance, M11 indicates a mesh of approximately 11 million volumes). Notice that different mesh densities were employed for each case, varying from 4 to 55 million volumes. The deviation presented between experimental and numerical data is based on the experimental data. Values can be found in Table A.1 to A.4 (see Appendix A).

Figure 4.1 – Comparison between experimental and numerical data obtained for Case 1 ( $15^\circ \times 15^\circ - 1970 \leq \text{Re} \leq 4034$ ), Case 2 ( $15^\circ \times 15^\circ - 1332 \leq \text{Re} \leq 4034$ ), Case 3 ( $45^\circ \times 45^\circ -$

1993  $\leq$  Re  $\leq$  7529) and Case 4 ( $45^\circ \times 15^\circ - 1305 \leq$  Re  $\leq$  6153): Left: pressure loss on a pair of plates; Right: Deviation (%) between experimental and numerical data.



Source: Author (2019).

As can be seen from Figure 4.1 for Cases 3 ( $45^\circ \times 45^\circ$ ) and 4 ( $45^\circ \times 15^\circ$ ) numerical results are in good agreement with experimental data, indicating a deviation lower than 15% for all Re number tested. Deviations lower than 5% were found for Re numbers lower than 4644 for the plate with Chevron angle of  $45^\circ \times 45^\circ$  while a 10% deviation was found for Re

numbers lower than 4005 for the  $45^\circ \times 15^\circ$  configuration. The SST turbulence model results in better agreement with the experimental data for mesh with higher densities (21 to 55 million volumes) while the  $k - \varepsilon$  model predicts similar results to the SST model for meshes with lower volume densities (4 to 11 million volumes), both with higher deviations, around 30 to 40% for both Chevron angle configurations. That was expected since for lower mesh densities the dimensionless wall distance,  $y^+$ , for both models is predicted with values higher than 1, the recommended value for the SST model to correctly estimate the boundary layer. The  $k - \varepsilon$  model is less affected for this variable since the  $k - \varepsilon$  model with scalable wall function can be applied in a range of  $11 < y^+$ , suitable for this case. However, the later model does not solve the boundary layer for the flow as it assumes a fully developed turbulent boundary layer for the numerical domain, not entirely true for the flow between the two PSHE plates analyzed herein as it will be shown latter on. Values for  $y^+$  for each numerical case can be found in Table A.1 to A.4 (see Appendix A).

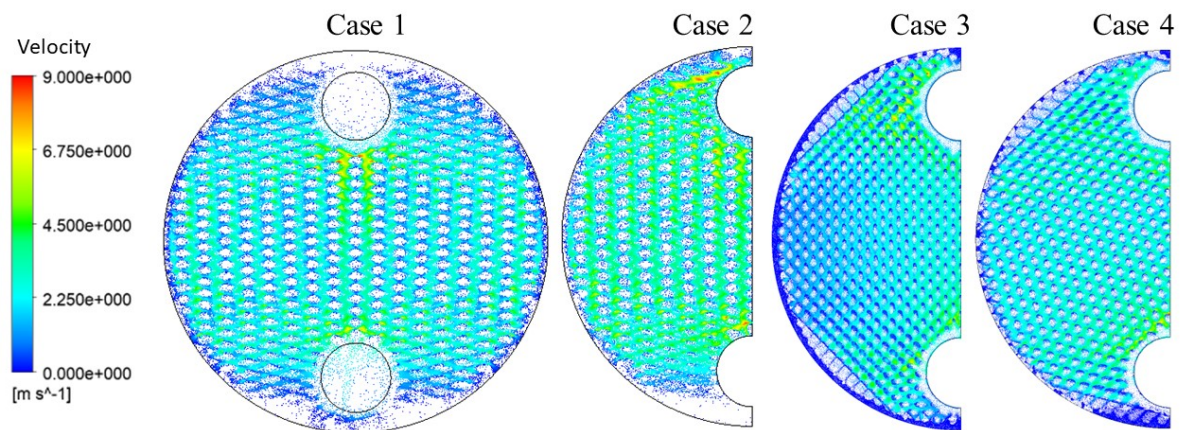
Cases 1 and 2 have the same Chevron angle configuration ( $15^\circ \times 15^\circ$ ) but differ on the geometric domain representation. While Case 2 represents the same geometric configuration as Cases 3 and 4 (one half of the fluid domain obtained by an arrange of two PSHE plates welded together by its external diameter) Case 1 represent the geometry comprised by the full fluid domain between the two plates added by the inlet and outlet pipe. This configuration is more realistic when compared to the experimental setup employed to measure the pressure loss. However, unlike the numerical results for the configuration of Chevron angle of  $45^\circ \times 45^\circ$  and  $45^\circ \times 15^\circ$ , both Cases for the  $15^\circ \times 15^\circ$  configuration presented a high deviation when compared to the experimental pressure loss for the pair of PSHE plates. Numerical prediction indicated pressure losses between 60% (Case 2) to 80% (Case 1) lower than the ones predicted by the experimental data. The better results obtained with Case 2, when compared to Case 1, can be explained as a consequence of the denser mesh applied for the center of the plate on Case 2 while on Case 1 a quantity of the mesh is located in the inlet and outlet tubes. Mesh densities of 22 to 60 million volumes were tested for Case 1 and 2 with no improvement on the results for total pressure loss. The elevated deviation found for the numerical results for the Chevron angle configuration of  $15^\circ \times 15^\circ$  might be associated to others parameters or conditions not investigated in this study.

Despite not being the more geometric realistic model analyzed herein, results obtained for the configurations adopted for the one half of the plate (Case 2, 3 and 4) showed a better agreement with experimental data.

#### 4.1.2 Velocity Field

The velocity field obtained with the numerical model for each Case is presented in Figure 4.2.

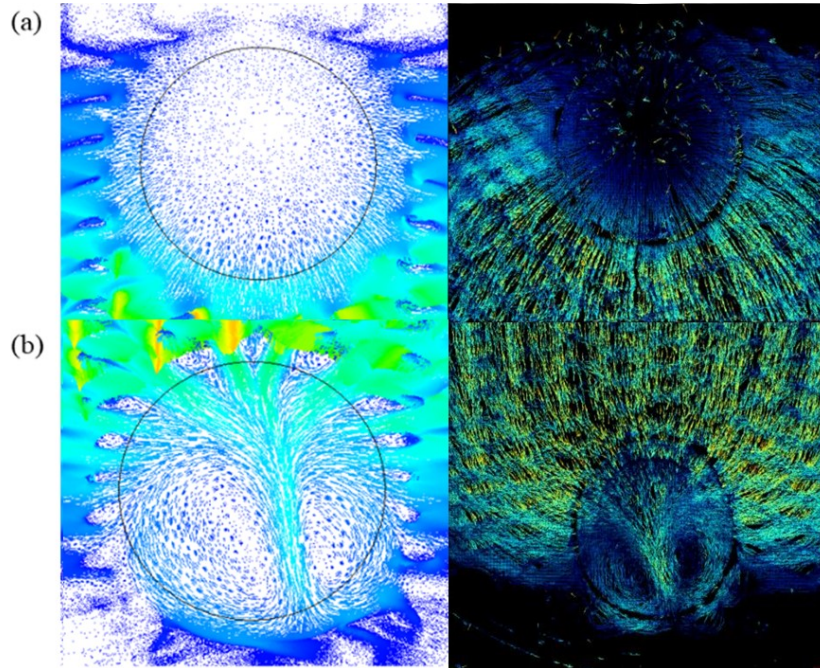
Figure 4.2 – Velocity field plotted on a plane situated between the plates: Case 1 (M22, SST -  $Re = 4451$ ), Case 2 (M4, SST -  $Re = 4451$ ), Case 3 (M21, SST -  $Re = 4643$ ) and Case 4 (M21, SST -  $Re = 4005$ ). Inlet port is located on the upper side of the plate.



Source: Author (2019).

As can be seen, velocities are low and well distributed between the plates, ranging from approximately zero to 9.0 m/s for the different configurations presented for  $4005 < Re < 4643$ . A higher velocity concentration can be noticed near the inlet (upper port) and the outlet (lower port) of the plates due to the reduction/expansion of crossing area for the fluid to enter and exit the plates. This effect can be better visualized on Figure 4.3 where the flow concentrated near the inlet and outlet ports is visualized through PVT (BECKEDORFF et al., 2019) (right side) and compared to the numerical predicting for Case 1 (left side) for the  $15^\circ \times 15^\circ$  configuration. The configuration  $45^\circ \times 45^\circ$  and  $45^\circ \times 15^\circ$  were not compared since no experimental data for these configurations is available.

Figure 4.3 – Velocity field distribution near the inlet (a) and outlet (b) for Chevron angle configuration of  $15^\circ \times 15^\circ$  ( $Re = 3400$ ): Results predicted with numerical model – Case 1 – left side; Experimental result – right side (BECKEDORFF et al., 2019).



Source: Author (2019).

The velocity vector field near the inlet port exhibits an almost uniform behavior, well distributed in the inlet, contributing for a good distribution of the flow to the interior of the plates. Nevertheless, there is a concentration of fluid entering the plates through the lower portion of the inlet. The numerical result predicted by Case 1 reflects a similar behavior, even with the elevated deviation encountered for the estimation of the pressure loss across the plates for the configuration  $15^\circ \times 15^\circ$  presented in Figure 4.1.

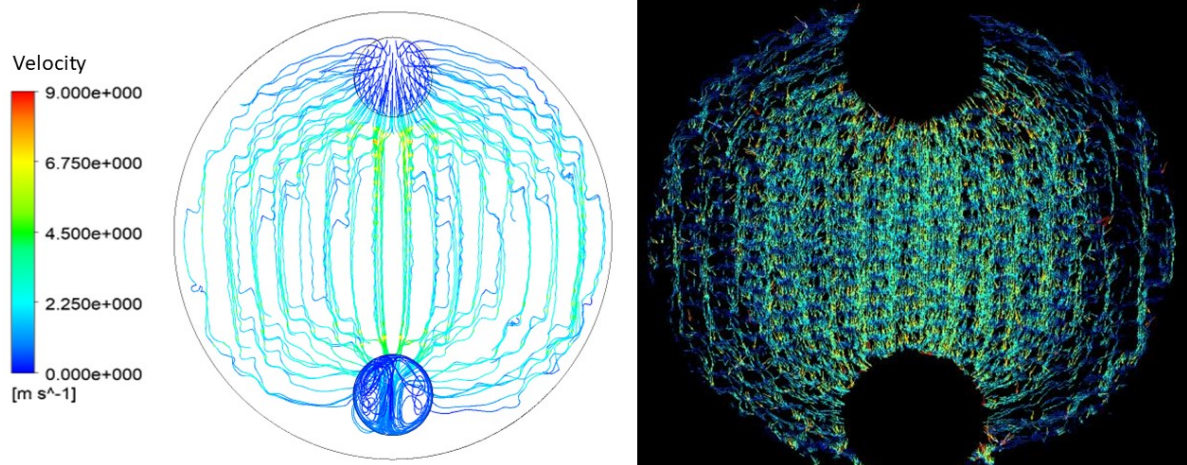
For the outlet port the formation of vortex occurs, probably due to the deceleration of the flow in the exit of the plates. The numerical results for Case 1 also indicated the formation of vortex on the exit port, in a similar pattern.

It is important to highlight here that Case 2 to 4 have a simplification on this behavior in the numerical model. Due to the use of one half of the plates and no tubes connecting the inlet and outlet ports, this model employs a prescribed uniform mass flow distribution on the inlet port. Also as a limitation of this model, on the outlet port, the vortex formation cannot be visualized since no tube is connected into the fluid domain. However, the

velocity field near the outlet port reflects the effect of a non uniform exit through the outlet port, as expected. This results will be shown later on.

Figure 4.4 present the flow pattern inside the PSHE plates with the Chevron angle  $15^\circ \times 15^\circ$  obtained from the numerical model (Case 1) and from the experimental data (BECKEDORFF et al., 2019). Streamlines are connected from inlet (upper port) to outlet (lower port). The flow is approximately uniform on the central region of the plates and mainly aligned with the flow main direction (the vertical direction connecting the ports). This zig-zag pattern, where the fluid is reflected by the contact points between plates, was documented for Plate Heat Exchangers (PHE) by Liu and Tsai (2010), Dovic and Svaic (2004) and by Focke, Zachariades and Olivier (1985) for configurations of low Chevron angle (reference on the horizontal axis), as is the case shown in Figure 4.4.

Figure 4.4 – Flow pattern between a pair of PSHE plates for Chevron angle  $15^\circ \times 15^\circ$ . Left: numerical results for Case 1 (M22, SST and  $Re = 3400$ ); Right: experimental data (BECKEDORFF et al., 2019) ( $Re = 3400$ ).

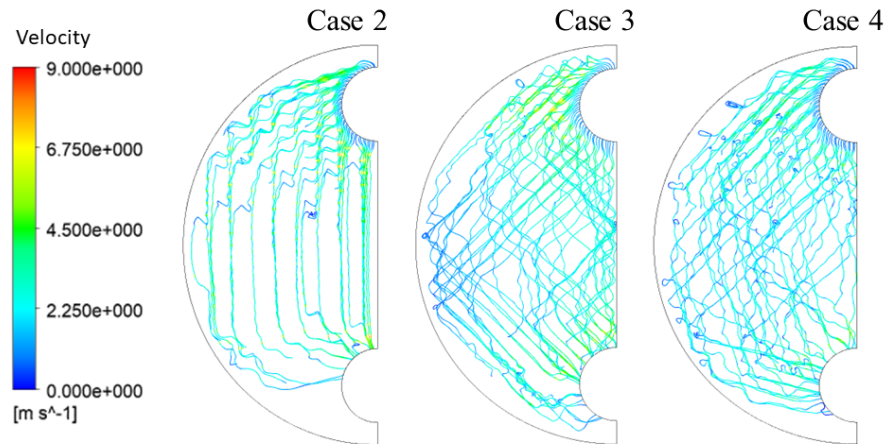


Source: Author (2019).

To analyze the other configurations included herein, Figure 4.5 presents the flow pattern for Cases 2 to 4 predicted by the numerical model. A different pattern can be observed for Case 3 ( $45^\circ \times 45^\circ$  Chevron angle configuration) where the fluid flow more predominantly through the channels formed by the plates until it reaches the border of the plates and then is reflected. This behavior was also documented by Focke, Zachariades and Olivier (1985) for PHE with  $\beta = 45^\circ$ . For Case 4 ( $45^\circ \times 15^\circ$  configuration) a mix of both previous behaviors can be identified, the zig-zag flow and the flow reflected by the border of the plates. Flow pattern

for a mixed pair of plates (plates with different chevron angles) is not documented on the literature up to the date, either for PSHE or PHE.

Figure 4.5 – Flow pattern between a pair of PSHE plates for configurations of Chevron angle of  $15^\circ \times 15^\circ$  (Case 2 (M21, SST -  $Re = 4034$ )),  $45^\circ \times 45^\circ$  (Case 3 - M21, SST -  $Re = 4643$ ) and  $45^\circ \times 15^\circ$  (Case 4 - M21, SST -  $Re = 4005$ ).



Source: Author (2019).

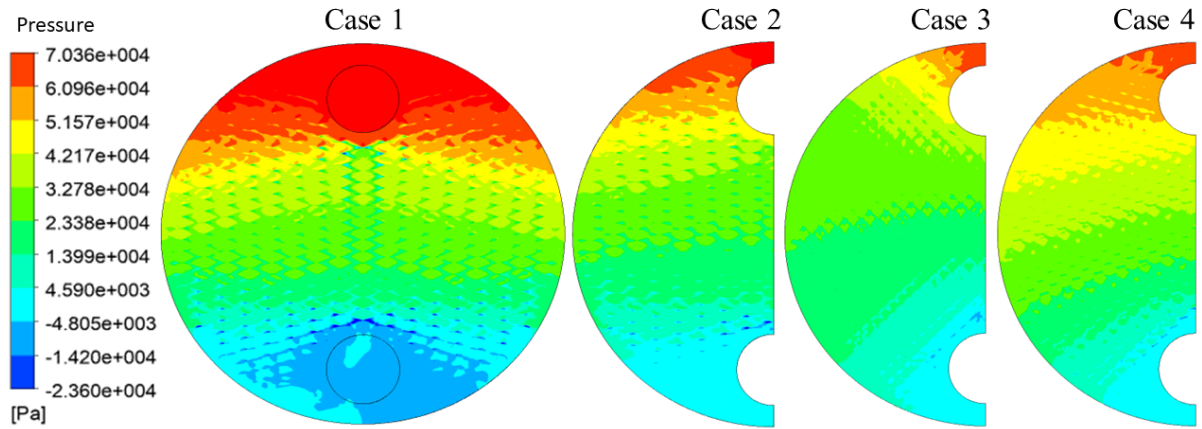
## 4.2 PART II – NUMERICAL RESULTS

This section presents results obtained from the numerical model. These results are not validated with experimental data nevertheless since the same models and mesh from the last section were employed these data serve as an estimative of probable behavior of the flow.

### 4.2.1 Static Pressure Profile on the Surface Across Plates

The static pressure profile on the surface of the plates indicated by the numerical model is presented in Figure 4.6 for all three configurations analyzed in this study.

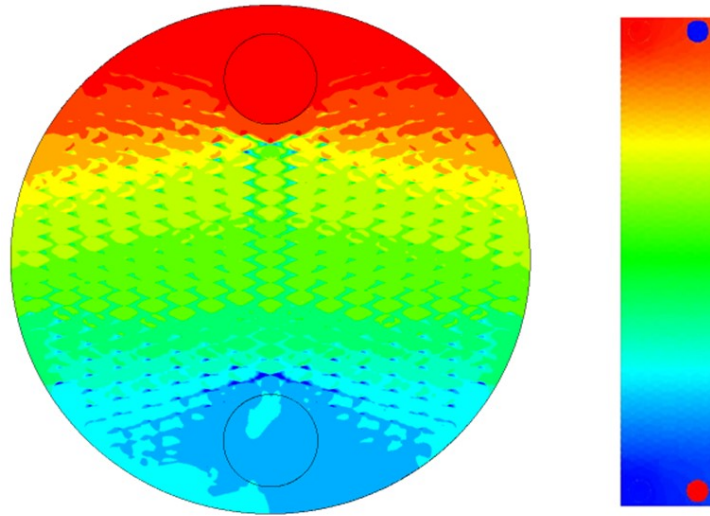
Figure 4.6 – Static pressure profile on the surface of the plates for configurations of Chevron angle of  $15^\circ \times 15^\circ$  (Case 1 (M22, SST -  $Re = 4643$ ) and Case 2 (M4, SST -  $Re = 4034$ )),  $45^\circ \times 45^\circ$  (Case 3 - M21, SST -  $Re = 4644$ ) and  $45^\circ \times 15^\circ$  (Case 4 - M21, SST -  $Re = 4005$ ).



Source: Author (2019).

As expected, the pressure decreases as the fluid flow across the plates, from the inlet to the outlet. It is interesting to notice that the profile for the pressure field differs for each configuration. The configurations  $15^\circ \times 15^\circ$  and  $45^\circ \times 15^\circ$  seems to produce a more uniform profile (on the horizontal axis), similar to the one found for PHE, as can be seen in Figure 4.7. The profile for the  $45^\circ \times 45^\circ$  configurations tends to create a more cylindrical profile near the border of the plates. Also notice the difference between the pressure profile of Case 1 and 2. The inlet and outlet tubes cause the effect of homogenizing the pressure near the inlet and outlet ports. This result suggest that even if the total pressure loss for the configurations  $45^\circ \times 45^\circ$  and  $45^\circ \times 15^\circ$  indicated a small deviation with the experimental data, a more detailed study including the full geometry of the plates with the tubes is advised.

Figure 4.7 – Pressure profile for PSHE (Left: Case 1 ( $15^\circ \times 15^\circ$ ) for  $Re = 4643$ ) and PHE (Right: Adapted from Han et al., 2010).



Source: Author (2019).

## 4.2.2 Velocity, Re Number, Nu Number and Friction Factor

### 4.2.2.1 Volumetric meshes

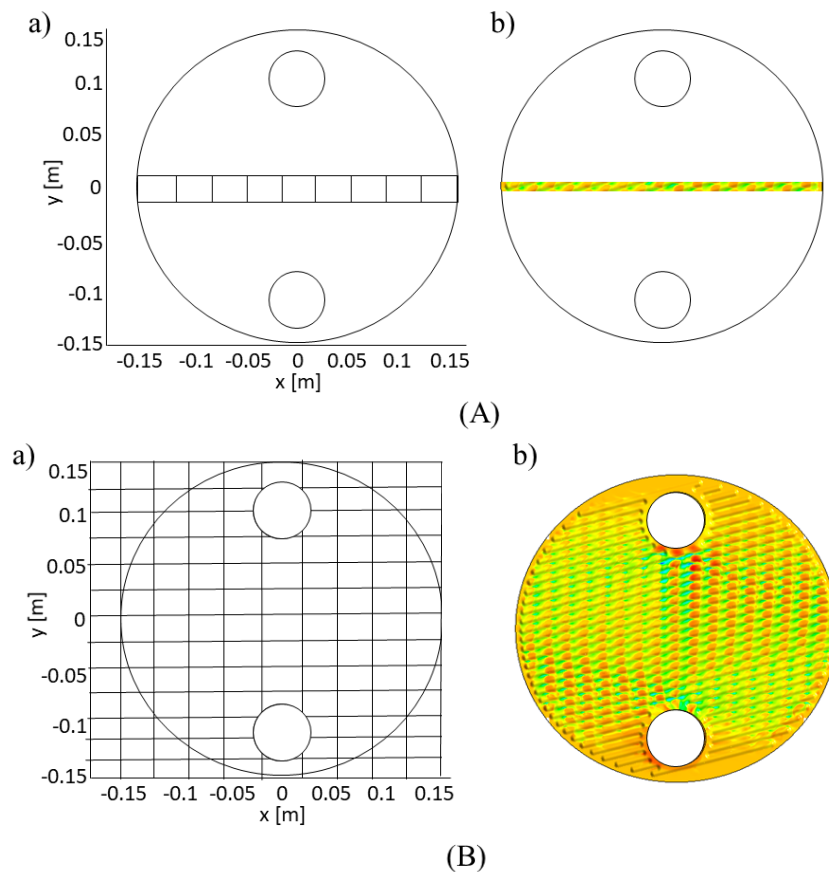
To better visualize the numerical results of the velocity field, Re number, Nu number and friction factor for each plate configuration, a volumetric average methodology was applied to the solution in the post-processing stage.

The methodology consists in dividing the geometric domain in regions of equal volume. In these volumes, the velocity vector is then averaged to represent that specific volume on that specific position, accordingly to Figure 4.8. Two 3D meshes of different number of volumes were created. The most refined volume mesh (Figure 4.8 (A)) is located in the central section of the channel ( $y = 0$  m), with nine rectangular volumes of  $622 \text{ mm}^3$  each. The thicker mesh subdivides the entire channel (Figure 4.8 (b)), the central fractions have volumes equal to  $1533 \text{ mm}^3$ , ranging in the boundaries of the channel between 48 to  $1189 \text{ mm}^3$ .

The volumetric average velocity on the y and x direction (see Figure 4.8) for each volume was obtained from the numerical solution within this methodology and then plotted or used to estimated other parameters with Matlab. The velocity profiles (Figures 4.10 and 4.11)

were obtained with the mesh located at  $y = 0$  m (Figure 4.8 (A)) while all other parameters expressed in color maps (Figures 4.9, 4.13 and 4.14) were obtained for the entire channel with the thickest grid (Figure 4.8 (B)).

Figure 4.8 – Volumetric meshes applied for the volumetric average methodology for post-processing the results for velocity vectors: a) mesh sections indicating the reference axis  $y$  and  $x$ ; b) The complete volumetric mesh. A) Refined volume mesh. B) Thickest volume mesh.



Source: Author (2019).

#### 4.2.2.2 Velocity profile

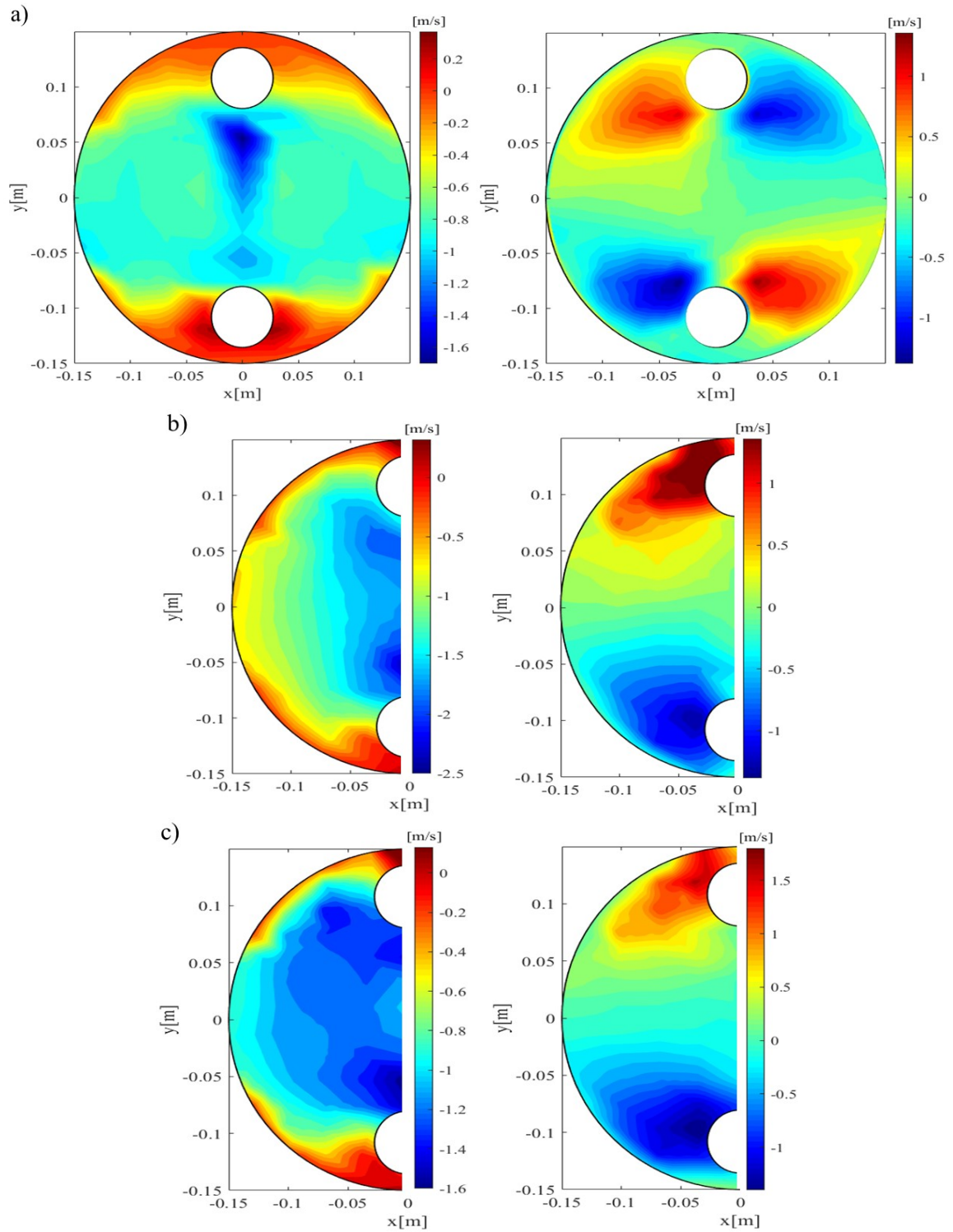
Figure 4.9 presents the vertical and horizontal velocity profile for a plane situated between the pair of plates (see Figure 4.8 (B)) for the configurations  $15^\circ \times 15^\circ$ ,  $45^\circ \times 45^\circ$  and  $45^\circ \times 15^\circ$ . The vertical and horizontal velocity are the velocity vectors aligned with the  $y$  and  $x$  axis from Figure 4.8 (B) respectively. It is important to highlight here that results for the configuration  $15^\circ \times 15^\circ$  indicated an elevated deviation and should only be used as qualitative results. Nevertheless it is interesting to investigate the behavior for the full plate with inlet and

outlet tube. Notice that the sign for the velocity legend in Figure 4.9 indicates the direction of the flow regarded to the y axis (for the vertical velocity) or the x axis (for the horizontal velocity).

At the central region between inlet and outlet ports the averaged vertical velocity reached its maximum value for all cases. A probably explanation for this result is due to a lower resistance to the fluid flow since the path to be traveled by the fluid in the middle of the plate is shorter than at the border of the plate. Also, the profile for the average vertical velocity is approximately symmetric in relation to the horizontal axis at  $y = 0$  m for all cases.

For the average horizontal velocity for the complete plate (Case 1) an axisymmetric behavior for both planes at  $x = 0$  m and  $y = 0$  m can be noticed. This effect is associated to the flow entering and exiting the plates. The same behavior is not noticed for Case 3 and 4 since the geometric domain is comprised only of one half of the plate. There, only the symmetry related to the  $y = 0$  m is noticed again.

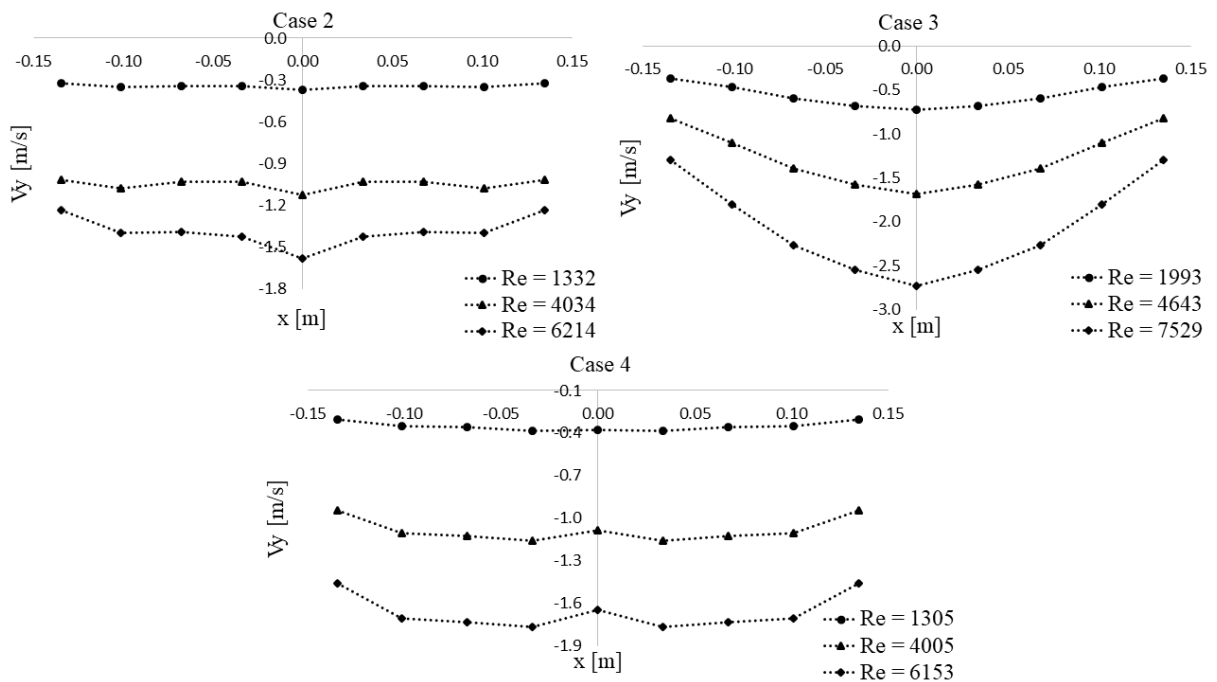
Figure 4.9 – Average velocity for a plane situated between PSHE plates: a) Case 1 (M22, SST –  $Re = 3400$ ), b) Case 3 (M21, SST –  $Re = 4643$ ), c) Case 4 (M21, SST –  $Re = 4005$ ). Left: vertical velocity. Right: horizontal velocity.



Source: Author (2019).

Figure 4.10 shows the averaged vertical velocity profile for the center line of the plate (position  $y = 0$  m) for Cases 2, 3 and 4 for three Re number each (low, medium and high Re number). Since all presented results are for the half plates configurations, results were mirrored at  $x = 0$  m for better visualization.

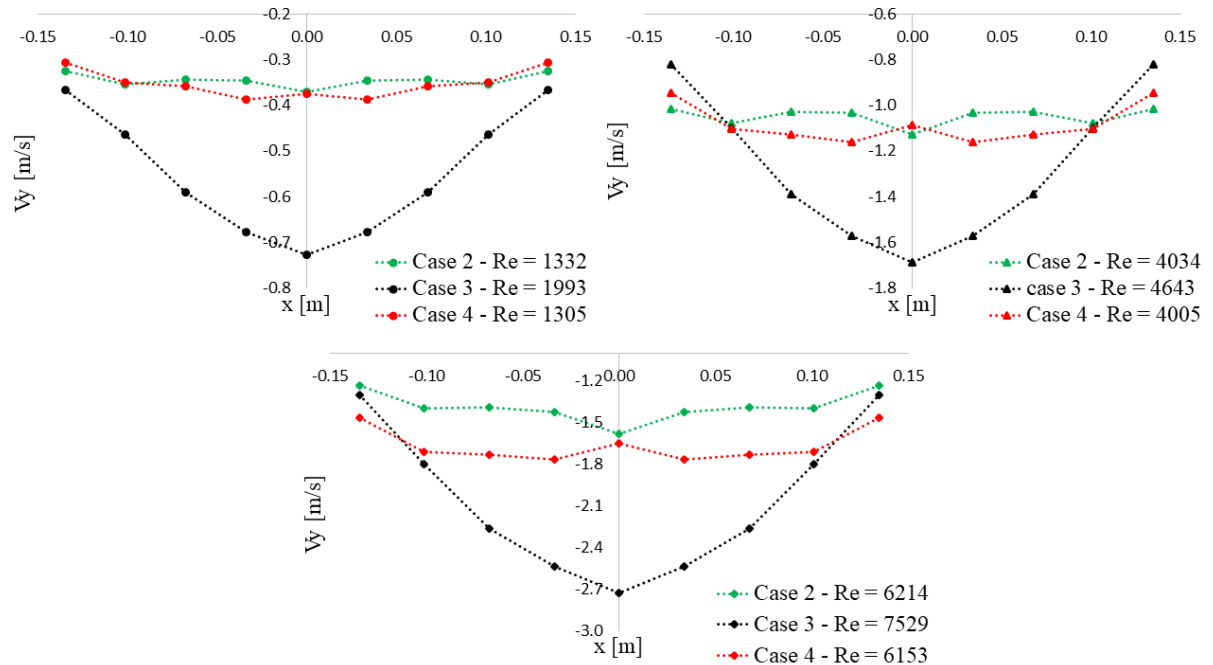
Figure 4.10 – Averaged vertical velocity profile at  $y = 0$  m for low, medium and high Re number: Case 2 ( $15^\circ \times 15^\circ$ , SST and M11), Case 3 ( $45^\circ \times 45^\circ$ , SST and M52) and Case 4 ( $45^\circ \times 15^\circ$ , SST and M55).



Source: Author (2019).

For Cases 2 and 3 the highest speed points are located in the center of the channel ( $x = 0$  [m]), while for Case 4 the speed decreases in this position. Case 3 has uniform parabolic profiles, unlike Cases 2 and 4 which show a slight fluctuation of velocity points along the section. The distinction between vertical velocity profiles is best seen in Figure 4.11, which shows the comparison between the points obtained for the three channels in the different Re ranges.

Figure 4.11 – Vertical velocity profiles in the center of the channel ( $y = 0$  [m]) for the different ranges of  $Re$ .



Source: Author (2019).

The highest velocity peaks are presented in Case 3 in the center of the channel. However, the speed peaks for Case 3 are concentrated in a small area in the center of the channel, restricting the effective heat transfer area. Cases 2 and 4, however, have small variations in velocity along the section, consequently having a larger effective heat transfer area.

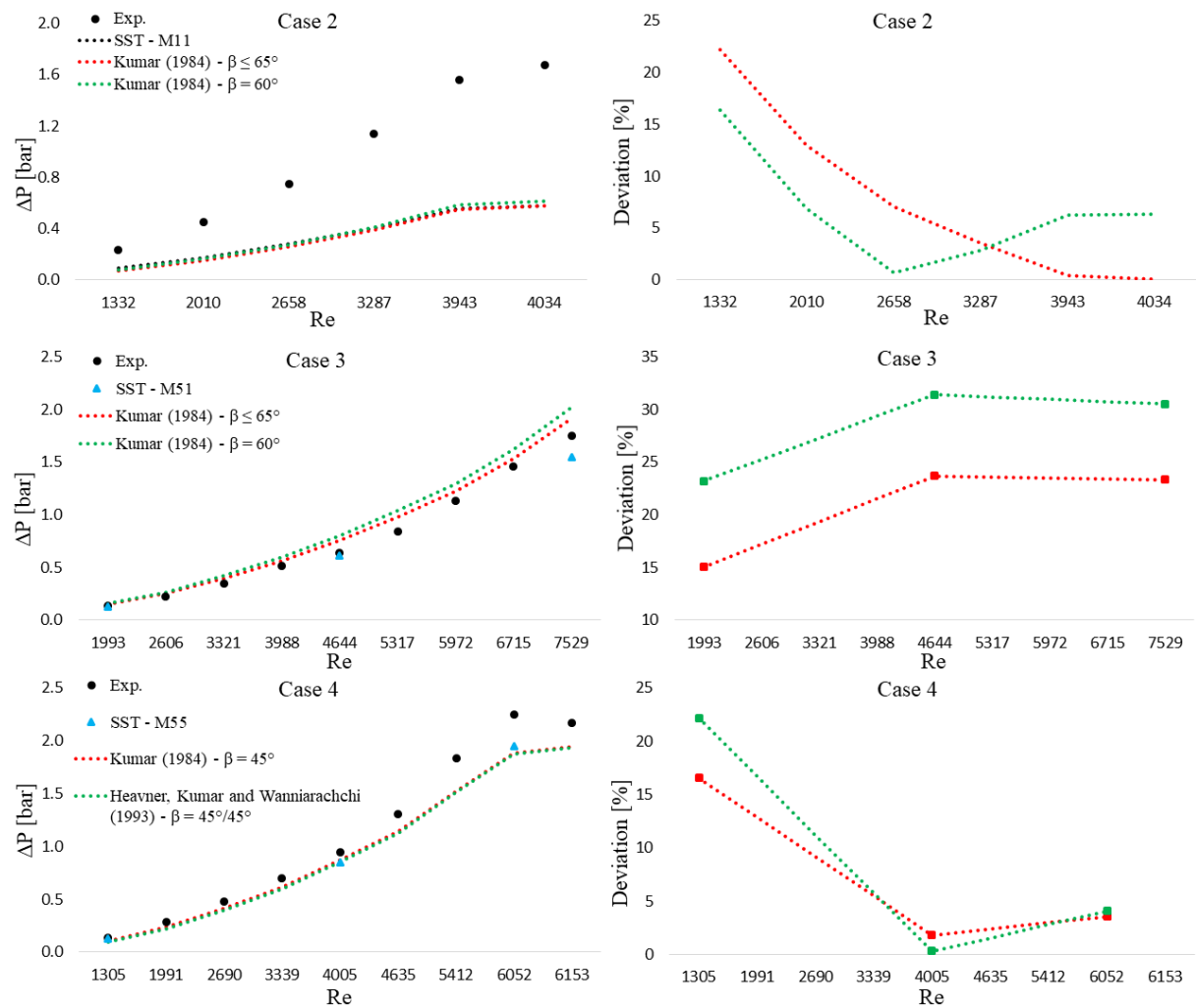
### 4.2.3 Correlations

To evaluate the applicability of the correlations presented for the PHEs (Tables 2.1 and 2.2), the pressure drop was calculated and compared for the PSHE channels. The geometric characteristics of the plates and the input mass flow rates were used to calculate the pressure drop. The pressure drop was obtained through Equation 2.63, disregarding the last term of equation (3) and the Fanning friction factor was obtained through the correlations presented in Table 2.1.

Since the numerical results are close to the experimental ones, with the exception of Case 2 ( $15^\circ \times 15^\circ$ ), Figure 4.12 shows the comparison of the results for the experimentally

obtained pressure loss, numerically and by the two correlations that showed the smallest deviation from the numerical results for the channels of the PSHE.

Figure 4.12 – Comparison between the results obtained by the numerical approach and the correlations for Cases 2, 3 and 4. Left: pressure drop as a function of Reynolds number. Right: deviation (%) from numerical data for pressure loss.



Source: Author (2019).

The correlation of Kumar (1984) to  $\beta \leq 65^\circ$  showed results with better agreement to the numerical results obtained for Cases 2 and 3, whereas for Case 4 the best results were obtained with the correlation of Kumar (1984) to  $\beta = 45^\circ$ . Cases 2 ( $\beta = 15^\circ \times 15^\circ$ ) and 3 ( $\beta = 45^\circ \times 45^\circ$ ) respect the limitation  $\beta \leq 65^\circ$  imposed by the Kumar correlation (1984), the same is not observed for Case 4. It is important to highlight here that these correlations were

developed for PHE only and that the Chevron angle design for a PHE is different from a PSHE (see Figures 2.4 and 2.8). Regardless of how the authors of the correlations measured the  $\beta$  angle with respect to the vertical or horizontal axis of the corrugated channel, the Chevron angles for which the correlations were developed do not match the angles of the cases studied. Results suggest that the set of the geometry characteristics of each plate studied in this work gives the similarity observed between the correlations mentioned in this section and the curves obtained by the numerical approach for total pressure loss within 30% deviation for the  $45^\circ \times 45^\circ$  and  $45^\circ \times 15^\circ$  configuration.

#### 4.2.4 Reynolds, Friction Factor and Nusselt Numbers

Reynolds local number,  $Re(x, y)$ , friction factor,  $f(x, y)$ , and Nusselt number,  $Nu(x, y)$ , were calculated using local convection velocity,  $u(x, y)$ . The magnitude velocity vector was calculated using the axial and longitudinal velocity averages components for each mesh volume (Figure 4.8 (B)).

$Re(x, y)$  was calculated by substituting the average velocity component ( $u_m$ ) for the absolute velocity  $u(x, y)$  in Equation 2.2, considering the constant hydraulic diameter equal to 0.0034 m, a value determined by Equation 2.4 (section 2.3.1). Assuming that the correlations presented in the previous section and formulated for PHEs can be locally applied to a PSHE channel, the friction factor and local Nusselt number were obtained from the correlations presented by Kumar (1984) for  $\beta \leq 65^\circ$  (Cases 2 and 3) and Kumar (1984) for  $\beta = 45^\circ$  (Case 4) (Table 2.1 and 2.2). The figure below gives the numerical results for  $Re(x, y)$  (Figure 4.13 (a)), the friction factor -  $f(x, y)$  (Figure 4.13 (b)) and  $Nu(x, y)$  (Figure 4.13 (c)) for Cases 2, 3 and 4 simulated with the same input flow ( $Re = 1332$ ), with the SST model for the 11 million volumes ( $15^\circ \times 15^\circ$ ) and 21 million volumes ( $45^\circ \times 45^\circ$  and  $45^\circ \times 15^\circ$ ).

The color maps presented for Cases 2 and 4 are qualitatively similar, an aspect probably associated with the plate of  $\beta = 15^\circ$ . In general, the preferred path is located in the center of the channel ( $x \approx 0$  m), where it shows the largest number of local Reynolds, reaching 1939, 2629 and 2091 for Cases 2, 3 and 4, respectively. At the channel boundaries small values of  $Re(x, y)$  were found, less than 4 (Cases 2 and 4) and 51 (Case 3). The local Reynolds number is proportional to the local Nusselt number, which implicates in a similar behavior between the color maps presented for these variables. Consequently, the highest

values for  $Nu(x, y)$  are also in the center of the channel, 47, 45 and 97 for Cases 2, 3 and 4, in that order.

Inversely proportional to  $Re(x, y)$  and  $Nu(x, y)$ , the local friction factor shows a distinct color map. In the center of the channel ( $-0.05 < x [m] < 0.0$ ;  $-0.05 < y [m] < 0.05$ ), the lowest values are observed: 0.12 for Cases 2 and 4, 0.3 for Case 3. Outside this region, at the edges of the plate, the local friction factor increases due to the lower local velocity, reaching 0.46, 0.24 and 0.78 for Cases 2, 3 and 4, respectively.

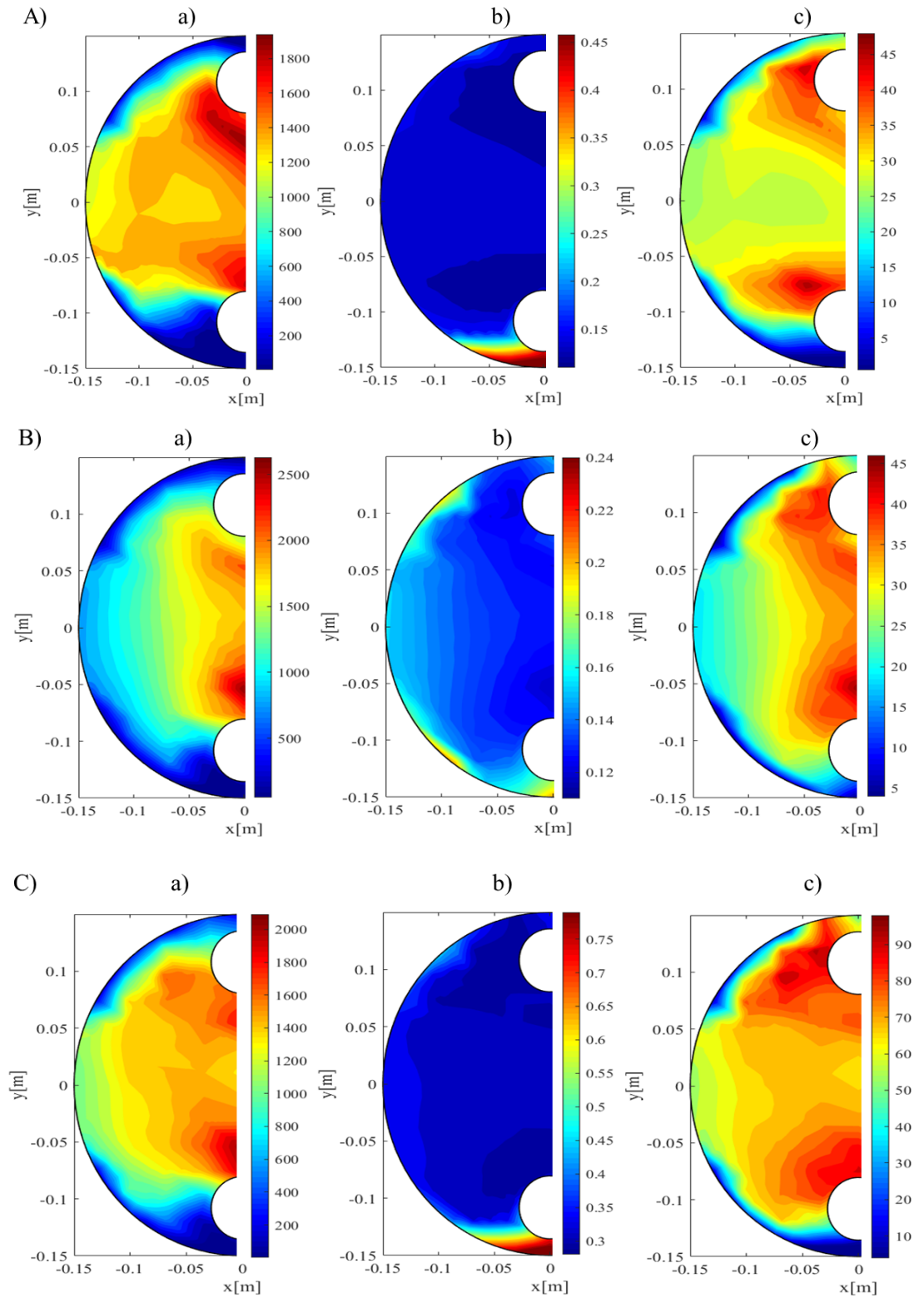
Notice here that the results presented here for Cases 2 ( $15^\circ \times 15^\circ$ ) and 3 ( $45^\circ \times 45^\circ$ ) applied the same correlation of Kumar (1984) for  $\beta \leq 65^\circ$ , pointed as the best for these geometries. For Case 4 ( $45^\circ \times 15^\circ$ ) the values were obtained with the correlation of Kumar (1984) for  $\beta = 45^\circ$ .

Calculating the local average of  $Re(x, y)$  we have 1462, 1179 and 1398 for Cases 2, 3 and 4, in this order. Reynolds local average indicates that Case 2 ( $15^\circ \times 15^\circ$ ) is probably the most efficient of channels. But when we compare the local average  $Nu(x, y)$  we have 26.57 for Case 2, 23.69 for Case 3 and 60.49 for Case 4, suggesting that channel 4 stands out as the most efficient for convective heat transfer. Nusselt numbers calculated here are derived from the correlations and although the correlations of Kumar (1984) for  $\beta \leq 65^\circ$  and  $\beta \leq 45^\circ$  demonstrate compatibility with numerical curves for total pressure loss, it may present an error associated with  $Nu$  number not identified in this study.

Since the local  $Re(x, y)$  was not obtained from a correlation based on PHE, it may be a more reliable indicator in this case, as it was obtained through a global equation.

Assuming the local average of  $Re(x, y)$  to estimate channel efficiency, Case 2 is the most efficient channel. This means that the Chevron angle  $\beta = 15^\circ$  provides a geometric configuration that contributes to the development of turbulent flow, preserving velocity along the channel and consequently maintaining a considerable heat transfer area. The combination  $\beta = 45^\circ \times 15^\circ$  gives Case 4 the second highest efficiency. Despite the higher velocity components, see section 4.2.2, the angle  $\beta = 45^\circ$  concentrates the flow at the center of the channel. Keep in mind that results presented for the  $15^\circ \times 15^\circ$  configuration may present an elevated deviation as indicated in section 4.1.1.

Figure 4.13 – Local: Reynolds number (a), friction factor (b) and Nusselt number (c). A) Case 2 ( $15^\circ \times 15^\circ$ ). B) Case 3 ( $45^\circ \times 45^\circ$ ). C) Case 4 ( $45^\circ \times 15^\circ$ ).



Source: Author (2019).

The average number of  $Re(x,y)$  for Case 2, 3, and 4 calculate in the average plane of the channel ( $y = 0$  m) results is 1315, 1382, and 1374, respectively. Comparing to the total average presented earlier, these results differ by 10%, 17% and 2%, respectively. The average plane results are close to the total averages values, indicating that the central values (at  $y = 0$  m) for the friction factor, Reynolds and Nusselt are representative of the PSHE channel.

#### 4.2.5 Shear Forces

Local force,  $F_{x,y}$ , is obtained by the product of the local shear stress,  $\tau_{w(x,y)}$ , and the local projected area in the xy-plane,  $A_{x,y}$ :

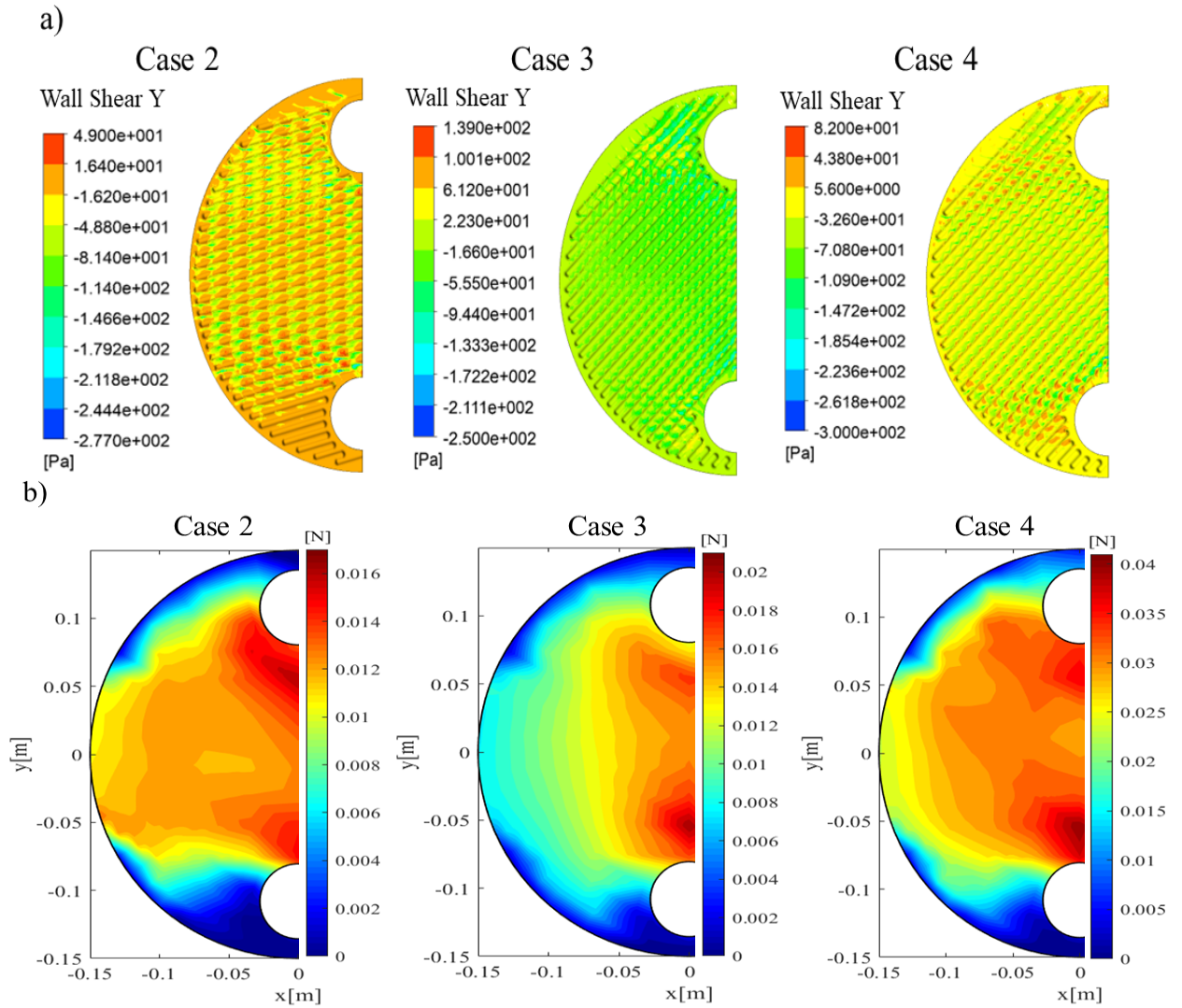
$$F_{x,y} = \tau_{w(x,y)} A_{x,y}, \quad (4.1)$$

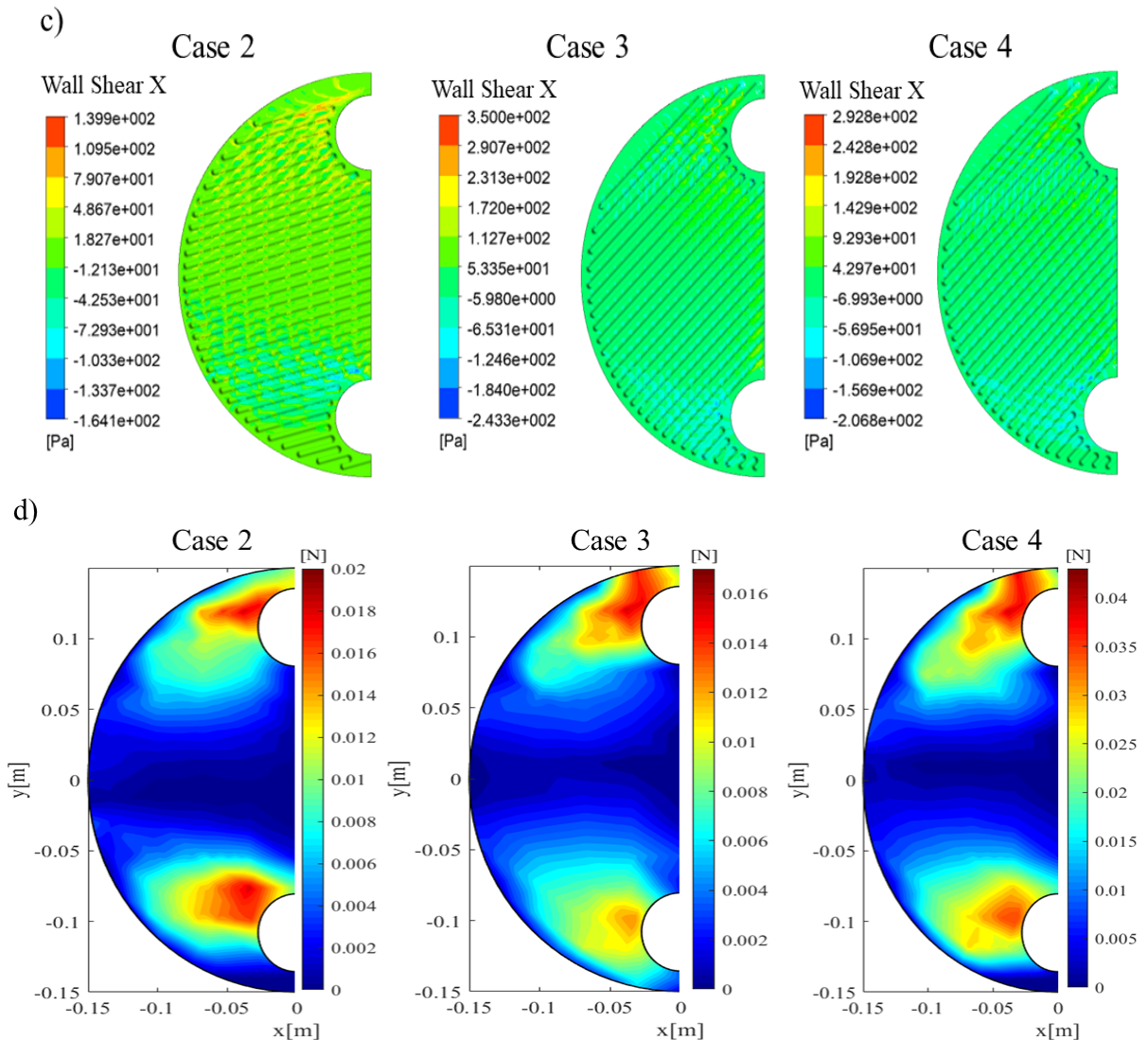
where the subscripts  $x$  and  $y$  represent a location in the mesh volume (Figure 4.8 (B)). The projected area in the xy plane for only one plate is typically 785 mm<sup>2</sup>. With the local friction factor  $f(x, y)$  and the local convective velocity  $u(x, y)$ , calculated in section 4.2.4, the local shear stress can be obtained by:

$$\tau_{w(x,y)} = \left(\frac{1}{2}\right) f_{x,y} \rho |u_{x,y}|^2. \quad (4.2)$$

The figure below presents the results for the shear stress obtained directly in the CFD-post and the shear forces obtained with the volumetric methodology. The Figure 4.14 presents the vertical shear stress (Figure 4.14 (a)), the local vertical shear force ((Figure 4.14 (b)) and its horizontal decompositions shown in Figure 4.14 (c) and (d) for the simulated Cases 2, 3 and 4 with the same input flow ( $Re = 1332$ ), with the SST model for the 11 million volume mesh (Case 2) and 21 million (Cases 3 and 4).

Figure 4.14 – Local: vertical shear stress (a), vertical shear force [N] (b), horizontal shear stress [N] (c), vertical shear force [N] (d). A) Case 2 ( $15^\circ \times 15^\circ$ ). B) Case 3 ( $45^\circ \times 45^\circ$ ). C) Case 4 ( $45^\circ \times 15^\circ$ ).





Source: Author (2019).

Horizontal forces are significant in the areas near the inlet and outlet ports, while forces in the vertical direction are more significant in the center of the channel. In agreement with the color maps presented in section 4.2.4, the region near the outlet concentrates the highest forces due to the fluid recirculation zone.

The integral of the horizontal component of shear forces is close to zero in all cases, since the flow is predominantly vertical. Integrating the results in the CFD-post the vertical shear force is equal to -1.49 N, -1.55 N and -1.60 N for Cases 2, 3 and 4, respectively. These results are on the same order as those obtained by the total sum of the values for each volume obtained by the 3D mesh (Figure 4.14 (b)) (-1.16 N (Case 2), -1.24 N (Case 3) and -1.26 N

(Case 4)), indicating that both methodology are in agreement and that, again, the correlations for PHE applied in section 4.2.3 for the friction factor may be used to estimate this same parameter for the configurations of PSHE studied herein. The largest vertical component of the shear force is obtained by Case 4, due to the higher velocities gradients reached in the channel.

## 5 CONCLUSIONS

### 5.1 MAIN CONCLUSIONS

Numerical simulations were applied to determine the hydrodynamic behavior of the flow between two plates of a PSHE. Two turbulence models were used to analyze four computational domains with Chevron angles of  $15^\circ \times 15^\circ$ ,  $45^\circ \times 45^\circ$  and  $15^\circ \times 45^\circ$ , evaluating different Re ranges. Experimental data were used for comparison and validation of numerical results.

The numerical analysis of the total pressure loss presented satisfactory results for Cases 3 ( $45^\circ \times 45^\circ$ ) and 4 ( $45^\circ \times 15^\circ$ ), agreeing with the experimental results, indicating deviations below 15% for the whole range of Re analyzed. Deviations below 5% were obtained for Re below 4644 for Case 3 while a 10% deviation was found for Re below 4005 for Case 4. The SST turbulence model had higher performance when applied with denser meshes (21 to 52 million volumes), while the  $k - \varepsilon$  model had better performance with thicker meshes (4 to 11 million volumes). However, deviations above 80% and 60% were observed for Cases 1 and 2 ( $15^\circ \times 15^\circ$ ), in this order.

Regarding the velocity fields, the vectors indicate that the flow proceeds predominantly in the vertical direction, with expressive velocities in the center of the channel, flowing from the entrance port to the channel exit port. The velocity field behavior is uniform at the inlet port (Case 1), contrary to the behavior observed at the outlet port, where vortex formation occurs.

Flow patterns have been identified for the channels, with format zig-zag for the channel  $15^\circ \times 15^\circ$ , with preferential path between the grooves for the channel  $45^\circ \times 45^\circ$ , and a combination of the patterns is displayed for the  $15^\circ \times 45^\circ$  arrangement, this last one not yet reported on the literature.

The average velocity profiles obtained in the cross section for the Cases 2, 3 and 4 were studied. Indicating profiles with small variations along the cross section, Cases 2 and 4 are similar, while Case 3 presented a parabolic profile with the velocity peak located at the center of the channel. This behavior points to a large difference between the effective heat transfer areas between Chevron angle configuration.

The total pressure loss results obtained through the correlations developed for the PHEs were compared with the numerical data for the PSHE channels. From this comparison it was concluded that the Kumar correlation for  $\beta \leq 65^\circ$  is the most appropriate to represent the Cases 2 and 3, while the Kumar correlation for  $\beta = 45^\circ$  describes the Case 4 more accurately. The conformance of the results presented in section 4.2.3 is associated with the set of the geometric characteristics of the channels and not exclusively with the Chevron angle.

Reynolds number,  $Re(x, y)$ , friction factor,  $f(x, y)$ , and Nusselt,  $Nu(x, y)$  were calculated locally for Cases 2, 3, and 4. The results agree qualitatively, high values of  $Re(x, y)$  and  $Nu(x, y)$  are concentrated in the center of the channels, inversely proportional, the local friction factor is smaller in the same region. Quantitatively the results for Cases 2 and 4 are similar, since they were obtained for the same correlation of Kumar (1984) for  $\beta \leq 65^\circ$ , different of the Case 3 which use the correlation of Kumar for  $\beta = 45^\circ$ . Derived from the correlations, the prediction of the local Nusselt number may be inaccurate, since the correlations analysis of the correlations presented here considered only the friction factor and not the heat transfer. Also, a low deviation was verified for the local averages of  $Re(x, y)$ ,  $f(x, y)$  and  $Nu(x, y)$ , in relation to the average obtained in the medium plane of the channels, indicating that the local average values are representative of the PSHE channel.

Regarding the shear forces, the horizontal components are expressive in the areas adjacent to the inlet and outlet ports, while the vertical components are significant in the center of the channels. The channel outlet region concentrates the greatest forces due to flow recirculation. The integral of the shear force results in a value close to zero for the horizontal components. For the numerical model the integral of the vertical shear stress resulted in -1.49 N, -1.55 N and -1.60 N for Cases 2, 3 and 4, respectively, for  $Re = 1332$ .

## 5.2 SUGGESTIONS FOR FUTURE WORK

- Reassess the geometry of  $\beta = 15^\circ$ , both numerically and experimentally to mitigate the error associated with the results obtained for the Cases 1 and 2.
- Employ larger mesh refining in order to achieve the  $y^+$  required for the application of the SST model, presenting results with greater reliability.
- Analyze the sensibility of the results for the application of the geometry of Case 1 with Chevron angle of  $45^\circ \times 45^\circ$  and  $45^\circ \times 15^\circ$ ;

- Perform numerical analysis to define the hydrodynamic behavior for the outside of the plates (the shell-side).
- Perform simulations to investigate the thermo-hydrodynamic behavior of the channel flow.
- Perform numerical simulations for one or more connected plates.

## BIBLIOGRAPHY

ABU-KHADER, “Better Thermal Calculations Using Modified Generalized Leveque Equations for Chevron Plate Heat Exchangers”, **International Journal of Green Energy**, 4:4, 351-366 (2007).

AKTURK et al., “Experimental investigation of the characteristics of a chevron-type gasketed plate heat exchanger”, 6th International Advanced Technologies Symposium (IATS’11), 16-18 May 2015, Elazığ, Turkey.

ALFA LAVAL. Tough enough to go round: AlfaDisc shell-and-plate heat exchanger for the process industries. Sweden. 2008. Disponível em: <[https://wpstatic.idium.no/sgp.no/2014/12/Brosjyre\\_2-AlfaDisc.pdf](https://wpstatic.idium.no/sgp.no/2014/12/Brosjyre_2-AlfaDisc.pdf)>. Acesso em: 06 mar. 2018.

BARDINA, J.E.; HUANG, P.G. COAKLEY, T.J. “Turbulence Modeling Validation, Testing, and Development”, NASA Technical Memorandum 110446, abr. 1997.

BECKEDORFF, L. et al., Flow statistics in plate and shell heat exchangers measured with PTV. **International Journal of Heat and Fluid Flow**. Joinville, ago. 2019.

BLAZEK, J. Computational fluid dynamics: Principles and applications; Elsevier, 440p., 2001.

CHISHOLM, D.; WANNIARACHCHI, A. S., Maldistribution in single-pass mixedchannel plate heat exchangers, in Compact Heat Exchangers for Power and Process Industries, HTD-Vol. 201, ASME, New York, 1992, 95.

COOPER A. “Recover more heat with Plate Heat Exchangers”, **Chemical engineer**, Vol. 285, pp.280- 285, May 1974.

ÇENGEL A. Y., Heat and mass transfer: A practica approach. 3. ed. Boston: Mcgraw-hill, 2007.

DOVIC’ et al., “Generalized correlations for predicting heat transfer and pressure drop in plate heat exchanger channels of arbitrary geometry”, **International Journal of Heat and Mass Transfer**, p. 4553–4563, 52 (2009).

DOVIC, D.; SVAIC, S.. Experimental and numerical study of the flow and Heat transfer in plate heat exchanger channels. International refrigeration and air conditioning conference, Purdue e-Pubs, Croatia, 2004.

ELMAATY, T. M. A.; KABEEL, A. E.; MAHGOUB, M., Corrugated plate heat exchanger review. Renewable and Sustainable Energy Reviews. [s.l.], p. 852-860. fev. 2017.

EURO HEAT LTD. Euro Heat. Disponível em: <<http://www.innovationfund.rs/>>. Acesso em: 26 nov. 2019.

FIUZA, G. C. C.; REZENDE, A. L. T., Comparison of K-E Turbulence Model Wall Functions Applied on a T-Junction Channel Flow. **International Journal of Engineering Research & Science**. [s.l], p. 60-70. jan. 2018.

FOCKE, W. W.; ZACHARIADES, J.; OLIVIER, I. The effect of the corrugation inclination angle on the thermohydraulic performance of plate heat exchangers. **Int. J. Heat mass transfer**. Republic of South Africa, p. 1469-1479. jan. 1985.

GESMEX: compact heat exchangers. 2007. Disponível em: <<http://www.gesmex.com/en/>>. Acesso em: 22 fev. 2019.

GHERASIM, I. et al., Heat transfer and fluid flow in a plate heat exchanger part I. experimental investigation. **International Journal of Thermal Sciences**. Sherbrooke, p. 1492-1498. mar. 2011.

GHERASIM, I.; GALANIS, N.; NGUYEN, C. T.. Heat transfer and fluid flow in a plate heat exchanger. part II: assessment of laminar and two-equation turbulent models. **International Journal of Thermal Sciences**. Sherbrooke, p. 1499-1511. mar. 2011.

GRETH, TM11 – Perte de pression et transfert de chaleur dans les échangeurs à plaques en simple phase, Manuel technique, 24 juin 1999.

GULLAPALLI, V. S., Estimation of Thermal and Hydraulic Characteristics of Compact Brazed Plate Heat Exchangers. 2013. 171 f. Tese (Doutorado) - Curso de Heat Transfer Research, Energy Sciences, Lund University, Sweden, 2013.

HAN D. H.; LEE K.J.; KIM Y.H., Experiments on the characteristics of evaporation of R410A in brazed plate heat exchangers with different geometric configurations, **Appl. Therm. Eng.**, 23 (2003) 1209–1225.

HAYES N.; JOKAR A.; AYUB Z.H., Study of carbon dioxide condensation in chevron plates exchangers; heat transfer analysis, **Int. J. Heat Mass Transfer**. 54 (2011) 1121–1131.

HESSELGREAVES J.E.; LAW R.; REAY D., Compact heat exchangers: selection, design and operation. 2. ed. Oxford: Butterworth-heinemann, 2016. 502 p. Disponível em: <[https://books.google.com.br/books?id=je8QCgAAQBAJ&hl=pt-BR&source=gbs\\_navlinks\\_s](https://books.google.com.br/books?id=je8QCgAAQBAJ&hl=pt-BR&source=gbs_navlinks_s)>. Acesso em: 06 mar. 2018.

HEAVNER R. L.; KUMAR H.; WANNIARACHCHI, A. S., Performance of an industrial plate heat exchanger: effect of chevron angle, AICHE Symposium Series No. 295, Vol. 89, AICHE, New York, 262, 1993.

HUANG, J., Performance analysis of plate heat exchangers used as refrigerant evaporators. 2010. 295 f. University of the Witwatersrand, Johannesburg, 2010.

HUTCHINS N. et al., “Hot-wire spatial resolution issues in wall-bounded turbulence,” *J. Fluid Mech.* 635, 103 2009.

IKEGAMI Y.; MUTAIR S.; KAWABATA Y., Experimental and Numerical Investigations on Plate-Type Heat Exchanger Performance. **Open Journal of Fluid Dynamics**. [s.l.], p. 92-98. mar. 2015.

JAIN S.; JOSHI A.; BANSAL P. K., A new approach to numerical simulation of small sized plate heat exchangers with chevron plates. **Journal of Heat Transfer**, [s.l.], v. 129, n. 3, p.291-297, mar. 2007. ASME International. <http://dx.doi.org/10.1115/1.2430722>.

JIN S.; HRNJAK P., Effect of end plates on heat transfer of plate heat exchanger. **International Journal of Heat and Mass Transfer**. Urbana, p. 740-748. nov. 2016.

KAKAÇ, S.; LIU H.; PRAMUANJAROENKIJ A., Heat exchangers: selection, rating, and thermal design. 3. ed. New York: Taylor & Francis Group, 2012. 624 p.

KANARIS A.G.; MOUZA A.A.; PARAS S.V., Flow and heat transfer in narrow channels with corrugated walls. **Chemical Engineering Research and Design**, [s.l.], v. 83, n. 5, p.460-468, maio 2005. Elsevier BV. <http://dx.doi.org/10.1205/cherd.04162>.

KANARIS et al., Flow and Heat Transfer Prediction in a Corrugated Plate Heat Exchanger using a CFD Code, **Chem. Eng. Technol.** 2006, 29, No. 8, 923–930.

KHAN M.S. et al., “Evaporation heat transfer and pressure drop of ammonia in a mixed configuration chevron plate heat exchanger”, **Int. J. Refrig.** 41 (2014) 92–102.

KLIN S. J. et al., The structure of turbulent boundary layers. *J. Fluid Mech.* Great Britain, p. 741-773. jul. 1967.

KUCUKGOKOGLAN S. et al., Prediction of interactions between burners in multi-burners systems. International Symposium on Multiphase Flow and Transport Phenomena, 5-10 November 2000, Antalya, Turkey.

KUMAR B.; SINGH S.N., Study of pressure drop in single pass U-type plate heat exchanger. **Experimental Thermal and Fluid Science**, p. 40-49. abr. 2017.

KUMAR H., The plate heat exchanger: construction and design, in: Institute of Chemical Engineering Symposium Series, 1984, pp. 1275–1288.

LIU, F.; TSAI, Y., An experimental and numerical investigation of fluid flow in a cross-corrugated channel. *Heat and Mass Transfer*, [s.l.], v. 46, n. 5, p.585-593, maio 2010. Springer Science and Business Media LLC. <http://dx.doi.org/10.1007/s00231-010-0605-7>

LIU, J. et al., Numerical simulation and optimization on fluid flow distribution performance of plate and shell heat exchanger’s shell-side. **Chemical Industry And Engineering Progress**. Guangdong, p. 3569-3576. 2015.

LUAN H. B. et al., CFD analysis of two types of welded plate heat exchangers. **Umerical Heat Transfer, Part A: Applications: An International Journal of Computation and Methodology**. Sweden, p. 250-269. fev. 2017.

MABEY D. G.; MEIER, H. V.; SAWYER, W. G., Experimental studies of the boundary layer on a flat plate at mach numbers from 2.5 to 4.5, RAE TR 74127, 1976.

MARTIN, H., A theoretical approach to predict the performance of chevron-type plate heat exchangers. *Chemical Engineering And Processin*, Karlsruhe, v. 35, p.301-310, 1996.

MCGEORGE H. D., General engineering knowledge: Marine engineering series. 3. ed. Woburn: Routledge, 1991. 157 p.

MEHRABIAN M.A.; POULTER, R., Hydrodynamics and thermal characteristics of corrugated channels: computational approach. *Applied Mathematical Modelling*, Kerman, v. 2000, n. 24, p.343-364, jul. 1998.

MENTER F.; ESCH T., Elements of industrial heat transfer predictions. 16th Brasilian Congress of Mechanical Engineering, 2001.

METWALLY; MANGLIK, “Enhanced heat transfer due to curvature-induced lateral vortices in laminar flows in sinusoidal corrugated-plate channels”, **International Journal of Heat and Mass Transfer**. p. 2283–2292, 2004.

MENTER F.; C. F. J.; ESCH T.; KONNO B. The SST turbulence model with improved wall treatment for heat transfer prediction in gas turbines. *International gas turbinecongress*, GTSJ, 2003.

MULEY A.; MANGLIK, R. M., Enhanced heat transfer characteristics of singlephase flows in a plate heat exchanger with mixed chevron plates, **J. Enhanced Heat Transfer**, 4(3), 187, 1997.

MULEY A.; MANGLIK R.M.; METWALLY H.M., Enhanced heat transfer characteristics of viscous liquid flows in a chevron plate heat exchanger, *ASME J. Heat Transfer*, pp. 1011–1017, 1999.

MULEY A.; MANGLIK, R. M., Experimental investigation of heat transfer enhancement in a PHE with  $\beta = 60^\circ$  chevron plates, *Heat and Mass Transfer*, Tata McGraw-Hill, New Delhi, India, 1995, 737.

MULEY A.; MANANGLIK R.M., “Experimental study of turbulent flow heat transfer and pressure drop in a plate heat exchanger with chevron plates”, *Journal of heat transfer*, Vol.121, pp. 110-117; 1999.

PRICE; FATTAH, “Hydrodynamic characteristics of a Plate Heat Exchanger Channel”, **Trans. Inst. Of Chem. Eng.**, Vol.56, pp.217-228, 1978.

PURTELL, L. P.; KLEBANOFF, P. S.; BUCKLEY, F.T., Turbulent boundary layer at low Reynolds number. *Physics of Fluids*, [s.l.], v. 24, n. 5, p.802-811, 1981. AIP Publishing. <http://dx.doi.org/10.1063/1.863452>.

RAO, B. P.; SUNDEN, B.; DAS, S., An experimental and theoretical investigation of the effect of flow maldistribution on the thermal performance of plate heat exchangers. **J. Heat Transfer**, 127, 332, 2005.

OKADA et al., “Design and heat transfer characteristics of new plate heat exchanger”, **Heat transfer Japanese research**, Vol.1, pp.90-95, 1972.

SAVOSTIN, A. F.; TIKHONOV, A. M., Investigation of the characteristics of platetype heating surfaces, **Thermal Eng.**, 17(9), 113, 1970.

SHAH, R. K.; SUBBARAO, E. C.; MASHELKAR, R. A., *Heat Transfer Equipment Design*. New York: Crc Press, 1988. 804 p.

SHAH, R. K.; SEKULIC, D. P., *Fundamentals of heat exchanger design*. New Jersey: John Wiley & Sons, Inc, 2003. 972 p.

SHIOMI, Y.; NAKANISHI, S.; UEHARA, T.. Characteristics of two-phase flow in a channel formed by chevron type plates. *Experimental Thermal and Fluid Science*, [s.l.], v. 28, n. 2-3, p.231-235, jan. 2004. Elsevier BV. [http://dx.doi.org/10.1016/s0894-1777\(03\)00044-x](http://dx.doi.org/10.1016/s0894-1777(03)00044-x).

TALIK, A. C; SWANSON, L. W., Heat transfer and pressure drop characteristics of a plate heat exchanger using a propylene-glycol/water mixture as the working fluid, *Proc. 30th Natl. Heat Transfer Conf.*, 12, 83, 1995.

THULUKKANAM, K., *Heat exchanger design handbook: Mechanical Engineering*. 2. ed. New York: Crc Press, 2013. 1260 p. Disponível em: <[https://books.google.com.br/books?id=hmzRBQAAQBAJ&hl=pt-BR&source=gbs\\_navlinks\\_s](https://books.google.com.br/books?id=hmzRBQAAQBAJ&hl=pt-BR&source=gbs_navlinks_s)>. Acesso em: 27 fev. 2018.

TOVAZHNYANSKI, L. L.; KAPUSTENKO, P. A.; TSIBULNIK, V. A., Heat transfer and hydraulic resistance in channels of plate heat exchangers, *Energetika*, 9, 123, 1980.

TSAI, Y.; LIU, F.; SHEN, P., Investigations of the pressure drop and flow distribution in a chevron-type plate heat exchanger. **International Communications in Heat and Mass Transfer**. Kaohsiung, p. 574-578. abr. 2009.

TURK, C.; ARADAG, S.; KAKAC, S., Experimental analysis of a mixed-plate gasketed plate heat exchanger and artificial neural net estimations of the performance as an alternative to classical correlations. **International Journal of Thermal Sciences**. [s.l.], p. 263-269. jun. 2016.

VAHTERUS OY. *Plate & Shell Heat Exchanger*. 2017. Disponível em: <<http://www.vahterus.com/en/node/528>>. Acesso em: 14 maio 2018.

VITILLO, F., Experimental and numerical contribution to heat transfer enhancement in compact plate heat exchangers. Modeling and Simulation. 2015. 310 f. Tese (Doutorado) - Institut Supérieur de L'aeronautique Et de L'espace, 2014.

WANG, L.; SUNDÉN, B., Optimal design of plate heat exchangers with and without pressure drop specifications, **Appl. Thermal Eng.**, 23, 295, 2003.

WANG, Y. et al., A Study on 3D Numerical Model for Plate Heat Exchanger. *Procedia Engineering*, [s.l.], v. 174, p.188-194, 2017. Elsevier BV. <http://dx.doi.org/10.1016/j.proeng.2017.01.203>.

WANNIARACHCHI A. et al., Approximate correlation for chevron type plate heat exchangers. ASME 1995; HTD-314.

WILCOX, D. C. Turbulence modeling for CFD. [S.l.]: DCW industries La Canada, CA, 1994. v. 2.

## APPENDIX A – Numerical results

The tables below show the results for total pressure loss obtained with the numerical approach with the SST and  $k - \epsilon$  turbulence models for the cases studied with different meshes, the deviation (%) of the experimental data and the dimensionless wall distance.

Table A.1 – Comparison between experimental and numerical results obtained with the SST and  $k - \epsilon$  models for pressure drop for the Cases 1 and 2 ( $15^\circ \times 15^\circ$ ) ( $1970 \leq Re \leq 10819$ ).

$\dot{m}$ [kg/s]	0.222	0.285	0.323	0.415	0.490	0.55	0.612	0.819	1.016	1.249	1.426
Re	1970	2162	2873	3149	3400	4452	4643	6214	7708	9476	10819
Case1 – M22											
$\Delta P$ SST [bar]	0.073	0.112	0.139	0.215	0.288	0.299	0.431	0.735	1.106	1.639	2.117
$\Delta P$ $k-\epsilon$ [bar]	0.061	0.098	0.124	0.201	0.206	0.289	0.427	0.758	1.161	1.748	2.272
y+ SST	4.50	5.96	6.50	7.74	7.80	8.80	10.12	12.48	14.72	17.41	19.43
y+ $k-\epsilon$	3.52	4.42	4.95	6.25	6.32	7.44	9.01	11.93	14.73	18.06	20.59
Case 2 – M4											
$\Delta P$ SST [bar]	0.076	0.119	0.150	0.239	0.244	0.341	0.502	0.884	1.353	2.026	2.624
$\Delta P$ $k-\epsilon$ [bar]	0.072	0.118	0.149	0.242	0.247	0.349	0.521	0.925	1.405	2.117	2.727
y+ SST	8.04	9.72	10.64	13.88	13.00	14.91	17.53	24.47	29.53	35.35	39.69
y+ $k-\epsilon$	6.66	9.79	9.77	13.91	12.77	15.29	20.18	26.61	32.51	39.34	42.90

Table A.2 – Comparison between experimental and numerical results obtained with the SST and  $k - \epsilon$  models for pressure drop for the Case 3 ( $45^\circ \times 45^\circ$ ) ( $1993 \leq Re \leq 7529$ ).

$\dot{m}$ [kg/s]	0.296	0.387	0.493	0.592	0.689	0.789	0.886	0.996	1.117
Re	1993	2606	3321	3988	4644	5317	5972	6715	7529
$\Delta P$ exp. [bar]	0.133	0.223	0.350	0.512	0.641	0.840	1.132	1.461	1.749
Case 3 – M4									
$\Delta P$ SST [bar]	0.104	0.166	0.257	0.361	0.481	0.621	0.778	0.972	1.207
$\Delta P$ $k-\epsilon$ [bar]	0.093	0.154	0.245	0.349	0.470	0.614	0.772	0.973	1.218
Deviation SST [%]	22.11	25.18	26.39	29.45	25.05	26.14	31.31	33.48	31.00
Deviation $k-\epsilon$ [%]	30.33	30.86	29.98	31.76	26.63	26.89	31.79	33.39	30.37
y+ SST	11.06	13.28	15.98	18.61	21.17	23.80	26.57	29.46	32.56
y+ $k-\epsilon$	7.88	10.04	12.57	20.74	24.19	19.72	22.07	24.71	27.58
Case 3 – M11									
$\Delta P$ SST [bar]	0.111	0.175	0.266	0.366	0.479	0.609	0.750	0.929	1.146
$\Delta P$ $k-\epsilon$ [bar]	0.091	0.149	0.234	0.330	0.441	0.572	0.718	0.904	1.134
Deviation SST [%]	16.65	21.18	23.90	28.38	25.26	27.55	33.70	36.40	34.47
Deviation $k-\epsilon$ [%]	31.67	32.97	33.18	35.54	31.21	31.91	36.56	38.09	35.20
y+ SST	5.98	7.28	8.60	10.66	11.81	12.95	14.05	15.30	16.66
y+ $k-\epsilon$	5.07	6.42	7.97	9.41	10.83	11.74	13.75	15.39	17.22
Case 3 – M52									

$\Delta P$ SST [bar]	0.129	-	-	-	0.61	-	-	-	1.55
Deviation SST [%]	2.78	-	-	-	4.87	-	-	-	11.39
y+ SST	2.0	-	-	-	5.0	-	-	-	10.0

Table A.3 – Comparison between experimental and numerical results obtained with the SST and k –  $\epsilon$  models for pressure drop for Case 4 (45°x15°) ( $1305 \leq Re \leq 6153$ ).

$\dot{m}$ [kg/s]	0.194	0.295	0.399	0.495	0.594	0.688	0.803	0.898	0.913
Re	1305	1991	2690	3339	4005	4635	5412	6052	6153
$\Delta P$ exp. [bar]	0.131	0.288	0.473	0.694	0.942	1.305	1.829	2.246	2.165
Case 4 – M4									
$\Delta P$ SST [bar]	0.087	0.179	0.307	0.459	0.648	0.855	1.148	1.422	1.465
$\Delta P$ k- $\epsilon$ [bar]	0.075	0.167	0.297	0.451	0.642	0.853	1.156	1.441	1.485
Deviation SST [%]	33.76	37.73	35.06	33.83	31.21	34.51	37.22	36.69	32.34
Deviation k- $\epsilon$ [%]	42.50	41.91	37.15	35.04	31.84	34.63	36.77	35.86	31.40
y+ SST	8.05	10.51	12.09	15.11	17.53	19.82	22.61	24.89	25.22
y+ k- $\epsilon$	6.54	9.53	12.54	15.33	18.18	20.86	24.14	26.83	27.23
Case 4 – M11									
$\Delta P$ SST [bar]	0.091	0.179	0.296	0.427	0.585	0.757	0.999	1.226	1.264
$\Delta P$ k- $\epsilon$ [bar]	0.071	0.154	0.272	0.411	0.582	0.771	1.040	1.293	1.335
Deviation SST [%]	30.86	37.65	37.46	38.41	37.85	41.97	45.35	45.42	41.60
Deviation k- $\epsilon$ [%]	46.19	46.47	42.52	40.78	38.20	40.94	43.12	42.44	38.33
y+ SST	5.77	7.57	9.20	10.59	11.95	13.20	14.73	16.02	16.23
y+ k- $\epsilon$	4.13	6.01	7.89	9.62	11.38	13.05	15.10	16.79	17.06
Case 4 – M55									
$\Delta P$ SST [bar]	0.127	-	-	-	0.85	-	-	1.95	-
Deviation SST [%]	3.12	-	-	-	9.74	-	-	13.18	-
y+ SST	2.0	-	-	-	6.0	-	-	11.0	-

Table A.4 – Comparison between experimental and numerical results obtained with the SST and k –  $\epsilon$  model for pressure drop for the Cases 1 and 2 (15°x15°) ( $1332 \leq Re \leq 4034$ ).

$\dot{m}$ [kg/s]	0.198	0.298	0.394	0.488	0.585	0.599
Re	1332	2010	2658	3287	3943	4034
$\Delta P$ exp. [bar]	0.232	0.451	0.747	1.137	1.557	1.674
Case 2 – M4						
$\Delta P$ SST [bar]	0.085	0.175	0.289	0.430	0.609	0.637
$\Delta P$ k- $\epsilon$ [bar]	0.076	0.167	0.287	0.435	0.622	0.652
Deviation SST [%]	63.31	61.34	61.27	62.19	60.91	61.97
Deviation k- $\epsilon$ [%]	67.19	63.03	61.57	61.73	60.03	61.07
y+ SST	7.47	10.06	12.31	14.49	16.88	17.21
y+ k- $\epsilon$	6.36	9.26	12.04	14.71	17.49	17.88

Case 2 – M11						
$\Delta P$ SST [bar]	0.089	0.174	0.278	0.403	0.553	0.576
$\Delta P$ k- $\epsilon$ [bar]	0.070	0.151	0.258	0.388	0.554	0.579
Deviation SST [%]	61.70	61.44	62.76	64.56	64.47	65.57
Deviation k- $\epsilon$ [%]	69.72	66.51	65.53	65.88	64.45	65.39
y+ SST	4.25	5.95	7.42	8.68	11.73	11.91
y+ k- $\epsilon$	4.04	5.85	7.57	9.24	10.99	11.23
Case 1 – M22						
$\Delta P$ SST [bar]	-	0.081	0.131	0.216	0.242	0.253
$\Delta P$ k- $\epsilon$ [bar]	-	0.069	0.117	0.203	0.23	0.241
Deviation SST [%]	-	81.98	82.48	81.03	84.44	84.9
Deviation k- $\epsilon$ [%]	-	84.73	84.41	82.19	85.23	85.62
y+ SST	-	4.8	6.34	7.75	8.33	8.77
y+ k- $\epsilon$	-	3.34	4.79	6.26	6.64	6.79